Search for a Supersymmetry Signature with the $Z\gamma$ Plus Missing Transverse Energy Final State Using the D0 Detector

by

Alan W. Wilson

A dissertation submitted in partial fulfillment
of the requirements for the degree of
Doctor of Philosophy
(Physics)
in The University of Michigan
2011

Doctoral Committee:

Professor Bing Zhou, Chair
Professor Finn Larsen
Professor Jing Sun
Assistant Professor Jennifer P. Ogilvie
Assistant Professor Junjie Zhu

ACKNOWLEDGEMENTS

I would like to acknowledge those who have so kindly supported me in many different ways, all were an integral part of my academic development leading up to the completion of my Ph.D. work. First and most important are my parents who encouraged my scientific explorations of the world in every year of my life and who's love and support made all my accomplishments easier ones. I also must thank my adviser, Bing Zhou, who provided all the support and consideration that a student could hope for. There has never been any doubt that she was on my side from my first ATLAS muon system work all the way to my dissertation defence.

I would also like to thank a few key figures throughout my academic career. The NASA Space Grant program provided a small amount of undergraduate financial support but more importantly introduced me to Prof. George Parks and Michael McCarthy in the Space Physics group at the University of Washington where I received my first taste of experimental physics. NASA Space Grant also brought together many like-minded students of the sciences who became valuable friends throughout the years. Wonderful mathematical experiences in the UW math honors program and later thoughtful and personalized instruction from professors such as John B. Sullivan were probably the single most important reasons I continued on in graduate school. In Computer Science and Engineering, Anna Karlin and others gave me my first chance at teaching, which I continue to love.

In 2004 we went from a cold, empty CERN lab stacked with crates of muon chambers to a smoothly running commissioning process, and along the way Zhengguo Zhao

taught me much about good management and the particulars of experimental high energy physics. His trust in my work was hugely important to me. The guidance and years of experience that engineers, postdocs, and research scientists such as Helmut Schick, Curtis Weaverdyck, Edward Diehl, and Daniel Levin contributed was a great part of my practical education in physics during my ATLAS years. Later, at DØ Junjie Zhu was another person who went out of his way to provide support in many little ways, this time regarding my physics analysis. Thanks also go to Natasha Panikashvili for the great idea for a DØ analysis topic.

Many others who were a part of the ATLAS experiment, especially the muon community, were of substantial help through the years, though I can't possibly name them all. Even more so, I must acknowledge a huge debt of thanks to all the members of the DØ experiment who contributed so much to making it run effectively long before I came along. Without their valuable contributions to science and future analyzers my work would have been impossible. Thanks, of course, also go to the DOE and indirectly to the American people for their continued funding of high energy physics, fickle though it may be, and my work in particular.

Finally, I would like to acknowledge all the great friends I have made through graduate school, it is difficult to pick a short list. Our shared difficulties and perseverance made our friendships better and more valuable than any I have had. Most significant are James Tung, Jeremy Herr, and my wife Monica. When I first met Monica she was quite a distraction, but these days the support she provides is a tremendous element of my life giving more to this humble physicist than he ever wished for.

TABLE OF CONTENTS

CHAPTER

LIST OF FIGURES

Figure

LIST OF TABLES

LIST OF ABBREVIATIONS

MDT mini drift tube

PDT proportional drift tube

SUSY supersymmetry

PMT photomultiplier tube

CFT central fiber tracker

SMT silicon microstrip tracker

DAQ data acquisition

FNAL Fermi National Accelerator Laboratory

SBC single board computer

CPS central preshower

FPS forward preshower

FPGA field programmable gate array

LM luminosity monitor

IP interaction point

VLPC visible light photon counter

NLSP next to lightest supersymmetric particle

SM standard model

ISR initial state radiation

FSR final state radiation

QCD quantum chromodynamics

MC Monte Carlo

CSG Common Samples Group

EM electromagnetic

HEP high energy physics

NLLR negative log-likelihood ratio

EWSB electroweak symmetry breaking

mSUGRA minimal supergravity

GMSB gauge-mediated supersymmetry breaking

AA Alternative Algorithm

HTF Histogram Track Finder

FH fine hadronic

CC central calorimeter

EC end calorimeter

ECN end calorimeter north

ECS end calorimeter south

BDT boosted decision trees

ANN artificial neural network

BLS baseline substraction

SCA switched capacitor array

WLS wavelength shifting

ICD intercryostat detector

MIP minimum ionizing particle

LHC Large Hadron Collider

AFE analog front end

TFW trigger framework

FEB front end busy

SLHA Supersymmetry Les Houches Accord

QED	quantum electrodynamics
EW	electroweak
LSP	lightest supersymmetric particle
MSSM	minimal supersymmetric standard model
VEV	vaccuum expectation value

ABSTRACT

Search for a Supersymmetry Signature with the $Z\gamma$ Plus Missing Transverse Energy
Final State Using the D0 Detector

by

Alan W. Wilson

Chair: Bing Zhou

A search for a supersymmetry signature is conducted with events containing $Z\gamma$ and large missing transverse energy at Fermilab's Tevatron accelerator with $p\bar{p}$ collisions at center of mass energy 1.96 GeV. The data used in the analysis was collected by the D0 experiment from June 2006 to July 2010 with a total integrated luminosity of 6.2 fb^{-1}. This is the first search for the $Z\gamma$ plus large missing $\not{E}_T$ signature in a hadron collider experiment.

Supersymmetry, a symmetry which relates fermions and boson, is a highly motivated theory extending the standard model of particle physics. This work considers a specific experimental signature from the gauge mediated supersymmetry breaking (GMSB) model. Pairs of neutralinos would be produced and decay to a neutral boson and a gravitino. The production $\tilde{\chi}_1^0\tilde{\chi}_1^0 \rightarrow Z\tilde{G}\gamma\tilde{G}\ \ (Z \rightarrow \ell^+\ell^-)$ predicted by this model is investigated in detail. The experimental signature is two isolated leptons from the Z decay, an isolated photon, and large missing transverse energy due to the two gravitinos, $\tilde{G}$, escaping detection. Two Z decay channels are considered in the

analysis, $Z \to e^+e^-$ and $Z \to \mu^+\mu^-$.

Where the photon has $p_T > 40$ GeV and the missing E_T is larger than 30 GeV for the electron channel and 40 GeV for the muon channel, the predicted number of events from the supersymmetric model with supersymmetry breaking scale $\Lambda = 80$ TeV is 5.2 ± 0.18 and 4.23 ± 0.16 for the electron and muon channels, respectively. No event is observed in the electron channel where the standard model background is expected to be 0.61 ± 0.13 events. In the muon channel 3 events are observed where the standard model background is expected to be 1.55 ± 0.38 events. We conclude that the observed data is consistent with the standard model prediction, no evidence for a supersymmetric signal is found. Employing a boosted decision tree selection process and combining the analysis results from both electron and muon channels we exclude the GMSB model at the 95% confidence level for $70 < \Lambda < 117.5$ TeV, which corresponds to neutralino masses of $111 < \tilde{\chi}_1^0 < 222$ GeV.

CHAPTER 1

Introduction

This thesis presents an experimental search for evidence of supersymmetry (SUSY) which is the most popular candidate for extending the standard model (SM) of particle physics. To potentially create new physics signatures such as supersymmetric particles the Tevatron at Fermilab collides protons and antiprotons head-on with a center of mass energy of 1.96 TeV, the highest in history up until the Large Hadron Collider (LHC) commissioning one year ago.

The data for this work comes from the DØ experiment, which is designed to observe new physics via the high transverse momentum (p_T) products of the Tevatron collisions. For this work we select events involving a photon and leptons, the decay products of the Z boson. We search for a large transverse energy imbalance in the events that could indicate a supersymmetric interaction (known as transverse missing energy or $\not\!\!E_T$).

Our current understanding of fundamental physics, in simple terms, characterizes a family of point-like particles and the forces that govern their interactions. The matter we observe everyday is almost entirely an assemblage of only three particles, the proton and neutron (bound states of quarks), and the electron; and, a mere 80 years ago only the proton and electron along with the forces of electromagnetism and gravitation where known. The theoretical framework developed from experimental observations in the intervening years is a relativistic quantum gauge field theory called the SM. So far the SM quite precisely describes the behaviour of the large family of particles that have been discovered as they interact via the strong force and the unified electroweak force.

The precision to which the SM has been verified is remarkable, in a sense it is the most precisely verified theory ever devised.[3] Nevertheless, the theory has some unverified and unsatisfying features. The source of electroweak symmetry breaking (EWSB), which leads to particle masses, has not been directly tested. The SM assumes EWSB occurs via a scalar particle field called the Higgs. Also, the SM does not connect to gravity which is dramatically weaker than the other forces. But, we know that eventually, when interaction energies approach the Planck scale, gravity must be part of our theoretical framework. Thus there is motivation to consider extensions that include gravity as well. Finally, there are mysteries afield of particle physics mainly in astrophysics that are ripe for a solution that an extension to the SM could provide; in particular is the question of what constitutes dark matter.

SUSY hypothesizes a symmetry between bosons and fermions that implies a family of particles mirroring the ones we know already. Symmetries, both global and local, are fundamental features of physics. At the classical and phenomenological level, global symmetries account for many of the regularities we observe in nature (symmetries of space and time being associated with our classical conservation laws via Noether's Theorem), while local symmetries account for many interactions between the basic constituents of matter. According to the current view in particle physics, most of the fundamental forces in nature, the strong, weak, and electromagnetic interactions, can be described with field theories which have local gauge invariances.

There are a number of appealing features of SUSY which have the power to resolve puzzling elements of the SM. Since supersymmetric particles have not yet been observed they must be massive compared to their partners. Thus the symmetry of SUSY must be broken. There is an analogue to this in the SM where EWSB gives mass to the vector bosons, $W^{\pm}$ and Z. The exact details of a SUSY theory depends on a set of unknown parameters, which in general includes the full mass spectrum of the particles. There is some hope of simplification with assumptions about conservations and the mechanism of SUSY breaking. Research has focued on a few degenerate theories of particular interest: one is minimal supergravity (mSUGRA) and another is gauge-mediated supersymmetry breaking (GMSB). Further description of the SM followed by motivations for SUSY appear in Chapter 2.

The work in this thesis will focus on a predicted signature of GMSB that is accessible at the Tevatron and can be tested with the large datasets available from the DØ experiment. In GMSB the gravitino ($\tilde{G}$), the superpartner to the graviton, is the lightest neutral particle. The supersymmetric particles would eventually decay to the lightest particle and standard model particles which we can observe directly in the experiment. In this work we are interested in a specific scenerio in which the next to lightest supersymmetric particle (NLSP) is a neutralino (neutral partner to the bosons) and its decay to a gravitino also produces Zs and photons (γ). The Z will immediately decay itself, so the final state we are interested in involves two leptons from the Z decay, a photon, and missing energy, where the leptons are either electrons or muons. The missing energy in the event comes from the two gravatinos which pass undetected because the lightest superparticle must interact extremely weakly with the ordinary matter of the detector.

Searches for GMSB have often used the $\gamma\gamma + \not{E}_T$ final state, which is dominate (the *branching ratio* to γ is close to 1.0) at scales that are more easily accessible [4]. In addition, even in regions where the branching to Z is substantial, there is the further branching of Z to leptons (3.3% each) that must be considered (the branching to quarks is buried by a large QCD jet background). On the other hand, a search for

$\gamma\gamma + \not\!\!E_T$ is complicated by the backgrounds from SM $\gamma\gamma$, multi-jet, and $W/Z + \gamma$ faking the signal. There are regions of parameter space where the branching to Z is substantial enough to consider $Z\gamma\not\!\!E_T$. If the Z decays to e^+e^- or $\mu^+\mu^-$ the final state produces a relatively distinct and thus background free signature that makes up for the low branching to electrons or muons (6.6%).

The analysis that follows makes use of data from runs IIb1, IIb2, and IIb3 of the Tevatron and DØ from June 2006 until July 2010. Details of the accelerator complex, detector, data aquisition, and reconstruction algorithms for this period fill Chapters 3 and 4. Chapter 5 describes the $Z\gamma + \not\!\!E_T$ search using 6.2 fb^{-1} of data. The observed events are constistent, up to uncertainty, with SM backgrounds. We summarize these results and exclude a region of the GMSB model in Chapter 6.

1.1 Conventions

Before we begin, a few notes about conventions. Througout, all momenta and masses will be measured in natural units where $c = 1$; and the units of energy, momentum, or mass will typically be presented in giga-electron volts, GeV, or at times three magnitudes up or down, MeV or TeV. Thus the mass of the Z boson, 91.2 GeV/c^2, is simply 91.2 GeV and the relation $E^2 = m^2c^4 + |p|^2c^2$ is simply $E^2 = m^2 + |p|^2$.

Also, take special note of the coordinate system described in Section 3.2.1. The quantities η and ΔR will be used extensively. In brief, η is a reparametrization of the inclination from the colliding beam axis, θ, that makes certain distributions more uniform.

CHAPTER 2

The Standard Model and Supersymmetry

2.1 The Standard Model of Particle Physics

2.1.1 Many particles

"Who ordered that?" - Isidor I. Rabi

As introduced in the previous chapter, the full compliment of forces and the proliferation of particles that we know of today originate from a host of experimental discoveries in the 1930s. In that decade we came to know of a neutral partner to the proton, the neutron; a heavy partner to the electron, the muon; a oppositely charged partner to the electron, the positron; and, finally, two new short-range forces, the nuclear and weak. Additional particles were already hypothesized: moderately heavy particles called mesons could be the carriers of the nuclear force (though initially the muon was mistaken for one of these particles), and extremely light and weakly interacting particle called the neutrino would explain the missing energy in some interactions.

It wasn't until 1947 that a true meson was observed, the pi meson or pion; and it wasn't until the 1950s that the first neutrino was directly detected. In the 1960s and 70s it became clear that the neutron and proton are not fundamental and are instead made of three quarks, particles that to the limits of current experiment are point-like.

The nuclear force that holds protons and neutrons together in a nucleus turned out to just be a residual effect of a much stronger force, aptly named the strong force, that binds the quarks together within these particles. Particles made of quarks are know as hadrons.

Despite the proliferation of particles, physicists were remarkably successful at wrangling them together into one unified theory, what is called the SM of particle physics. The SM describes all the interactions of the fundamental particles, quarks and leptons, connecting them via an additional family of particles, the bosons. The theory has survived many tests and today lacks direct evidence of only one important component, the higgs field. The higgs boson would be the only fundamental spin-0 particle in the SM and is a critical prediction arising from the hypothesized symmetry breaking process that gives particles mass.

The SM describes 12 fundamental fermions, which are particles with half-integer spin that obey Fermi-Dirac statistics. For each of these fermions there is an antiparticle of identical mass but opposite charge. They come in three generations, where each generation is identical to the last except for the masses; they are listed in Table 2.1. The leptons come in pairs starting with the electron and the electron neutrino. The electron has charge -1 and interacts via the electromagnetic and weak forces. The neutrino has no charge and interacts only via the weak force. In the second and third families the charged leptons are the muon and the tau and each is paired with a neutrino. *Note:* though the standard definition of "lepton" refers to all these particles, following common usage the analysis portion of this work will typically use"lepton" to refer only to electrons, muons, and their anti-particles. There are also six quarks and their anti-particles. The down and up quarks are the lightest and they are what make up protons, neutrons, and pions. Like the leptons they have spin 1/2. The quarks are the only particles with fractional electric charge, down and up have charges -1/3 and +2/3, respectively. The strange and charm followed by the bottom and top quarks mirror the down and up, but with increasingly larger masses. All the quarks are permanently bound in hadrons by the strong force and a hard scattering event that would eject a quark is accompanied by hadronization on a distance scale similar to the size of the proton. Hadronization is a process in which quark-antiquark pairs are created in the vacuum by strong force energy and combine to form new hadrons. The one exception to this is the top quark which is so massive (172 GeV) that it decays before hadronizing.

In addition to the fermions there are four types of gauge bosons, particles with integer spin obeying Bose-Einstein statistics and arising from a gauge theory. These bosons mediate the electromagnetic, weak, and strong forces. The photon is massless and involved in electromagnetic interactions, the massive $W^{\pm}$ and Z bosons are involved in the weak interaction, and the gluons (which come in eight flavors) are involved in strong interactions. One particle fundamental to the theory remains undiscovered, a scalar (spin-0) boson which gives particles mass, called the Higgs boson. There may also be a massless spin-2 boson associated with gravitation, the graviton, but it has not been observed. The observed bosons and their masses are summarized in Table 2.2.

2.1.2 Relativistic quantum gauge field theories

The standard model is a relativistic quantum field theory. A field theory defines a quantity $\psi(x)$ for all points of space and time. In a relativistic field theory this quantity must be invariant under Lorentz transformations of spacetime x. In a quantum field theory the field values are not directly observable, instead the observables are defined by Hermetian operators which act on the field. Quantum excitations of the fields are the point-like particles we observe.

The SM is also a gauge field theory. The specific gauge structure of the SM is one of its defining features. A gauge field theory is one in which certain transformations

Table 2.1: This enumerates the fundamental fermions of the SM and their masses. The lighter quark masses are somewhat hard to define because they are only observed bound within hadrons and are surrounded by a gluon field with much greater mass/energy. Because of this the quark masses depend on a model which in this case is QCD perturbation theory with the $\overline{\mathrm{MS}}$ renormalization scheme and scale $\mu = 2$ GeV; the u, d, and s-quark masses are "current quark masses" and the c and b-quark masses are "running masses." Neutrinos are known to have mass because they have been observed to oscillate between flavors, suggesting that their flavor and mass eigenstates are different and they have non-zero mass differences. Their exact masses are not well known, and neutrino masses are not part of the SM. [2]

Generation	Quark	mass	Lepton	mass
1st	up (u)	1.7-3.3 MeV	electron (e)	0.511 MeV
	down (d)	4.1-5.8 MeV	neutrino (ν_e)	< 2 eV
2nd	strange (s)	100 MeV	muon (μ)	105.7 MeV
	charm (c)	1.3 GeV	neutrino (ν_μ)	$< .19$ MeV
3rd	bottom (b)	4.5 GeV	tau (τ)	1777 MeV
	top (t)	172 GeV	neutrino (ν_τ)	< 18 MeV

Table 2.2: The fundamental bosons of the SM. [2]

Force	Boson	mass
Electromagnetic	photon (γ)	0
Weak	Z	91.2 GeV
	$W^\pm$	80.4 GeV
Strong	gluons (g)	0
Higgs mechanism	h	> 115 GeV
		< 158 or > 175 GeV [5]

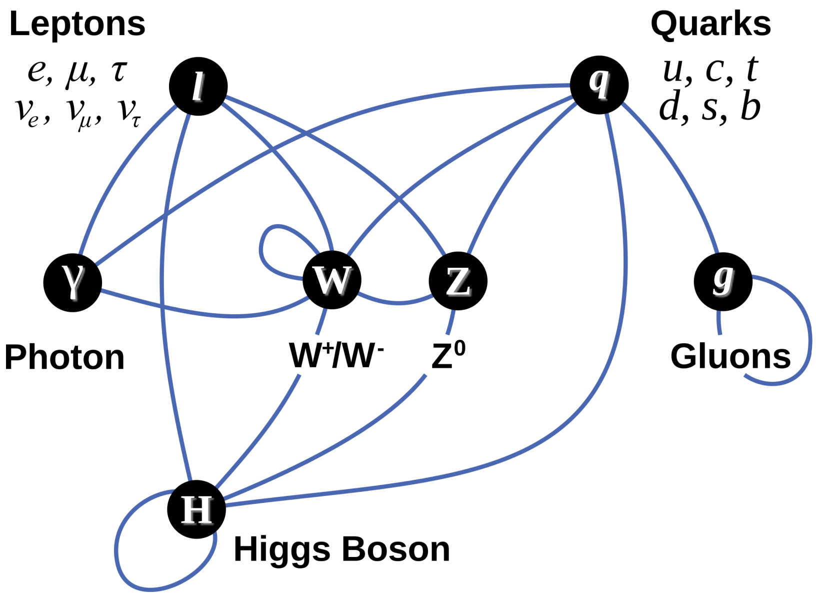

Figure 2.1: Connections on this graph indicate tree-level interactions between particles in the standard model. Fermions that make up matter are on the top, the force carrying vector bosons are in the middle, and the scalar Higgs boson is on the bottom. Notice the vector bosons only couple to particles that carry their type of charge: EM for photons, weak for W and Z, and strong for gluons. The Higgs boson only couples to particles with mass.

of the field leave the observable quantities unchanged. [1] For example, for a one-dimensional wavefunction, $\psi(x)$, where the modulus $|\psi(x)|$ is the observable one can apply a shift in phase

$$|\psi(x)| = |e^{i\phi}\psi(x)| \tag{2.1}$$

With no change in the observable. In fact, the phase ϕ can be taken to be different at different x, $\phi = \phi(x)$, and again no change should be expected. This is called a local gauge invariance.

One can characterize a gauge theory by the underlying symmetry defined by its gauge transformations. In the one-dimensional wavefunction example the symmetry is simply the one-dimensional unitary group, $U(1)$, but more complicated symmetries

---

[1] The term "gauge" derives from Hermann Weyl's usage when he unsuccessfully tried to connect electromagnetism to gravitation via a scale invariance. A gauge is a choice of scale, thus the naturalness of the term for Weyl's purposes, but the gauge transformations in the SM will turn out to be more akin to rotations rather than to scalings.

are possible. The underlying symmetry presumed by the SM is

$$U(1)_Y \times SU(2)_L \times SU(3)_C \tag{2.2}$$

but there may be additional symmetries as yet undiscovered. (Extensions to the SM may, for example, include these symmetries as a subset of a larger $SU(5)$ symmetry.) The structure of the gauge symmetries turns out to define the critical features of a gauge theory. In the case of the SM the four electroweak bosons γ, $W^{\pm}$, and Z are associated with combinations of the four generators of $U(1)_Y \times SU(2)_L$, where $U(1)_Y$ is known as the *hypercharge* component and $SU(2)_L$ is the *isospin* component.

To see how gauge invariance for a fermionic field naturally leads to force carrying bosons start with the Dirac Lagrangian for a free spin-1/2 fermion,

$$\mathcal{L}_0 = i\bar{\psi}(x)\gamma^\mu\partial_\mu\psi(x) - m\bar{\psi}(x)\psi(x) \tag{2.3}$$

The first term is the kinetic component and the second term the mass component. Now apply a local phase change

$$\psi(x) \to \psi'(x) = e^{i\phi(x)}\psi(x). \tag{2.4}$$

This leaves the mass term unchanged but alters the kinetic term such that $\mathcal{L}_0$ is clearly not gauge invariant,

$$\partial_\mu\psi(x) \to e^{i\phi(x)}(\partial_\mu + i\partial_\mu\phi(x))\psi(x). \tag{2.5}$$

One perspective on this situation is that we are not using a meaningful derivative and in fact if there is local phase invariance then we need to instead be using the convariant derivative,

$$D_\mu = \partial_\mu + ieA_\mu \tag{2.6}$$

where there is a a vector (spin-1) field $A_\mu(x)$ that transforms as

$$A_\mu(x) \to A_\mu(x) - \frac{1}{e}\partial_\mu\phi \tag{2.7}$$

See [6, p. 482-6] for more detail as to how we are naturally lead to this. Notice that now

$$\begin{aligned} D_\mu\psi(x) &\to \left[\partial_\mu + ie\left(A_\mu - \frac{1}{e}\partial_\mu\phi\right)\right] e^{i\phi}\psi(x) \\ &= e^{i\phi}\left[i\partial_\mu\phi + \partial_\mu + ie\left(A_\mu - \frac{1}{e}\partial_\mu\phi\right)\right]\psi(x) \\ &= e^{i\phi}D_\mu\psi(x), \end{aligned} \tag{2.8}$$

so $\bar{\psi}\gamma^\mu D_\mu\psi$ is invariant. The invariant kinetic term for A_μ is $\frac{1}{4}(F_{\mu\nu})^2$ where $F_{\mu\nu} = \partial_\mu A_\nu - \partial_\nu A_\mu$, so putting this all together we are lead to the gauge invariant Lagrangian

$$\begin{aligned} \mathcal{L}_1 &= i\bar{\psi}\gamma^\mu D_\mu\psi - m\bar{\psi}\psi - \frac{1}{4}(F_{\mu\nu})^2 \\ &= i\bar{\psi}\gamma^\mu\partial_\mu\psi - m\bar{\psi}\psi - e\bar{\psi}\gamma^\mu A_\mu\psi - \frac{1}{4}(F_{\mu\nu})^2. \end{aligned} \tag{2.9}$$

This has a kinetic term for the fermion, a mass term for the fermion, an interaction term for the fermion and the boson, and a kinetic term for the boson. A mass term like $m^2A^\mu A_\mu$ for the boson would not be invariant and so it must be massless. This is essentially quantum electrodynamics (QED) where this Lagrangian expresses the interaction between an electron, the field ψ, and a photon, the field A_μ.

2.2 Deficiencies of the standard model

A clear deficiency of the standard model is that it makes no mention of gravitation. Gravity is far too weak to be important in the interactions we produce in the lab. The scale at which quantum gravitation effects would become important is called the Planck scale and it is huge, $M_p \approx 10^{19}$ GeV, 17 orders of magnitude above the weak scale at around 100 GeV. So, we are left to wonder, what happens in the intervening energy region?

Of significant concern is what is called the hierarchy problem. If we assume the standard model is an effective theory which approximates a more fundamental theory at a high energy scale, then when one considers the radiative corrections to the higgs mass a worrying situation arises. Virtual fermion loops contribute to a correction of the squared Higgs mass that diverges quadratically in the energy scale. The trouble is that the Higgs mass must be near the electroweak (EW) scale ~ 100 GeV and yet if there is not new physics between the EW scale and the Planck scale then these huge corrections must cancel with incredibly fine tuning (to the 24th decimal place!) Of course this could be possible, but to many such a cancellation feels very unlikely.

Another issue to consider is the great differences between the forces. It is hoped, but not certain, that the forces unify at a high energy scale near the Planck scale in much the same way as electromagnetism was unified with the weak force via electroweak theory. Georgi, Quinn, and Weinberg predicted the dependence of the SM gauge couplings on energy scale and noted that within the experimental errors at the time the three scales could intersect around 10^{14} GeV [7], see Figure 2.2.

Finally, there is the issue of dark matter. It has been found that none of the SM particles can sufficiently describe the dark matter phenomena in our Universe. Something forms a larger portion of the material universe than anything that we can directly observe; and it must interact extremely weakly with ordinary matter. Could this lurking presence be the product of new physics beyond the SM?

Figure 2.2: Running of gauge couplings as a function of energy, Q. The solid line is the SM, the dotted (dashed) line is for MSSM with 1 TeV (10 TeV) SUSY mass scale.

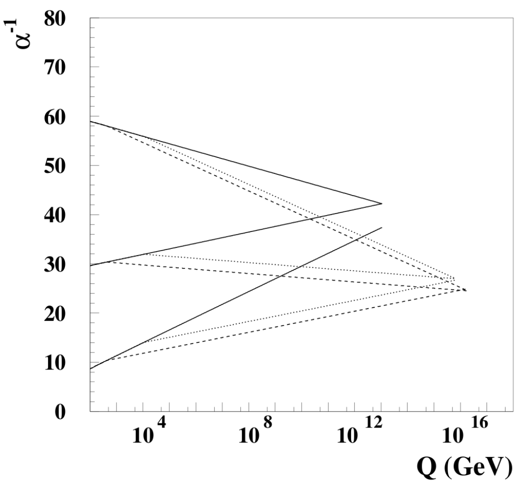

2.3 Supersymmetry

Extensions of the SM can be formed very generally by assuming additional underlying symmetries. In SUSY the assumption is made that the fermions and bosons are actually connected via a symmetry, Q, transforming each fermion to a boson and each boson to a fermion. Thus we have

$$Q|\text{fermion}\rangle = |\text{boson}\rangle \qquad Q|\text{boson}\rangle = |\text{fermion}\rangle. \tag{2.10}$$

It turns out that if this happens the symmetry must apply to all fermions and bosons in nature. Thus our large family of particles doubles, and this must even include a partner to the graviton, the extremely weakly interacting boson we presume is associated with gravitation. Naming of these new particles follows a convention of prefixing the fermion partners with 's' (which are **s**calar bosons) and suffixing the bosons with '-ino', thus getting for example 'slepton', 'stau', 'wino', and 'gravitino'. See [8] for a short introduction to SUSY and [9] for more detail.

Supersymmetry is appealing theoretically in a number of ways. Refering back to Figure 2.2, it has been found that the three couplings do not infact converge at

Figure 2.3: The quantum correction to m_H^2 via a single fermion loop and the correction from its boson partner in SUSY are proportional to Λ^2 but cancel to a quantity proportional to $\ln \Lambda$.

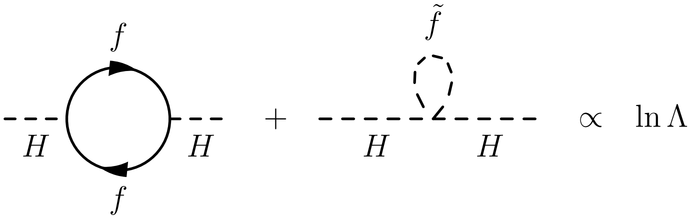

high scale assuming SM particles alone. But, with the addition of supersymmetric particles in the minimal supersymmetric model the curves can be made to converge with a SUSY breaking scale at the TeV level, not far above the EW scale and within reach of experiment [8].

A supersymmetric reality may also be behind the struggle to discover the Higgs. One feature of SUSY is that two Higgs doublets are require to give the fermions mass, this would be physically manifest as three neutral Higgs particles (where the SM has one). These supersymmetric Higgses would have somewhat different production and decay properties that make it more likely that they have evaded discovery.

SUSY also addresses the hierarchy problem quite nicely. In the SM we have virtual fermion loop corrections to the Higgs mass that contribute corrections that could be huge relative to the EW scale. But in SUSY the corrections are exactly cancelled by corresponding virtual scalar loop corrections. Finally, there is the issue of dark matter. The lightest supersymmetric particle (LSP) of a supersymmetric theory would be a very good candidate for the massive but very weakly interacting matter content of the universe.

For a summary of the current state of SUSY searches see [10].

2.3.1 Gauge Mediated Supersymmetry Breaking

Despite it's nice features, we know already that supersymmetry, if it exits, cannot be an unbroken symmetry. There is no evidence, for example, of a boson with the mass and charge of the electron. If a slepton exists, it must have mass significantly larger than the current reach of experiment, and this is true of nearly all the other supersymmetric particles. Thus, for the theory to apply to nature the supersymmetry must be broken. Exactly how the supersymmetry is broken will produce different spectra of particle masses. In this study we will assume gauge-mediated supersymmetry breaking (GMSB) is responsible.

In GMSB there are a set of chiral supermultiplets called messengers which communicate the supersymmetry breaking from the hidden breaking sector to the minimal supersymmetric standard model (MSSM) portion via the gauge bosons of the SM $SU(3)_C \times SU(2)_L \times U(1)_Y$ gauge symmetries and via the supersymmetric gauginos. Because the messangers communicate the breaking via SM gauge interactions the particles aquires masses related to the strength of their gauge interactions, squarks are heavier than sleptons, the gravitino is the LSP, and the NLSP is usually either a neutralino or stau. The hyper charge gaugino is usually the lightest component of the neutralino (the superpartners don't have to be the same as the mass eigentstates, there can be mixing), and this is where γ decays are favored.

There are 120 free parameters in the MSSM but the assumptions of the GMSB model reduce this number dramatically. In the minimal version of GMSB the masses and branching fractions are determined by six parameters

$$\Lambda, \quad M, \quad n_5, \quad \tan\beta, \quad \mathrm{sgn}(\mu), \quad C_{\mathrm{grav}} \tag{2.11}$$

The two scale parameters are Λ and M. Λ is loosely known as the "breaking scale," though more precisely the breaking scale is $\sqrt{\Lambda M}$. The messanger scale is M. Production cross sections decrease exponentially with increasing scale, and these values can be as much as hundreds of TeV for models observable at the Tevatron. The parameter n_5 is the number of complete $SU(5)$ multiplets (a positive integer), and μ is the superpotential Higgs mass parameter (around the EW scale, hundreds of GeV). SUSY requires a Higgs field with two complex doublets, $\tan\beta$ is the reatio the vaccuum expectation values (VEVs). The parameter C_{grav} is another ratio of VEVs comparing hidden sector to messenger sector.

The C_{grav} parameter determines how quickly the NLSP decays to a gravitino. If this parameter is large enough this decay may happen while traversing the detector or beyond. The result would be a unique signature, especially in the case when the NLSP is charged and thus observed in the trackers. A charged NLSP stable enough to pass through the detector would have the signature of a slow-moving muon [11]. This is not a scenario we will explore here so we will assume $C_{\text{grav}} = 1$, giving a prompt decay.

2.4 Model Line E yielding the $Z\gamma + \not{E}_T$ signal

The GMSB model we will be focus on is the "Model Line E" originating in [12]. The idea is to construct a model with a higgsino-like neutralino that has substantial decays to $Z\tilde{G}$. A small deviation from the minimal GMSB model is required, as plausible as any, to produce this unique phenomenology.

The model takes the values

$$M = 3\Lambda, \qquad n_5 = 2, \qquad \tan\beta = 3, \qquad \mu = \frac{3}{4}M_1, \qquad C_{\text{grav}} = 1. \tag{2.12}$$

where we consider one free parameter, the supersymmetry breaking scale Λ. In the minimal model the magnitude of μ is determined by the other parameters and is generally larger than $\frac{3}{4}M_1$, but for large enough values stau ($\tilde{\tau}_1$) becomes the NLSP. The model is relatively insensitive to the choice of $\tan\beta$: with increasing $\tan\beta$ the $\tilde{\chi}_1^0 \to Z\tilde{G}$ decay becomes slightly more important but at the same time the production cross section decreases. In short, this model sits close to a local maximum for $Z\tilde{G}$

Figure 2.4: In (a), the Feynman diagram for an important chargino/neutralino production considered in this work. In (b), an example cascade decay to $\tilde{\chi}_1^0$, the NLSP, producing two charged leptons along the way. The products of cascade decays have relatively low energy and are not considered in our signal signature.

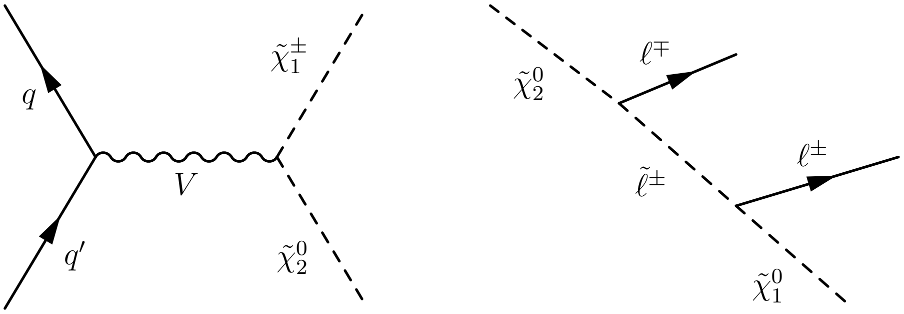

(a) (b)

production [13]. This is certainly not the only source of the $Z\gamma + \not{E}_T$ signature among the spectrum of potential SUSY models but it provides a plausible and concrete example for this analysis.

The important productions in model line E are

$$p\bar{p} \to \tilde{\chi}_1^0\tilde{\chi}_1^\pm, \quad \tilde{\chi}_1^\pm\tilde{\chi}_1^\mp, \quad \tilde{\chi}_2^0\tilde{\chi}_1^\pm, \quad \tilde{\chi}_1^0\tilde{\chi}_2^0 \tag{2.13}$$

and the Feynman diagram for the third of these is shown in Figure 2.4(a) where a second generation neutralino and a first generation chargino are coupled to the colliding quarks via a vector boson. In all cases productions that involve states heavier than the NLSP decay quickly via a cascade decay such as in Figure 2.4(b) that may produce multiple leptons. The cascade decay leptons create a unique trilepton signature that is often used as a SUSY search signature [14, 15]. (At the LHC same-sign trilepton or four lepton searches may even be considered [16].)

For our model the products of the cascade decay are quite soft and rarely reconstructed in DØ . Thus we focus only on the decay of the $\tilde{\chi}_1^0$ pair. In model line E the branching to $Z \to \ell\bar{\ell}$ is substantial but not overwhelming for the accessible values of Λ, so though one may want to consider final states such as $ZZ + \not{E}_T$, $h\gamma + \not{E}_T$, and

Figure 2.5: A generalized Feynman diagram for the production of the $\ell^+\ell^- + \gamma + \not{E}_T$ final state via light neutralino decays to Z or γ plus a gravitino. The blob contains pair production of neutralinos, charginos, or a combination followed by a cascade of decay to the lightest neutralino, see Figure 2.4 for an example.

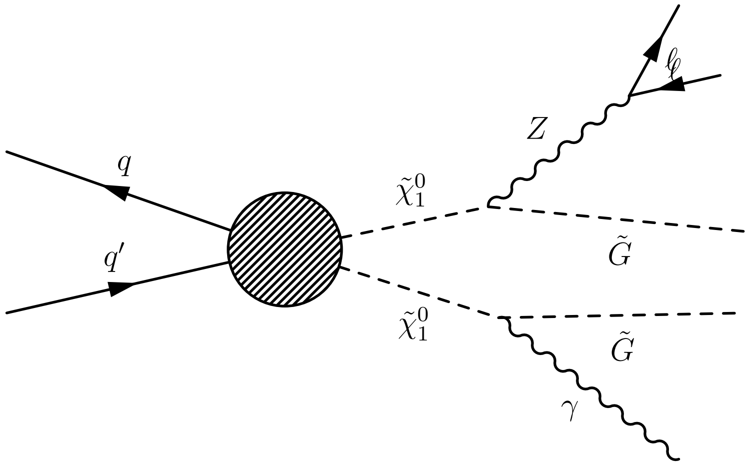

$hZ + \not{E}_T$, they are difficult to justify. The squared branching fraction to leptons for ZZ is especially troublesome but may have some prospects at a higher energy collider such as the LHC. (The branching of Z to a single charged lepton type is 3.3% so the branching of ZZ to electrons or muons is only $(0.066)^2 = .44\%$.) We focus on $Z\gamma + \not{E}_T$, the general diagram of which is shown in Figure 2.5, where the cascade decays and resulting soft leptons occur within the central blob.

The NLSP branching and total cross section to photons and leptons are shown in Figure 2.6. The Z decay is only important for $\Lambda > 65$ GeV and it exceeds the γ decay for $\Lambda > 83$ TeV. Because of the steeply falling production cross section the $Z\gamma$ and ZZ channels have peak production near the turn-on around 80 TeV. The total cross section in this figure includes the branching ratio of $Z \to \ell\bar{\ell}$ where $\ell = e$ or μ, One sees that even in this model $\gamma\gamma$ is more frequently produced; but background rejection is harder in a $\gamma\gamma$ analysis. A quick estimate based on a comparison of the results of this work to the recent DØ $\gamma\gamma + \not{E}_T$ result [17, 18] suggests that $Z\gamma$ gets comparable sensitivity with roughly a factor of 4 fewer events.

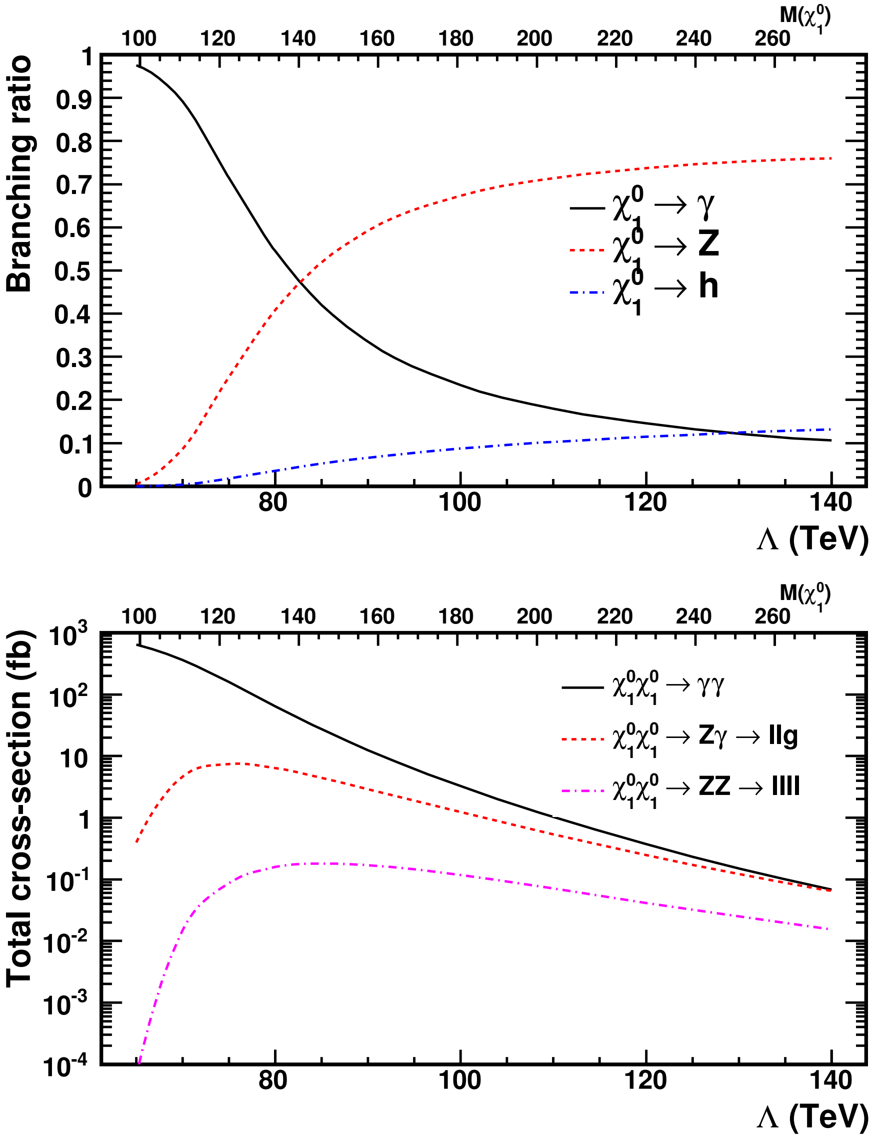

Figure 2.6: The branching ratio of $\tilde{\chi}_1^0 \rightarrow \gamma/Z/h + \tilde{G}$ (top) and total cross section including production and branching of $Z \rightarrow e\bar{e}$ or $\mu\bar{\mu}$ (bottom) from model line E as a function of Λ. The top axis gives the mass of the NLSP, $\tilde{\chi}_1^0$.

CHAPTER 3

The Tevatron Accelerator Complex and DØ Detector

A complex of accelerators and storage rings at Fermi National Accelerator Laboratory (FNAL) produces as the end result head-on collisions of protons with antiprotons, where the proton-antiproton center-of-mass energy is 1.96 TeV. The final stages of this process happen in the Tevatron, a storage ring four miles in circumference. At one of the two interactions regions around the accelerator the DØ detector is used to monitor the results of the collisions. The equipment used for this analysis has been upgraded from it's original design to higher luminosity operation and is known as Run II.

Table 3.1: The maximum energy of a proton/antiproton in each accelerator in the FNAL complex.

Accelerator	Maximum energy
Cockcroft-Walton	750 keV
Linac	400 MeV
Booster	8 GeV
Main Injector	150 GeV
Tevatron	980 GeV

3.1 Accelerators

The transition from a bottle of helium gas (average kinetic energy 1/40 eV) to protons and antiprotons with 980 GeV of energy requires many stages. The maximum energy after each stage is shown in Table 3.1, and the layout of the accelerators is shown in Figure 3.1. The process begins when helium gas is ionized to H^- and accelerated to 750 keV by the Cockcroft-Walton pre-accelerator. The Linac accelerates these ions further and sends them through a foil, stripping them down to protons, as they are injected into the Booster. Protons are accelerated in the Booster and then the Main Injector after which they are either injected into the Tevatron or used to produce antiprotons. The antiprotons pass through the Debuncher and are stored temporarily in the Accumulator. Periodically the Accumulator is emptied into the the Recycler where the antiprotons are are stored until ready for injection, via the Main Injector, into the Tevatron. The process of filling the Tevatron in preparation for collisions is called *shot setup* and the period when a set of particles circulate in the Tevatron, typically colliding at 980 GeV, is a *store*.

An overview of the Tevatron design and performance for RunIIa is given in [19] with more detail in [20] and upgrades for RunIIb in [21]. Updates and far more details about operations be found in [22].

3.1.1 Cockcroft Walton Pre-Accelerator

The H^- ions that begin the acceleration process are created using a magnetron surface plasma source. The device is made up of a rectangular molybdenum cathode surrounded by an anode with a 1 mm gap. Hydrogen gas is introduced 15 times per second and a 40 A arc is formed between the two surfaces for 80 μs. A 0.1 T magnetic field applied parallel to the anode/cathode pulls electrons into violent spirals that lead to full ionization of the hydrogen. The H^+ ions migrate to the cathode where they occasionally collect two electrons, a process that is enhanced by the addition of cesium

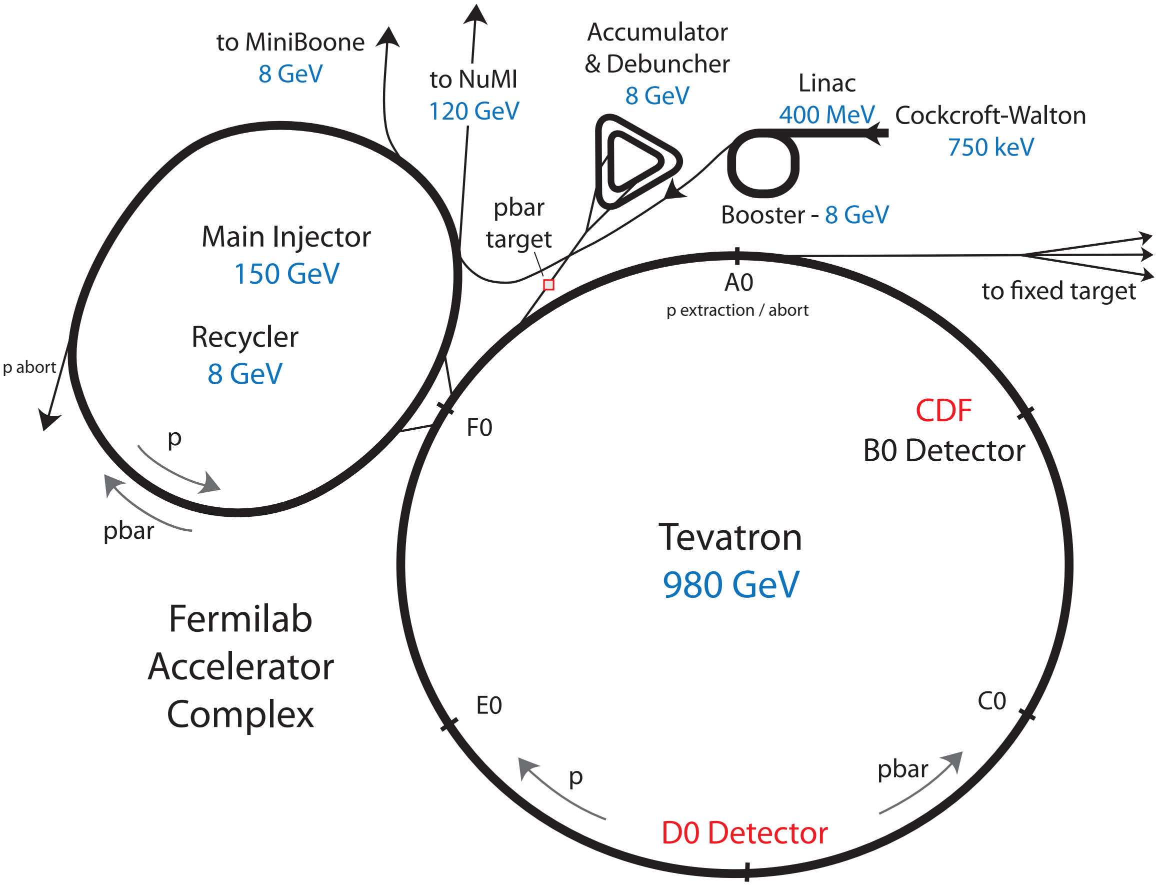

Figure 3.1: Map of the FNAL accelerators shown roughly to scale. The indicated energies are the maximum for that accelerator or storage ring. The Recycler is just above the Main Injector, and the Accumulator is just inside of the Debuncher.

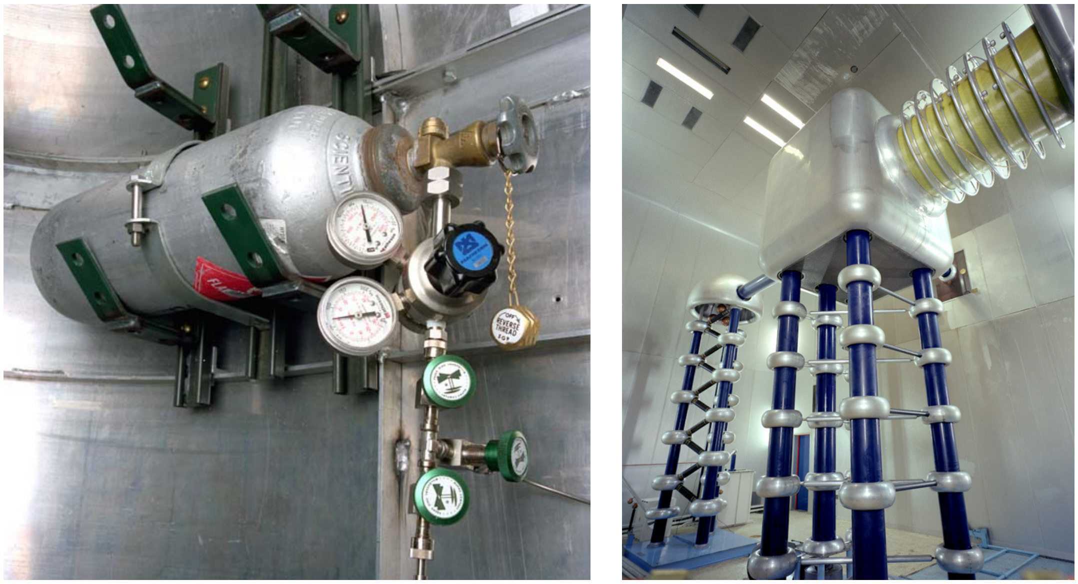

Figure 3.2: The hydrogen gas from which the accelerated protons are derived (left), and the Cockcroft-Walton accelerator which employs a 750 kV static electric field (right).

vapor. The resulting H^- ions and electrons are pulled out of the source with a pulsed 18 kV plate. A magnet separates out the H^- ions, bends them 90°, and focuses them. The result is a 50-80 mA beam.

This process all happens within a chamber held at -750 kV with respect to ground. The extreme voltage is created by a standard 5-stage capacitor and diode voltage multiplying ladder, but on a massive scale: a 19 ft tall tower. A transformer supplies 75 kV of oscillating current that is doubled for each of the 5 stages. Roughly, the diodes allow the capacitors to charge in parallel to the peak-to-peak voltage (150 kV) but only allow them to discharge in series (so $5\times$ 150 kV = 750 kV). All the equipment required for controlling and monitoring the ion source is contained within the 750 kV dome. Power comes from a generator in the dome powered by a shaft running up one leg of the tower, and data is communicated by fiber optic cables.

The H^- leaving the source at -750 kV are accelerated toward the room wall which is at ground potential, thus gaining 750 keV. Finally, depending on the needs of later accelerator stages, the 80 μs bunches are trimmed down to 10-57 μs bunches by an

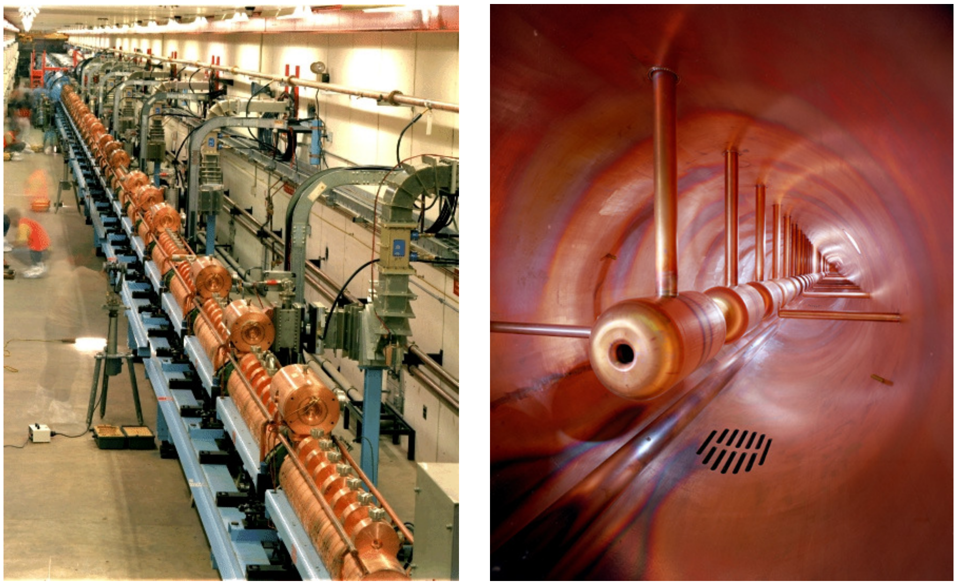

Figure 3.3: In the left image the copper-colored tube apparatus is the high energy (800 MHz) portion of the Linac. Grey, rectangular waveguides feed the 800 MHz RF energy from Klystron amplifiers (not shown). In the background can be seen the larger blue vessels containing the low energy (200 MHz) portion of the Linac. The right image shows the internal structure of the low energy section.

electrostatic chopper as they head toward the Linac.

3.1.2 Linac

The Linac accelerates the H^- ions from 750 keV to 400 MeV. It is made up of two sections. The first section is a drift tube linac which can be seen at right in Figure 3.3. This section is made up of five water-cooled vessels containing a series of suspended copper tubes. A power amplifier applies a 201.24 MHz signal along the vessel such that ions traveling between two tubes may experience a potential difference. The tube lengths are designed such that the H^- ions experience an accelerating potential difference when they are between tubes and they are shielded from the decelerating half of the cycle while drifting inside a tube. At the end of the drift tube section the ions have been accelerated to 116 MeV.

Ions arriving out of phase with the 200 MHz signal would experience a decelerating force, and in fact the stable phase in the drift tube section is only 105°of the cycle. To increase efficiency there is a single RF cavity buncher before each of the Linac stages. The first buncher groups the ions such that effectively 240°of the cycle are captured. The second buncher squeezes further on the bunches to match the narrower stable phase in the high energy section.

The second, higher energy section of the Linac, seen at left in Figure 3.3, uses side coupled cavities which provide three times the accelerating gradient of the drift tube portion. Instead of one cavity containing many drift tubes this section has many cavities coupled together. There is one cavity for each half cycle, alternately containing an accelerating and a decelerating field. The RF power operates at four times the drift tube frequency or 804.96 MHz, so bunches travel eight cavities apart. The side coupled cavities are grouped into seven sections, and each section is powered by a 12 MW Klystron. In total this half of the Linac is 64 m long.

3.1.3 Booster

The Booster is a synchrotron that accelerates protons from 400 MeV to 8 GeV. It is 151 m diameter and is made up of 96 combination dipole/quadrupole magnets and 17 cavity resonators. It operates on the same 15 Hz cycle as the Cockcroft-Walton and Linac, accelerating bunches in 33 ms before injection into the Main Injector. One turn in the Booster is 2.2 μs but the Linac provides a pulse about 40 μs long; a chopper is used to select a portion of this pulse to fill a whole number of turns, usually not more than 5 or 6.

The filling of the Booster is the point at which the H^- are stripped of their electrons to create a proton beam. The Linac H^- beam is first debunched, removing the 200 MHz bunch structure required by the Linac in favor of a tighter momentum spectrum. It is then brought parallel with the circulating proton beam in the Booster, about 8 cm away. During filling two dipole magnets displace the proton beam in the Booster toward the oppositely charged H^- beam from the Linac such that the two beams combine. The combined beam passes through a carbon foil which strips electrons from the H^-. The resulting particles pass through another pair of dipoles which displace the resulting protons back into the Booster. and the stripped electrons into a dump.

Unlike in the Main Injector and Tevatron, the Booster uses magnets that serve both as dipoles and quadrupole, called gradient magnets. The field lines in the gradient magnet are roughly vertical, but they bow horizontally in or out of the bending radius. This is accomplished with laminated steel forming a wedge shaped beam gap; when the larger vertical gap is toward the inside of the dipole bending then the field bows inward creating a vertical defocusing and the field strength increases outward creating a horizontal focusing.

The magnets are grouped into 24 sections made up of two focusing magnets separated by a short straight section and two defocusing magnets separated by a long straight section. Acceleration is accomplished by 17 cavities located in eight of the long straight sections. The cavities operate at a frequency 84 times the revolutions frequency, starting at 38 MHz after injection and ending at 53 MHz before extraction.

3.1.4 Main Injector

The Main Injector is a large synchrotron, about half the size of the Tevatron, that replaced the duties of the Main Ring for Run II. It operates in at least five different modes depending on the needs of the complex. The Main Injector accelerates the 8 GeV protons from the booster to 150 GeV and either injects them into the Tevatron or sends them to the fixed target experiments. It also uses protons from the Booster, accelerated to 120 GeV, to produce antiprotons. Finally, antiprotons stored in the Accumulator or the Recycler at 8 GeV also need to be accelerated to 150 GeV and injected into the Tevatron.

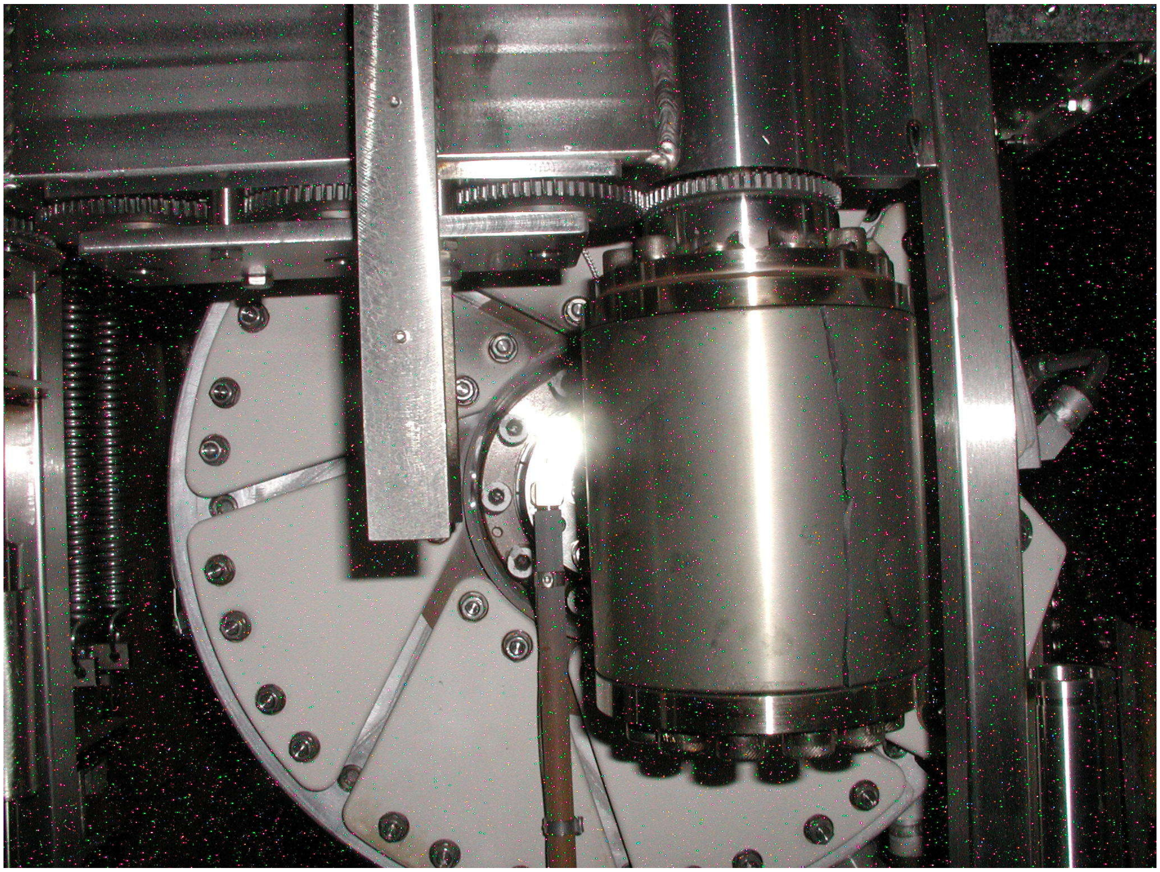

Figure 3.4: The nickel target used to produce antiprotons with the lithium lens behind it. The aperture of the lithium lens is just out of view behind the target. Air flows through the target for cooling, and gearing at the top rotates it to even out heating from the narrow beam. This target has cracked will be replaced. The colored speckles in the picture are from residual radiation after a 6 hour cool-down period.

3.1.5 Antiproton Source

The Antiproton Source uses 120 GeV protons striking a nickel target, seen in Figure 3.4, every 2.4 seconds to produce antiprotons. The target is a cylinder of nickel (in the past short nickel cylinders were stacked with copper to improve heat dissipation). The cylindrical shape is convenient because it can be rotated to spread the radiation exposure around the target and the thickness of the target is easily adjusted by striking a different cord of the circular cross section. A small fraction of the scattering antiprotons are captured and focused by a lithium lens. The lithium lens is a solid rod of lithium 1 cm in diameter and 15 cm in length. A current of

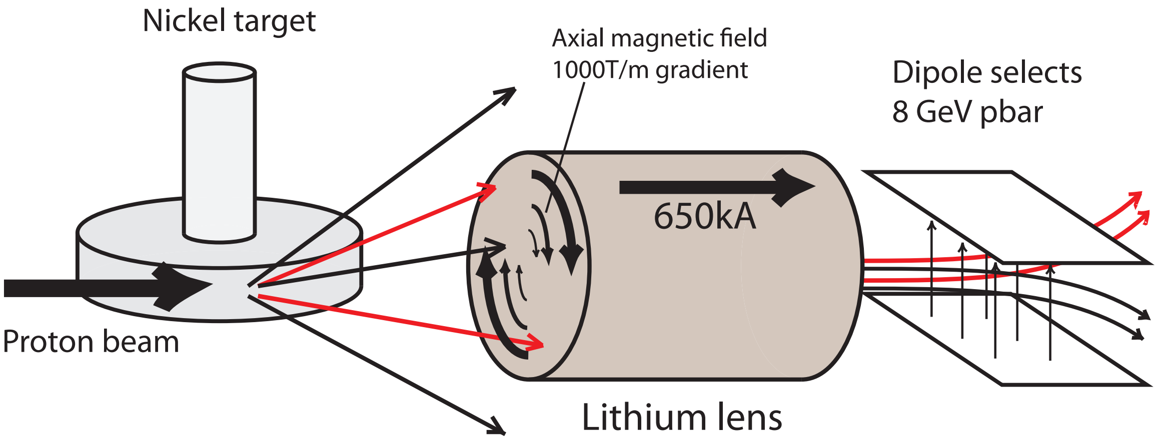

Figure 3.5: Antiprotons are created by striking a nickel target with 120 GeV protons. The antiprotons are focused by a the axial magnetic field formed by pulsing a cylinder of lithium with 650 kA of current. Finally, a dipole magnet selects 8 GeV antiprotons.

650 kA is pulsed lengthwise through the lithium to produce an axial magnetic field that increases radially with a gradient of 1000 T/m. The field bends stray particles back toward the center of the lens. Just past the lens is a pulsed dipole magnet that selects only negatively charged particles with energy near 8 GeV. See Figure 3.5 and [23] for an illustration of this whole process. The resulting efficiency is 1 antiproton in the accumulator for every 50,000 protons striking the target.

The antiprotons are first sent to the Debuncher which is a synchrotron with three straight sections giving it a roughly triangular shape. The Debuncher rotates the narrow temporal group in phase space to a narrow momentum group. It also applies some stochastic cooling before injecting the bunch into the Accumulator. The Accumulator is housed in the same tunnel as the Debuncher but at a smaller radius. It applies stochastic cooling in momentum and position to the collection of antiprotons called a *stack*. Stochastic cooling is accomplished by sensing small groups of particles with anomalous momentum and applying an appropriate electromagnetic kick to the beam. After many passes the overall phase space of the beam decreases. This type of cooling is limited by the ability to detect and respond to particles at the smallest scale, ideally individual particles.

The stacking rate into the Accumulator and the total stack available for each store has continually improved. At the beginning of Run II, stacking rates were at best 7×10^{10} antiprotons/hour and a store was typically begun when the stack size was about 100×10^{10} antiprotons. Beyond an Accumulator stack of 50×10^{10} the process of transfering additional antiprotons to the Accumulator becomes significantly less efficient. A new storage ring in Run II called the Recycler salvages antiprotons from a previous store and collects antiprotons from the Accumulator roughly every hour. During the 2009 running production stacking rates of 25×10^{10} antiprotons/hour were common, and collisions often began with a stack of more than 400×10^{10} antiprotons.

3.1.6 Recycler

The Recycler is an 8 GeV storage ring that stores and applies further cooling to the antiprotons transfered from the Accumulator and salvaged from previous collider stores. It is housed in the same tunnel and above the Main Injector. It uses permanent strontium ferrite gradient magnets that serve the function of both bending dipoles and focusing quadrupoles. This permanent magnet design allowed construction to proceed quickly and efficiently and allows it to operate more reliably than the other storage rings. Beam cooling was originally accomplished with a 0.5-2 GHz longitudinal and 2-4 GHz transverse stochastic cooling system. The bunching of the beam and the high intensities in the Recycler mean that even a very high bandwidth Stochastic cooling system starts to become ineffective since it is unable to resolve individual particles. For RunIIb an electron cooling system was added to increase cooling efficiency for stack sizes above 150×10^{10} antiprotons. Electron cooling merges an intense but relatively cool beam of electrons with the antiproton bunches in one section of the Recycler. Antiprotons with momenta significantly divergent from the electron beam experience coulomb interactions that give up energy to the electrons. The Recycler at FNAL was the first in the world to employ electron cooling to a “high energy” relativistic beam.

3.1.7 Tevatron

The Tevatron is a 2 km diameter synchrotron that provides the final stage of acceleration for the protons and antiprotons before they are focused into collision at the D0 and B0 interaction points. The ring is buried underground where the earth provides shielding from the synchrotron radiation produced during running.

During the process of shot setup the Main Injector fills the Tevatron with 36 bunches of 150 GeV protons, followed by 36 bunches of 150 GeV antiprotons circulating in the opposite direction. The two beams circulate in the same beam pipe in a helical path around each other. The 36 bunches are actually grouped into three super bunches separated by 2.64 μs *cosmic gaps*. The gaps provide time for the beam abort kicker magnets to energize when the beam needs to be dumped normally or automatically in the case of a fault (which may be abnormal beam loss, power supply failure, quench, or many other things). The 12 bunches within each superbunch are separated by 396 ns.

Once the Tevatron contains the full compliment of 36×36 bunches, the beams are accelerated to 980 GeV. The acceleration happens in eight RF cavities around the ring with a total length of about 20 m. The remainder of the circumference is made up of about 1000 superconducting magnets, 800 dipole and 200 quadrupole. The magnets are cooled to 4K using liquid helium and at 980 GeV the dipoles produce a field of 4.4 T using 4000 A of current. The short period of acceleration is followed by a few minutes of *scraping* when collimators move close to the beam and scatter away the *beam halo*, particles outside the standard beam profile. Finally, at the two interaction points the low-β triplets made up of four quadrupole magnets focus the beams to an interaction region ≈ 100 μm in diameter and 10s of cm long.

Particles in a store typically collide for 16 hours or more. The luminosity tapers off during the store, dropping quickly at first (for example, see Figure 3.23); but, dumping the store moving through a new shot setup typically requires at least two hours. During this non-colliding period the antiproton bunches are decelerated, returned to the Recycler, and cooled; the magnet currents will be ramped up for testing without beam called a *dry squeeze*; the magnets then need to be brought down to very low currents to remove residual fields before the injection of protons and antiprotons begins again. The length of the store is optimized taking into account this required downtime, the rate of luminosity decay, and the functioning of the downstream accelerators. Probably the single most important factor is the size of the antiproton stash being prepared, since this requires good functioning for an extended period of time of nearly every component mention in this section except the Tevatron.

3.2 DØ Detector

The DØ detector is designed to be a general purpose instrument for measuring high p_T phenomena from colliding beams [24]. To this end it aims to measure the full kinematics–origin, direction, and momentum– of many of the particles produced by the collider, including quarks, gluons, photons, electrons, muons, and tau, with high efficiency when their transverse momentum is greater than a few GeV. The detector has many layers of different technologies that, working together, identify and measure these particles. These sub-detectors are designed to surround the interaction point as hermetically as possible, covering as much of the 4π steradians away from small scattering angles as feasible.

The inner most sub-detector is a silicon microstrip tracker. This is surrounded by a fiber tracker and a solenoid. All these together form the tracking system which identifies the origin, direction, and momentum of charged particles. Just outside the solenoid but before the calorimeter there are preshower detectors and, close to the beam pipe, the luminosity monitor. Surrounding all this is a sampling calorimeter

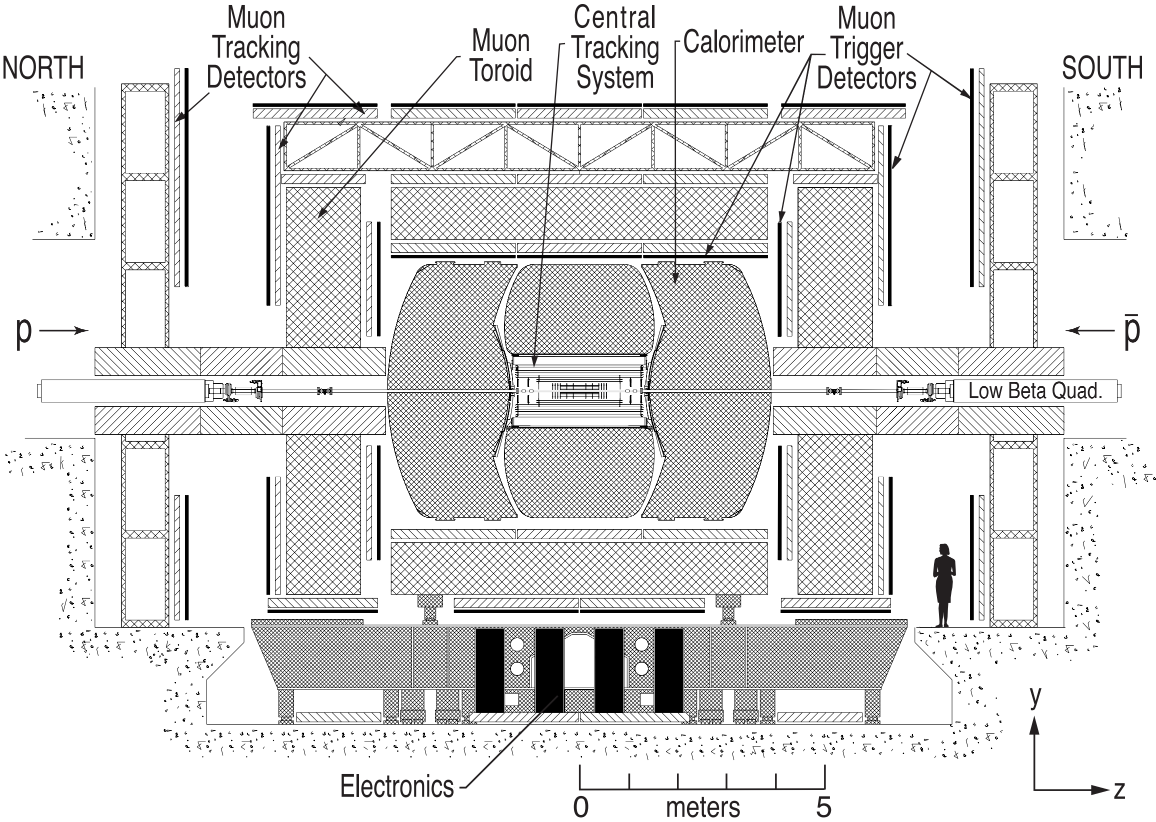

Figure 3.6: Cross section of the DØ detector in the yz-plane seen from inside the Tevatron ring. The x-axis is into the page, the y-axis is up, and the z-axis is along the beamline the the right. From the interaction point in the center outward there is the central tracking system, the calorimeter (see here as four "pillowy" regions surrounding the tracking system), the A-layer muon detectors, the toroidal magnets, and finally the B- and C-layer muon detectors.

that employs liquid argon as the active medium and uranium, copper, and stainless steel as absorber. Surrounding the calorimeter is additional tracking detectors and a toroidal magnet for identifying and augmenting the measurement of high p_T muons. The muon tracking is made up of scintillating counters and two different types of drift tubes. A cross section of the detector is shown in Figure 3.6.

3.2.1 Coordinate System

The DØ coordinate system orients the z-axis in the direction of proton circulation in the Tevatron (clockwise as seen from above). The y-axis is oriented up, and the x-axis points away from the center of the Tevatron. From this the typical cylindrical and spherical coordinate systems are defined,

$$r^2 = x^2 + y^2 \tag{3.1}$$

$$\phi = \arctan(y/x) \tag{3.2}$$

$$\theta = \arctan(z/r) \tag{3.3}$$

I will often refer to "transverse" quantities such as the transverse momentum, p_T. Unless otherwise specified, transverse is with respect to the beam line, in other words the component in the xy-plane.

In addition, we define an important alternative to θ, the pseudorapidity η. Pseudorapidity is a massless approximation to the rapidity,

$$y = \frac{1}{2} \ln \left(\frac{E + p_z}{E - p_z} \right). \tag{3.4}$$

This rapidity, y, has the property that the distance between two particles in η is invariant under a Lorentz boost in the z-direction. If we assume the mass is negligible, $m/|\mathbf{p}| \ll 1$, then

$$y \approx \frac{1}{2} \ln \left(\frac{|\mathbf{p}| + p_z}{|\mathbf{p}| - p_z} \right) \equiv \eta \tag{3.5}$$

Noting that $p_z/|\mathbf{p}| = \cos(\theta)$ and $\tan(\theta/2) = (1 - \cos(\theta))/\sin(\theta)$ yields the useful alternative form

$$\eta = -\ln \left(\tan \left(\frac{\theta}{2} \right) \right) \tag{3.6}$$

From Equation 3.6 we can clearly see that η is an entirely geometric quantity, only dependent on θ. It has the value 0 perpendicular beamline ($\theta = 90°$) and takes unbounded positive or negative values for directions approaching the beamline ($\theta = 0, 180°$). Particles of mass m and center of mass energy $\sqrt{s}$ will be produced uniformly with

$$-\ln\left(\frac{\sqrt{s}}{m}\right) < y < \ln\left(\frac{\sqrt{s}}{m}\right) \tag{3.7}$$

and so particles of small mass are produced relatively uniformly in η. Probably the most motivating feature of pseudorapidity is that the light, and relatively collinear products from the fragmentation of an energetic particle will naturally stay within a circular region in $\eta - \phi$ coordinates that is independent of η or ϕ. For this reason we define the quantity ΔR, where

$$\Delta R = \sqrt{(\eta - \eta_0)^2 + (\phi - \phi_0)^2}, \tag{3.8}$$

and given a particular η_0, ϕ_0 direction will often speak of the $\Delta R < x$ cone around it.

Directions close to the beam line, where $|\eta|$ is large, get the general label "forward." Directions perpendicular to the beam line where $|\eta|$ is small are "central". Though the division between central and forward varies by context, for the DØ detector components it is very roughly $|\eta| \approx 1$ or $\theta \approx 40°$.

3.2.2 Luminosity Monitor

The luminosity monitors (LMs) measures the average number of inelastic collisions per beam crossing to determine the instantaneous luminosity of the colliding beam. Weekly and complete Run II integrated luminosities are shown in Figure 3.7. The LM is made up of two wheels of 24 plastic scintillating counters located around the beam pipe at $z = \pm 140$ cm. They are just in front of the calorimeter and cover the pseudorapidity range $2.7 < |\eta| < 4.4$ The light from the scintillating wedges is read out using photomultiplier tubes (PMTs) attached perpendicularly, parallel to the z-axis. Since the solenoid field is still quite strong here, about 1 T, the PMTs are a type designed to operate in a strong axial field, though still the field reduces their gain by a factor of 30.

Figure 3.7: Luminosity delivered by the Tevatron over the entire Run II. As of 9 November 2010 9.68 fb^{-1} was delivered to DØ and 8.64 fb^{-1} was recorded. Recording efficiencies are currently just above 90%. See [1] which is updated regularly.

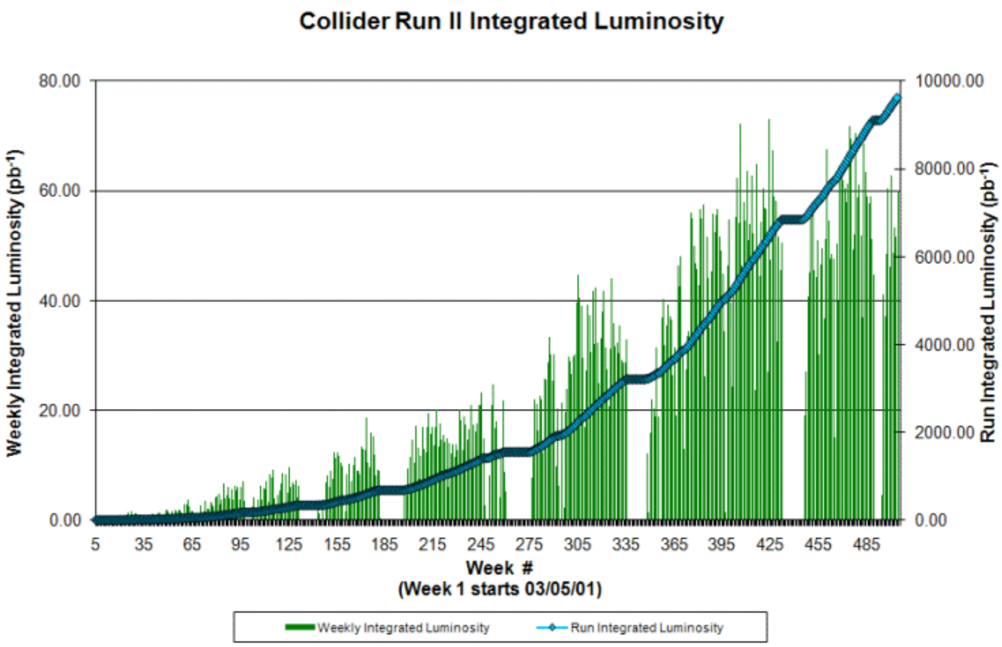

The LM counters use time-of-flight to quickly determine the rough position of the primary z-vertex. This determination is important for the luminosity measurement because it is used to filter out signal from the beam halo which would register as $|z| \approx 140$ cm. The LM uses only events with $|z| < 100$ cm. For each crossing the LM determines whether an interaction was observed or not, and then using Poisson statistics with many crossings determines $\tilde{N}_{\text{LM}}$, the average number of interactions per crossing, which is typically greater than 1. The luminosity is then

$$\mathcal{L} = \frac{f\,\tilde{N}_{\text{LM}}}{\sigma_{\text{LM}}} \tag{3.9}$$

where $f = 2.53$ MHz is the beam crossing frequency and σ_{LM} is the effective cross section of the LM, taking into account acceptance and efficiency.

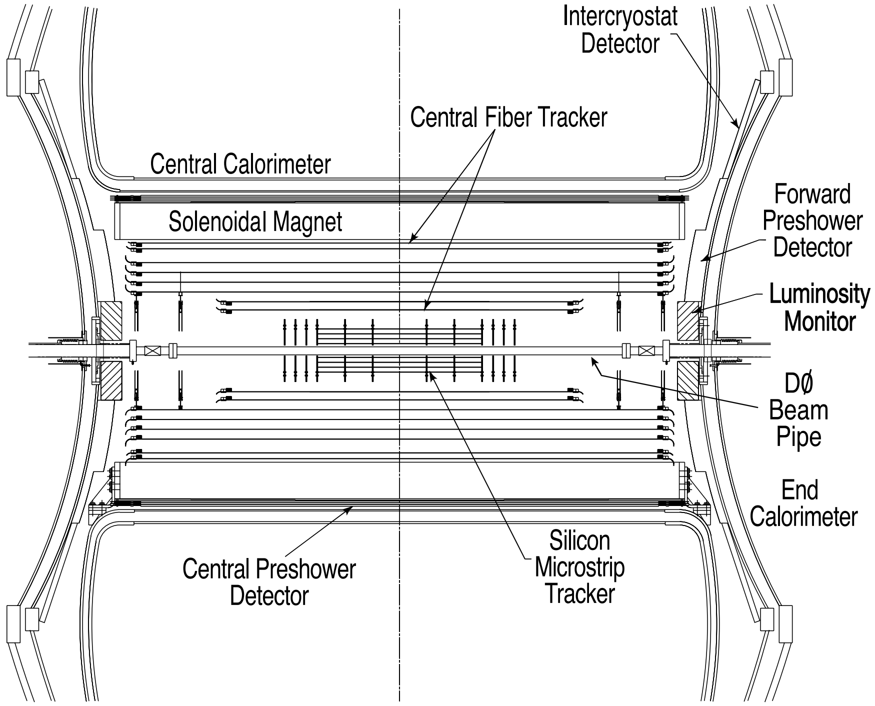

Figure 3.8: Cross section of the central tracking system, essentially zooming in on the center of Figure 3.6. From the interaction point in the center outward there is the silicon microstrip tracker, the fiber tracker, the solenoid magnet, and finally the preshower detectors just inside the calorimeter, Also shown is the luminosity monitor.

3.2.3 Central Tracking System

The central tracking system is made up of a silicon microstrip tracker (SMT), a central fiber tracker (CFT), and a solenoid. The whole system, which is shown in cross section in Figure 3.8, is about 1 m in diameter and 2.7 m long. The SMT and CFT work together to track charged particles through the magnetic field of the solenoid to determine their origin or vertex, direction, and momentum. The SMT, which lies very close the beam pipe, allows precise vertex finding for tasks such as b-quark jet tagging. The surrounding CFT improves high p_T momentum resolution. The transverse momentum resolution for tracks is about 2, 4, and 15% for tracks of $p_T = 1, 10,$ and 100 GeV, respectively, in the central region $|\eta| < 1.6$. In the forward region the solenoid provides less bending and there is no CFT coverage so resolutions worsen to around 10, 30, and 100% for the same p_Ts at $|\eta| = 3.0$.

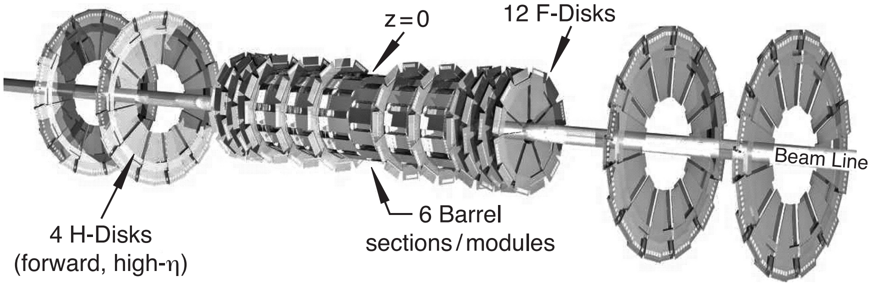

Figure 3.9: The Silicon Microstrip Tracker showing the outer layer of the barrel layers, the F-disks and the H-disks.

3.2.3.1 Silicon Microstrip Tracker

The SMT is the detector element closest to the interaction region, it provides tracking and vertex finding for tracks out to $|\eta| \approx 3$. Interactions happen with mean deviation of 25 cm in the z-direction from the interaction point (IP), and the SMT is designed to cover this region as fully as possible. Its geometry is that of barrels capped with disks (see Figure 3.9). There are six barrel segments capped by an F-disk. Each barrel segment has four layers. There are three additional F-disks at the ends of the outer segment. These components fill the region $|z| < 53$ cm and $|r| < 10$ cm. Additionally, there are two larger disks with 26 cm radius at $|z| = 100$ and 121 cm known as H-disks.

The barrel layers are made up of overlapping flat panels laid out roughly cylindrically, each panel is called a "ladder". The inner two layers have 12 ladders and the outer two layers have 24 ladders. The F-disks are made up of 12 double-sided wedge-shaped detectors. The H-disks each have 24 wedge detectors, each one formed from a single sided detector glued back-to-back. There is a total of 912 readout modules and 792,576 channels.

Silicon trackers use reverse biased diodes that emit a pulse when a charged particle passes through their depletion zone. The depletion zone is created at the interface between p and n-type silicon where electron and hole recombination leaves a region with an empty conduction band. The depletion zone is surrounded by static charged

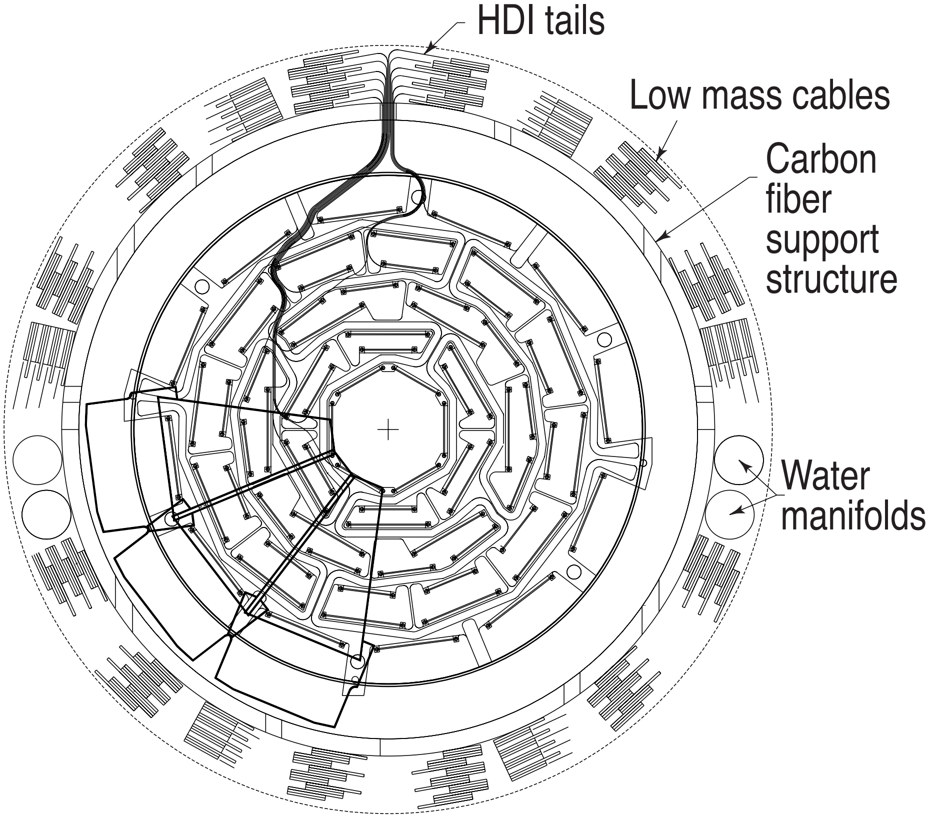

Figure 3.10: Cross section looking down the beam pipe showing the ladders of the silicon microstrip tracker barrels.

ions that create an electric field. An applied reverse bias voltage increases this electric field but little current can flow through the depleted region as long as the reverse bias is less than the breakdown voltage. When a charged particle passes through the depletion zone it liberates electron-hole pairs which are pulled via the electric field to the conduction regions at each end. This produces a charge pulse that is stored by an attached capacitor and read out by further electronics.

The barrel layers with axial strips essentially provide only a $r-\phi$ measurement of tracks, though two of the layers have double-sided boards with axial strips on the p-side and a 2°stereo angle offset of the implants on the n-type side. The disks align their strips parallel to one side (in the radial direction) of the wedges and the overlap with other wedges yields a stereo angle offset of 30°for the F-disks and 15°for the H-disks. This substantial stereo angle means that hits can be reconstructed in three dimensions in the forward region.

The pitch between diodes varies depending on the type of ladder, but around 50 μm is typical. In combination with the CFT the overall alignment has been measured with track residuals to be better than 10 μm. To prevent bulk damage the silicon must be cooled with a -10 °C mixture of water and ethylene glycol that flows through the beryllium support structure. To protect the system from from condensation it is ventilated with dry air with a dew point of -40 °C.

Radiation damage is a major factor for the silicon tracking system because it operates so close to the interaction region. There are two major effects, bulk and surface damage. In surface damage charge is trapped in the insulating layer allowing increased leakage current and the possibility of high-voltage breakdown. Bulk damage occurs as atoms in the n-type bulk are knocked out of the lattice effectively shifting it toward p-type doping. At around 2 fb^{-1} delivered luminosity layers 1 and 2 passed the point of type-inversion and with further radiation the voltage required to fully deplete the junctions increases. Currently, after 9 fb^{-1} of exposure (see Figure 3.7

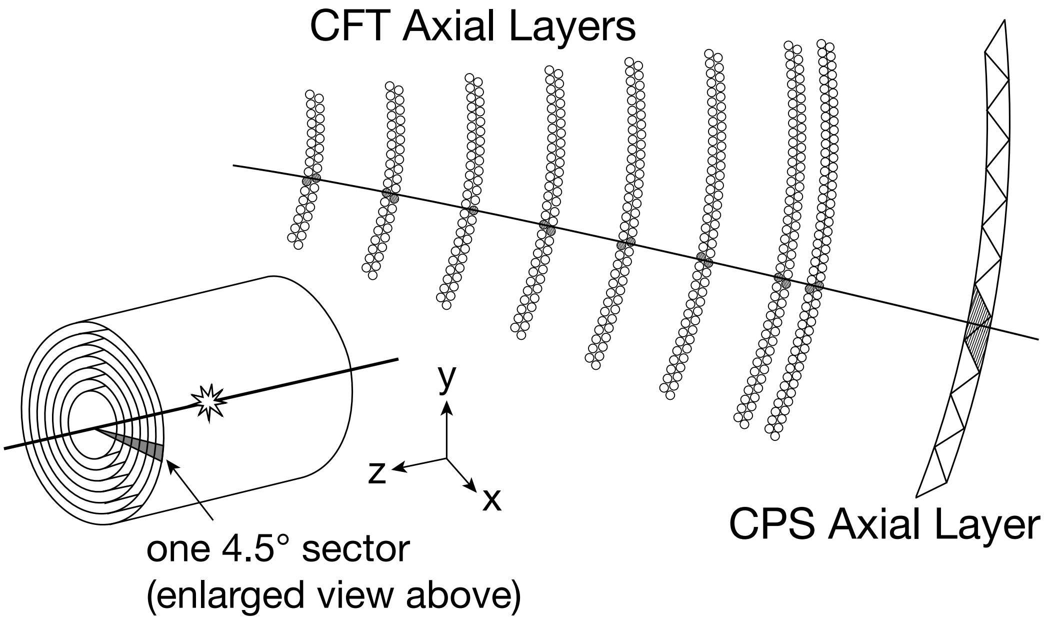

Figure 3.11: Track in the central fiber tracker.

for luminosity over time) the inner layer 1 is reaching the point were even at the bias voltage limit the silicon cannot be fully depleted. The Layer 0 was added during a later shutdown and still hasn't reach type-inversion. [25, 26]

3.2.3.2 Central Fiber Tracker

The CFT is a set of scintillating fibers laid out in eight cylinders from $r = 20$ to 52 cm. Because of the SMT H-disks, the two inner cylinders are only 1.66 m long while the remaining cylinders are 2.52 m long. Each of the cylinders supports two doublet layers of fibers; the fibers in the first doublet are oriented along the beam line (z-)axis, and the second doublet is oriented at a stereo angle in ϕ of $\pm 3°$. The "stereo" layer of the inner cylinder is at $+3°$and the stereo layers alternate moving outward.

The scintillating fibers are primarily made of polystyrene but incorporate two dyes. Excitations in the polystyrene are transfered to the 1% concentration of paraterphenyl which rapidly fluoresces at 340 nm but this wavelength has a mean free path of only a few microns in polystyrene. Trace amounts of 2-hydroxyflavone, a wave-shifting dye, convert the light to 530 nm which is not absorbed.

The scintillating fibers have a diameter of 835 μm and are connected to visible light photon counters (VLPCs) via clear fiber waveguides. The waveguides are similar to the scintillating fibers, except for a lack of florescent dye, and stretch from 7.8 to 11.9 m. The CFT required about 1000 km of fiber. The inherent doublet layer resolution is approximately 100 μm, and the locations of the layers have been surveyed with an X-ray source to an accuracy of 25 μm.

The VLPCs are impurity-band silicon avalanche photodetectors mounted in cassettes below the detector. They require cryogenics to operate effectively and the cold end of the VLPC cassettes are kept at 9 ± 0.1 K with liquid nitrogen and liquid helium cooling. An increase in temperature of only 1 K leads to a four fold increase in noise. Attached to the VLPC cassettes are analog front end (AFE) boards that perform amplification, Level 1 and 2 trigger functions, and readout for the Level 3 trigger.

3.2.3.3 Solenoid

The solenoid provides a 2 T magnetic field oriented parallel to the beam pipe. It is 2.7 m long and fills the space between 1 and 1.4 m in diameter. This field gives charged particles a spiral path whose radius is inversely proportional to the transverse momentum. The solenoid is is wound with two layers of superconductor, and each conductor has 18 strands. The conductors are a Rutherford-type cable with Cu:NbTi strands in a pure aluminum stabilizer. The operating current is 4749 A. Cooling of the superconductors is accomplished with liquid helium; a few outer components such as a radiation shield and the cold mass supports are cooled by liquid nitrogen. The fields of the solenoid and the toroid are alternately reversed every few weeks during a break in data taking.

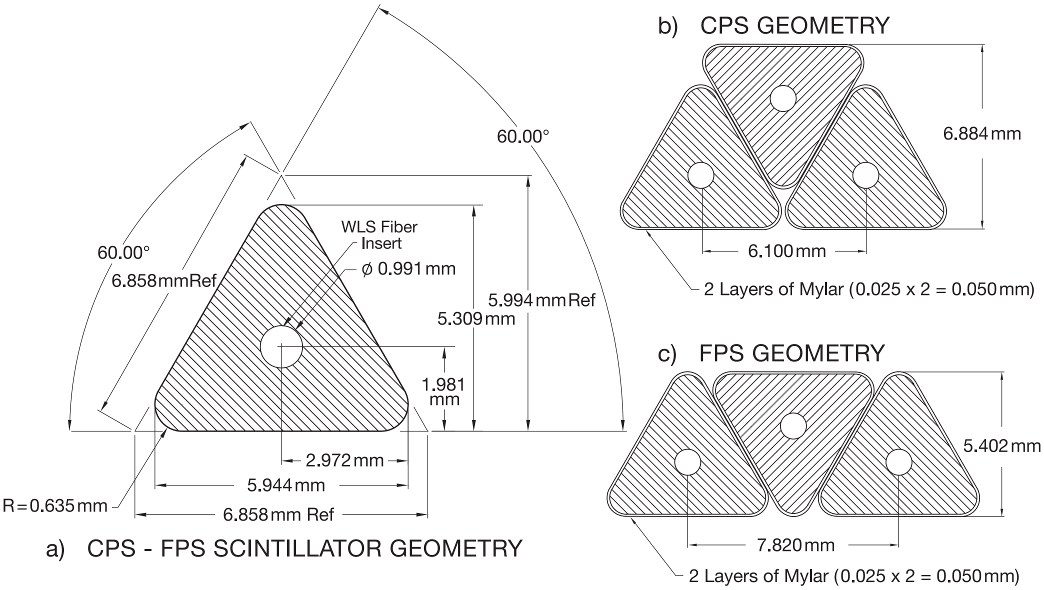

Figure 3.12: Triangular cross section of a preshower scintillator showing the central wave shifting fiber. (b) layout of a CPS layer. (c) layout of a FPS layer.

3.2.4 Preshower Detector

The preshower detectors serve as a bridge between the inner tracking detectors and the calorimeter. They improve matching between inner tracks and calorimetry cells, and they improve the calorimetry measurement by sampling showers that begin in the solenoid or earlier (mostly EM showers). They are also fast enough that they can be used in the Level 1 trigger. The preshower detectors are located on the inner surface of the calorimeter; the central preshower (CPS) surrounds the solenoid and the forward preshower (FPS) is located radially above LM.

The preshower detectors are all made up of triangular extrusions of scintillator as shown in Figure 3.12. The strips are each wrapped in aluminized Mylar and epoxied together into layers. Embedded in the center of each scintillator is a wavelength shifting (WLS) fiber that gathers photons and transports them to clear waveguides carrying 16 channels each to VLPC cassettes and readout electronics identical to that for the CFT.

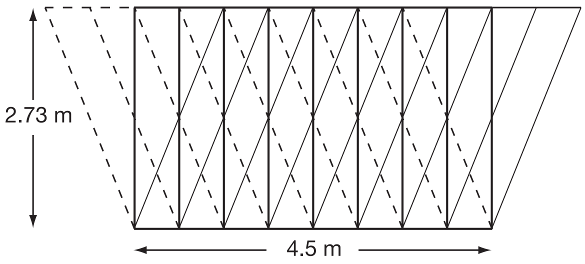

Figure 3.13: The CPS is formed from three layers, one at 24°and the other at -23.8°to the first. This figure shows the octant modules "rolled-out" with the axial direction (z-direction) oriented vertically.

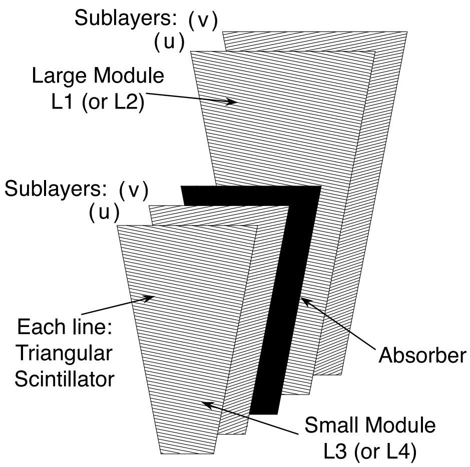

Figure 3.14: A ϕ-sector of the FPS showing two pairs of u and v slanted layers separated by absorber.

3.2.4.1 Central Preshower

The CPS is formed from three cylindrical layers with the inner layer of strips oriented axially. The second layer is oriented at stereo angle 23.774°relative to the first layer, and the third layer is oriented at the opposite stereo angle of 24.016°, as shown in Figure 3.13. The strips are split in the middle and read out from both ends. There is a total of $2(\text{split}) \cdot 1280(\text{strips/layer}) \cdot 3(\text{layers}) = 7680$ channels in the CPS. Between the solenoid and CPS is a stainless steel clad lead sheet of about 1 radiation length in thickness (7/32 in).

3.2.4.2 Forward Preshower

The FPS is made up of two layers of each made up of two (u and v) sublayers of strips as seen in Figure 3.14. The layers are separated by a lead and stainless steel absorber 11 mm thick, which corresponds to about $2X_0$. The inner layer is referred to as the minimum ionizing particle (MIP) layer and the outer layer as the shower layer.

Typically electrons will produce a very localized signal in the MIP layer but begin showering in the absorber producing a broader signal (3 layers wide) in the shower layer. Photons may not register in the MIP layer but produce a similar signal in the shower layer. The MIP layer and absorber only cover $1.65 < |\eta| < 2.5$ but the shower layer extends further in the radial direction to cover $1.5 < |\eta| < 2.5$, which can The end of the solenoid contains enough material to initiate showering in the $1.5 < |\eta| < 1.65$ region.

The sublayers are segmented into octants and offset by 13 mm radially to cover the gaps in ϕ. Strips in each octant are laid out perpendicular to one edge, using alternating edges for each sublayer. Each MIP sublayer has 208 strips and each shower sublayer has 288 strips, except in a notched region to allow for solenoid cryogenic pipes.

3.2.5 Calorimeters

The calorimeters are unchanged from the Tevatron's Run I (including a cut-out near their outer edge for the Main Ring which was replaced by the Main Injector for Run II). Details can be found in the original DØ detector paper [27]. The goal of the calorimeter is to measure the energy of jets, electrons, and photons, typically absorbing all energy out to $|\eta| \approx 4$ (from the origin) except that from muons, neutrinos, and possibly as yet undiscovered particles. There are three calorimeters, the central calorimeter (CC), end calorimeter south (ECS), and end calorimeter north (ECN).

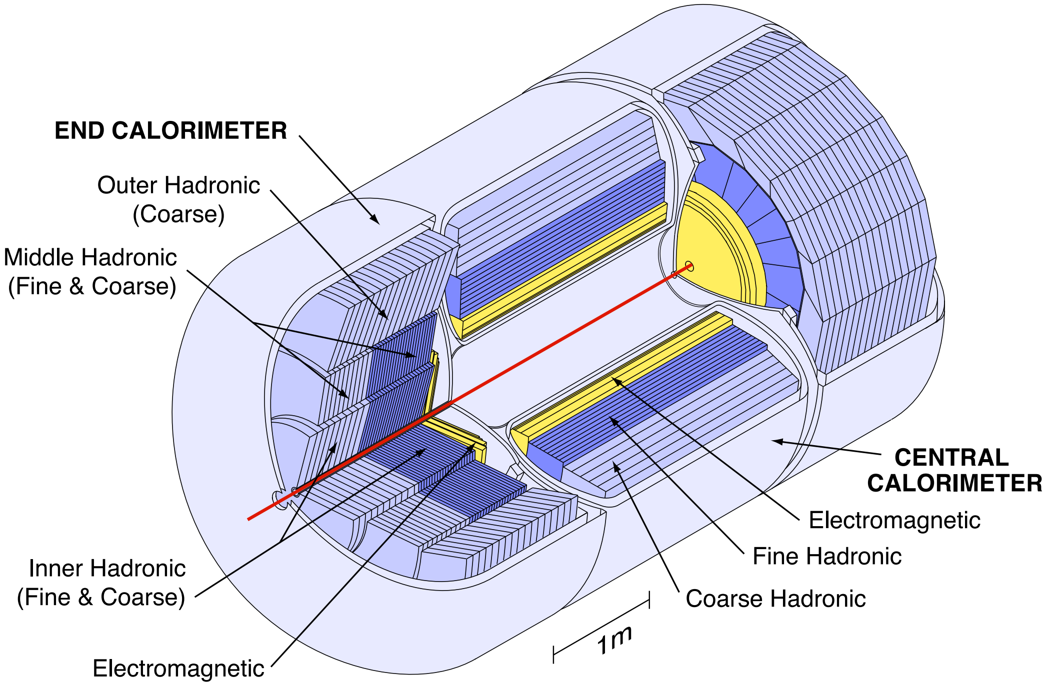

Figure 3.15: Cross section of the calorimeter showing the inner EM layers, the fine hadronic layers, the the course hadronic layers.

The CC covers out to $|\eta| \approx 1$ and the two end calorimeters overlap to $|\eta| \approx 0.7$. Each is a separate vessel with the ends able to move out of the way for access to the inner tracking. Each of the calorimeters has three layer groups we identify as the EM, fine hadronic, and coarse hadronic layers. Figure 3.15 shows the overall structure.

The calorimeters are broken up into cells that are arranged into projective towers pointing away from the interaction region. This can be seen in the cross-section in Figure 3.16. Each cell is made up of a layer of absorber material followed by a signal board. The 2.3 mm gap between the absorber and the signal boards is filled with liquid argon which is the active (sensing) material. Electrons produced by ionization in the liquid argon are accelerated between the grounded absorber and the +2 kV signal boards. Coaxial cables bring the signal through a port at the surface of the cold vessel to be fed into a preamplifier, signal shaping, and readout.

The signal boards are made up of sandwiched pairs of G-10 sheets with a resistive coating of carbon-loaded epoxy. An inner layer of copper between the sheets is milled

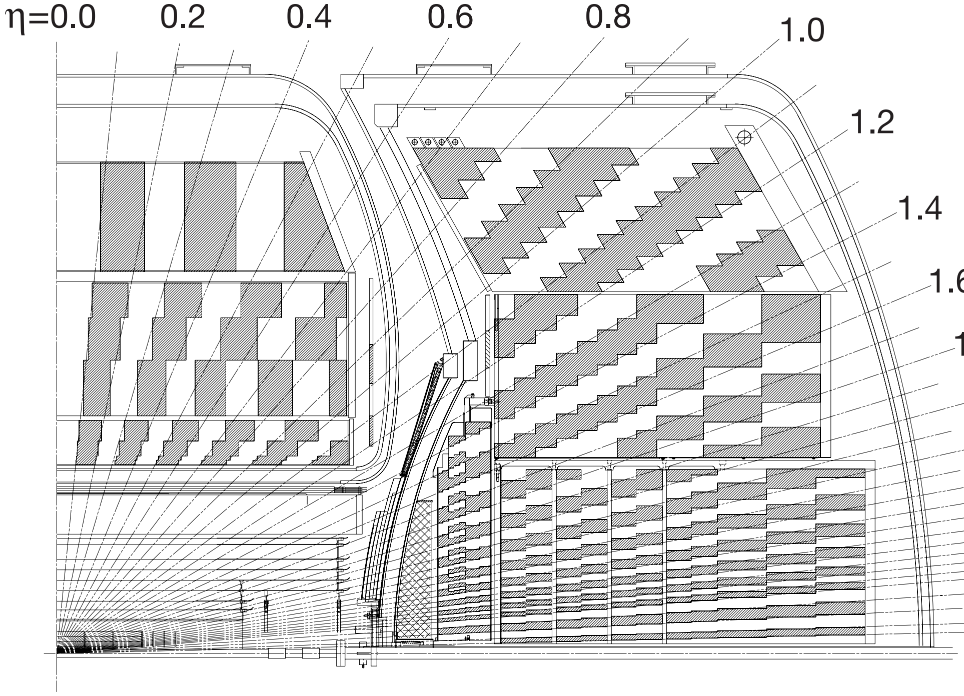

Figure 3.16: The segmentation in η of the calorimeter.

to divide the segments. The layering of absorber, LAr, and signal sheets forming a unit cell is shown in Figure 3.17. Several unit cells in the same $\eta - \phi$ direction are connected together into a single readout cell. The towers of cells running from the interaction region outward cover a $\Delta\eta = 1.0$ and $\Delta\phi = 2\pi/64$ region with a step-shaped segmentation in the $r - z$ plane as seen in Figure 3.16. One exception is in the third layer of the EM calorimeter which begins at about eight radiation lengths ($8X_0$) from the interaction region; this is where a $\approx$ 50 GeV EM shower typically peaks and so this layer has twice as many segments in the η and ϕ directions to allow more precise reconstruction of the shower direction. Another exception is in the very forward region $|\eta| > 3.2$ where the towers are wider in η so as to not become too narrow [28].

The primary difference between the three layer types is the material for the absorber. Cell size also varies from small in the inner layers (EM) to very large in the

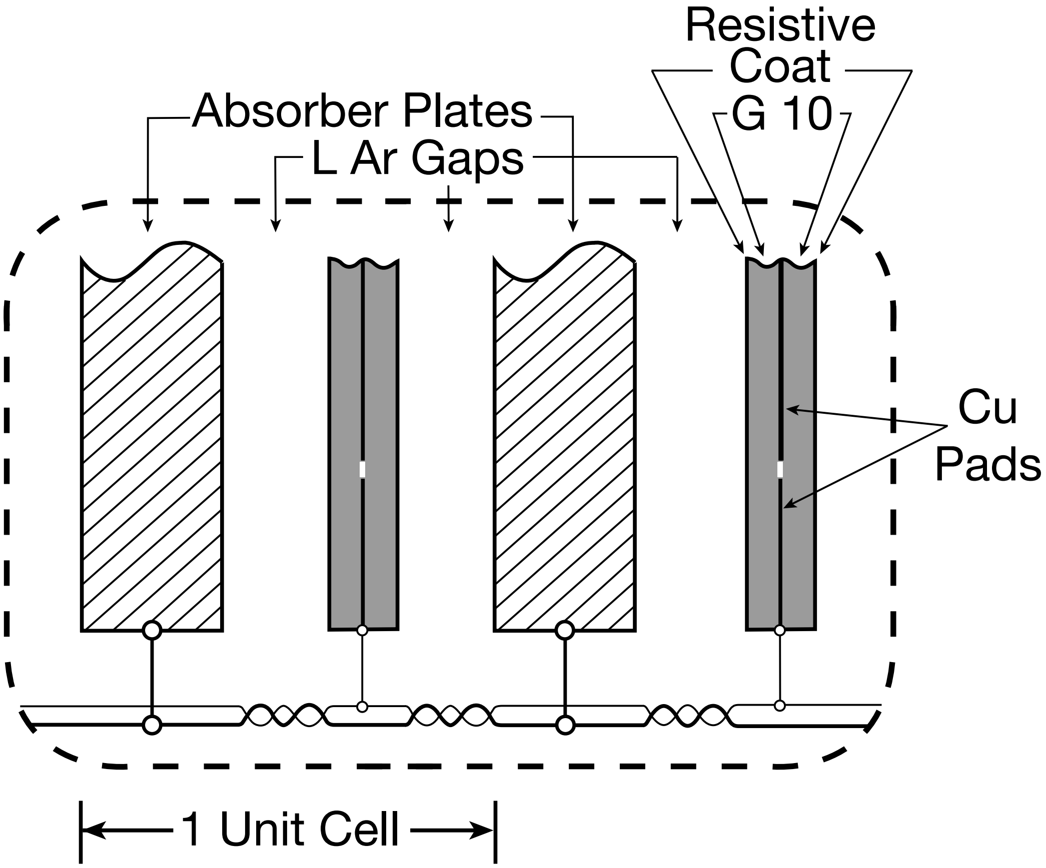

Figure 3.17: Sandwich of absorber, coated copper pads, and surrounding liquid argon active medium.

outer layers (coarse hadronic). The EM layers are closest to the interaction region and use a 3 or 4 mm thick absorber made of pure depleted uranium. The fine hadronic layers that come next use a uranium-niobium (2%) alloy in the 6 mm thick absorbers. Finally, the course hadronic layers use copper in the CC and stainless steel in the EC in 46.5 mm thick absorbers. The thin absorbers and cell size in the EM calorimeter provide a fine sampling of the beginning of shower evolution useful for differentiating electrons from pions. The thick absorbers in the course hadronic section provide higher average densities which limit the size necessary for the calorimeter. There is about $4X_0$ of material between the interaction region and the first active calorimetry cell at $\eta = 0$ ($\approx 4.4X_0$ at $\eta = 2$). The four EM layers have thicknesses of 1.4(1.6), 2.0(2.6), 6.8(7.9), and $9.8X_0(9.3X_0)$ in the CC (end calorimeter (EC)). The hadronic layers have a total thickness of about $6.0\lambda_A$ where λ_A is the nuclear absorption length. The coarse hadronic component makes up more than half of this. The CC and EC filled with argon weigh 331 and 238 metric tons, respectively.

The calorimeter has 47,032 readout channels. Signals pass through preamplifiers physically close to where they exit the cryostat. The preamplifier boards allow for calibration pulses to be injected into the signal path at their input. The preamplifier outputs are routed to baseline substraction (BLS) boards below the calorimeter that apply shaping and use switched capacitor arrays (SCAs) to store analog signals awaiting the Level 2 trigger decision. When there is a L2 accept the stored analog signal is transmitted 130 m on twisted-pair line to ADCs located outside the collision hall. Information for the L1 and L2 decisions comes from taps before the shapers that combines the signal from towers in a $\Delta\eta \times \Delta\phi = 0.2 \times 0.2$ region.

3.2.5.1 ICD and massless gap

To improve sampling of showers in the region between the CC and EC, scintillator tiles have been installed in the gap between the cryostats just above the FPS radially.

This is known as the intercryostat detector (ICD). In total it covers the region $1.1 < |\eta| < 1.4$. Each tile covers a $\Delta\eta \times \Delta\phi \approx 0.3 \times 0.4$ region and is further divided into 12 subtiles covering $\Delta\eta \times \Delta\phi \approx 0.1 \times 0.1$.

There are also special channels called the massless gaps which made up of a single sampling unit at the the innermost layer of the calorimeters. They are just inside the cryostat before the first uranium absorber, and their purpose is to sample showers that develop in the inner calorimeter wall.

3.2.6 Muon System

The muon system is made up proportional drift tubes (PDTs), mini drift tubes (MDTs), scintillation counters, and toroidal magnets. In the central region, roughly where $|\eta| \leq 1.0$, PDTs are used for tracking and momentum measurement. In the forward region, $1.0 < |\eta| < 2.0$, where particle fluxes are higher MDTs are used for tracking instead. Scintillation counters that are used primarily for triggering cover much of the same area as the wire detectors (PDT and MDT) used for tracking. Depending on location these scintillators are referred to as "cosmic cap," "cosmic bottom," "$A\phi$," and simply "trigger scintillation counters." Detectors are grouped into three layers: from interaction point outward they are the A-, B-, and C-layer. The A-layer is located inside the toroidal magnets but outside the calorimeter. The B-layer is just outside the toroid, and the C-layer is separated from the B-layer by a mostly inert gap.

3.2.6.1 Proportional Drift Tubes

The PDTs cover the central region of the muon system in A-, B-, and C-layers and can be seen in the Figure 3.18 exploded view. The A-layer is located inside the toroid magnets and the B- and C-layers outside. The PDTs are made up of extruded rectangular tubes 10.1 cm wide, oriented radially. A mixture of 84% argon,

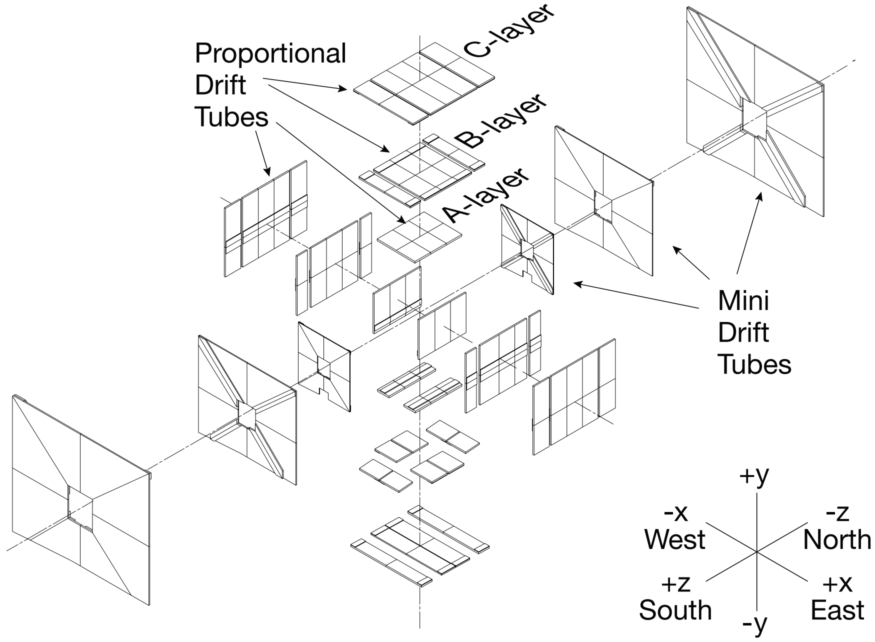

Figure 3.18: Exploded view of the muon wire detectors used for tracking. The beamline travels through the square holes in the MDT detectors along the z-axis. The PDTs cover the central region surrounding the interaction point on four sides. The toroidal magnets fill the space between the A- and B-layers.

8% methane, and 8% CF_4 fills the tubes; electrons liberated in this gas by an ionizing particle drift to an anode wire in the center. From the drift time a drift distance can be measured with a resolution of about 1 mm. The drift rate in this gas mixture is about 10 cm/μs for a maximum drift time of 500 ns. This means that for a 396 ns Tevatron bunch spacing two crossings can occur during the drift time.

Pairs of tubes are ganged together and read out from one end of each. The hit position along the wire can be determined by the propagation time of the signal which has a resolution of between 10 and 50 cm. The poorer resolution comes from dispersion a hit close to one readout has to propagate two tube-lengths to the other readout. The hit position is also determined by a vernier (tapered) cathode pad along the top and bottom of the drift tubes. This method provides a 5 mm resolution but only A-layer pads and 10% of the B- and C-layer pads are instrumented.

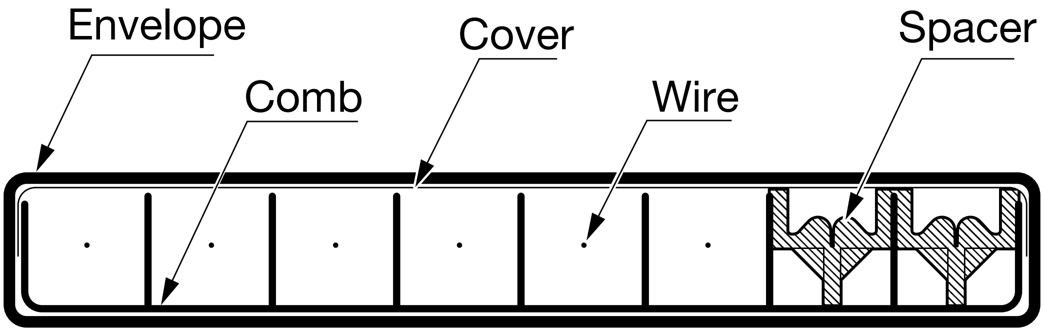

Figure 3.19: Cross section of the mini drift tubes.

3.2.6.2 Mini Drift Tubes

As the name implies, the MDTs are more finely segmented than the PDTs, for operating in the higher occupancy environment of the forward region. The tubes form eight 9.4 mm square cells as shown in Figure 3.19. The 50 μm W-Au anode wires are positioned by spacers at least every 1 m, and the tubes can be as long as 5.83 m in the outer layer. The three layers, A, B, and C have 4, 3, and 3 planes of tubes, respectively, in each layer. The tubes are aligned approximately along the magnetic field lines in a coaxial square around the beam line in ϕ octants. There are 48,640 channels.

The MDTs use a different gas, 90% CF_4 and 10% CH_4, which is non-flammable and shows no radiation aging. The operating voltage is 3200 V implemented by a negative supply on the cathode and grounding at the amplifier readout off the anode wires. Drift times are similar to the PDTs, about 12 cm/μs, but the smaller tubes leads to shorter maximum drift times of 40 ns for perpendicular tracks and 60 ns for 45°tracks (because of the square shape). A resolution of 350 μm is possible except that the coarse digitization binning in DØ yields a resolution of about 700 μm. The momentum resolution is about 20% for muon of $p < 40$ GeV. Momentum resolution of combined muon tracks is dominated by the central tracking resolution up to about $p < 100$ GeV and $|\eta| < 1.6$, beyond which the forward muon system becomes important.

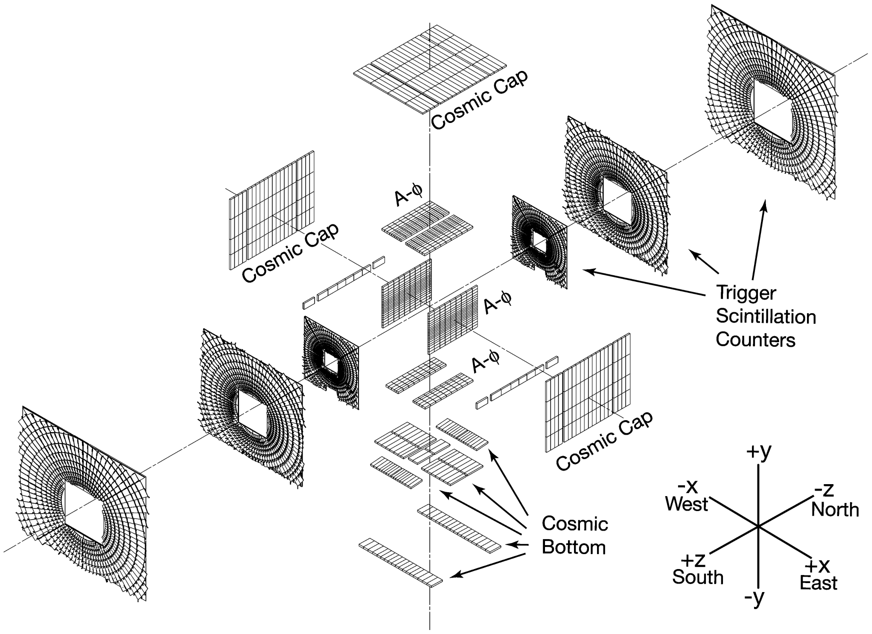

Figure 3.20: Exploded view of the scintillators used for muon triggering. The $A\phi$ and inner trigger scintillator layers lie inside the muon A-layer.

3.2.6.3 Scintillators

Scintillators counters in the muon layers provide a fast signal for triggering and a ϕ measurement in the forward region. There are three systems: the cosmic cap and cosmic bottom counters reside in the central B and C layers, the $A\phi$ scintillation counters are in the central A layer, and the forward scintillation counters cover all three forward layers; they can be seen in Figure 3.20. The $A\phi$ and forward counters are segmented in $4.5°\phi$ segments corresponding to the CFT trigger segmentation. The $A\phi$ counters are 33.25 in long in the axial direction to approximately correspond to the PDTs. The forward counters are segmented into 12 rows of $\Delta\eta = .12(.07)$, for the inner 9 (outer 3) rows. The cosmic cap and bottom counters are described more extensively in [29].

3.2.6.4 Toroidal Magnets

The toroidal magnets produce a field used to bend charged particles that escape the calorimeter, such particles are very likely muons. This bending allows for a second measurement of muon momentum which compliments the tracking measurement and makes matching more robust. The toroid is contained within a squared cylindrical volume and so the magnetic field lines travel perpendicular to the beam line in roughly a squared cylinder.

In the central region the toroid is assembled into three components. There is a bottom component and two C-shaped components, one for each side. The C-shaped components of the central toroid move away from the beam line to allow easier access to the A-layer muon, calorimetry, and tracking detectors inside.

3.3 Trigger Overview

The Tevatron brings bunches of protons and antiprotons together in collision inside the DØ detector at a rate of 1.7 MHz. The task of the trigger and data acquisition framework is to identify the crossings that yield the most interesting interactions, digitize the measurement, and store the event for offline analysis. The budget for stored events is an average rate of 100 Hz, which is limited by offline reconstruction and reprocessing rates, so the trigger system must ultimately select, on average, only 1 event from every 17000 crossings.

Trigger decisions are made in three stages, known as Level 1, 2, and 3, or L1, L2, and L3. An outline of the data flow is shown in Figure 3.21. The L1 trigger is implemented in hardware including field programmable gate arrays (FPGAs) and is designed to select events at a maximum rate of 2.5 kHz. The L2 trigger is implemented in firmware as well as software running on CPUs. Events are selected by the L2 trigger at a rate of 1 kHz at which point the entirety of the detector data is read out and shipped to a L3 processor. The L3 processors are computers running a simplified and optimized version of the full reconstruction that will be applied later offline. The L3 processors, using the results of their full reconstruction of objects such as electrons, muons, photons, and jets, make a final decision whether to store an event. Events

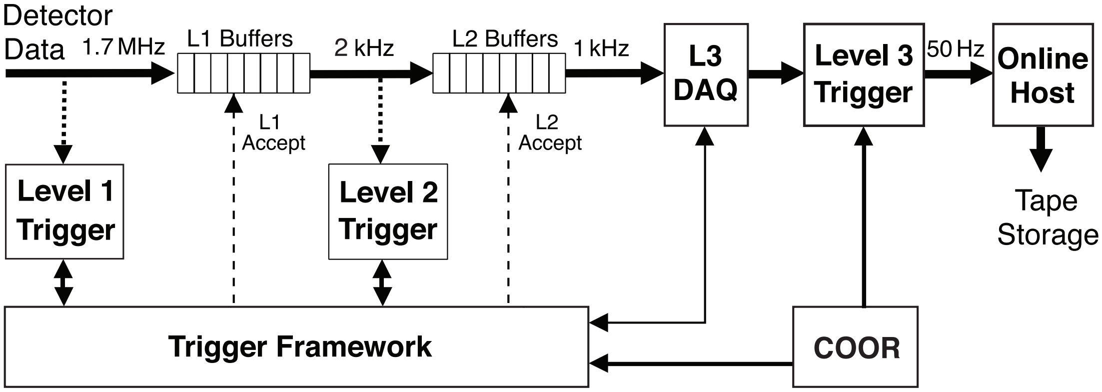

Figure 3.21: The process of selecting which events to record happens in three stages, the level-1, -2, and -3 triggers. The numbers here are slightly outdated, the current systems allow for triggers with a maximum rate of 2.5 kHz, 1 kHz, and 200 Hz, respectively. The overall average event selection rate is about 100 Hz.

are selected at a rate averaging 100 Hz, but at the beginning of a store when the instantaneous luminosity is high the rate may reach 250 Hz.

3.3.1 Level 1 Trigger

The L1 trigger is made up of five systems; the L1CAL, L1CTT, L1MUO, and L1FPD communicate with the trigger framework (TFW) where the L1 decision is made. They can be seen in the middle column of Figure 3.22.

Buffers can store up to 32 beam crossings before the L1 decision which may take up to 4.2 μs. The TFW can be programmed with 128 physics events for triggering from 256 “AND-OR” terms. Each physics trigger is associated with a beam condition requirement that must also be met for triggering.

Triggers that would otherwise lead to unmanageably high accept rates can be masked a fraction of the time via a *prescale*. Each prescale is described by an integer, say n, such that only one out of n lead to an accept. As the luminosity of the beam decreases throughout a store the prescales are occasionally adjusted downward and new triggers are turned on. The goal is accept as many interesting physics events within the L1, L2, and L3 bandwidth limits. The target for maximum L1 accepts is

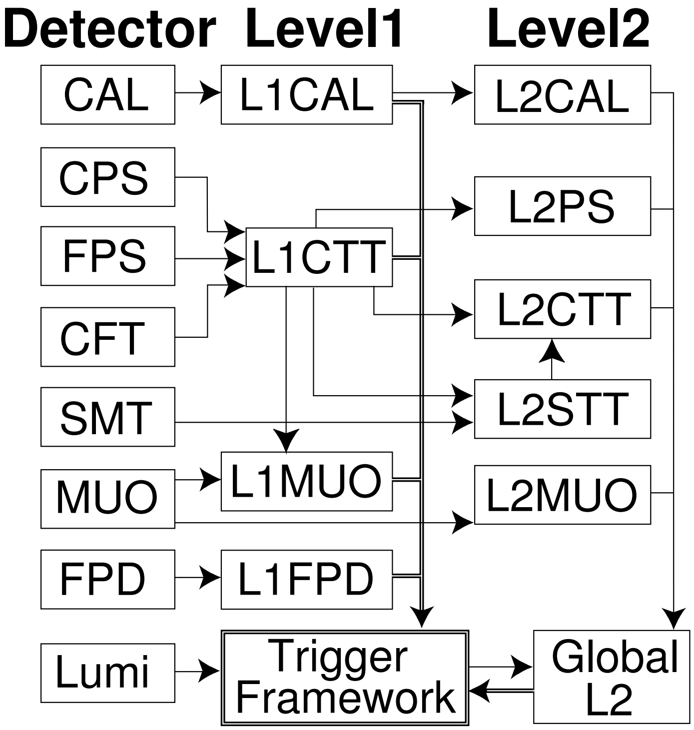

Figure 3.22: Connections between the L1 and L2 trigger components, all organized by the trigger framework.

about 1800 Hz which is the upper horizontal line in Figure 3.23. In this figure the L1 accept rate is the upper (black) curve, and the numbered points indicate where datataking was restarted with a new prescale set.

3.3.2 Level 2 Trigger

After the L1 decision the accepted event data is shifted to buffers for the L2 triggers which have 100 μs to make a decision. The L2 decision is formed from the results of five L2 processors, L2CAL, L2PS, L2STT, L2CTT, and L2MUO, that feed into the L2Global processor. The L2Global can make its decision based on combinations of objects reconstructed by the other crates; so, for example, an electron-like object can be required by matching a track with a cluster in the EM calorimeter. The L2 system also has time for more involved processing of tracks. For example the L2STT system takes hits found in the CFT at L1 and uses these to form a *road* in which matching

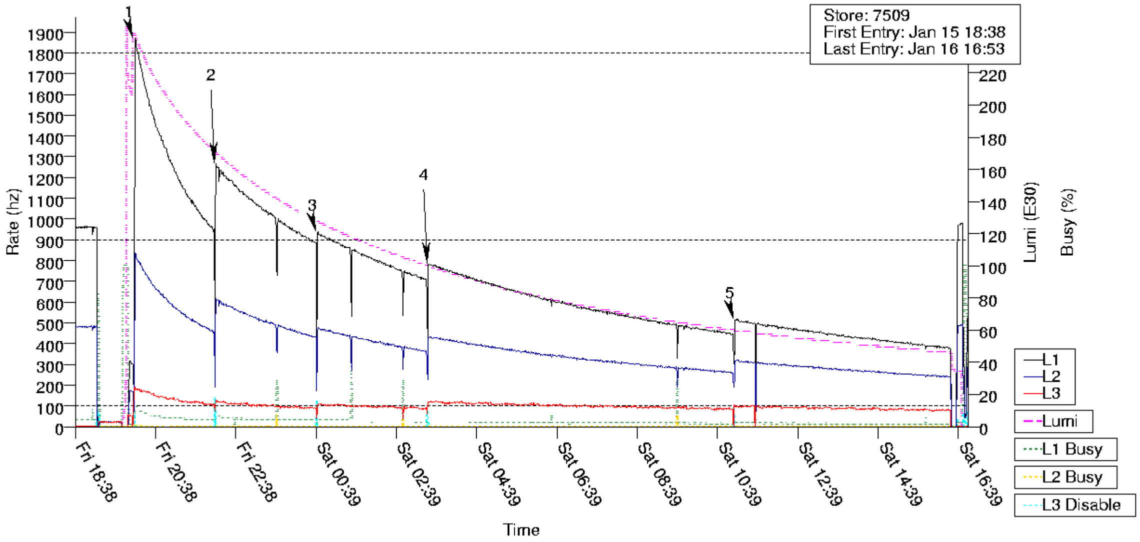

Figure 3.23: Example of luminosity and trigger rates over the course of one Tevatron store. The luminosity delivered to DØ is in magenta. Here the luminosity starts at $245 \times 10^{30}\mathrm{cm}^{-2}\mathrm{s}^{-1}$ and after colliding for almost 21 hours has decreased to $47 \times 10^{30}\mathrm{cm}^{-2}\mathrm{s}^{-1}$. Level 1, 2, and 3 trigger rates are rendered in black, blue, and red, respectively. The numbers indicate the start of new runs; which is typically done to change the trigger prescales as the luminosity decreases.

SMT tracks are hopefully found, as seen in Figure 3.24. This process uses only hits in the inner and outer layers of the CFT but is later sent to the L2CTT processor where it is matching to full CFT tracks.

The L2 decision comes from the OR of the scripts associated with each of the L1 triggers that fired. Buffers hold up to 16 events accepted at L1 before they must be accepted or rejected by the L2 decision. If an L2 decision is delayed or other *busy* condition occurs the L1 buffers may also fill up, leading to an front end busy (FEB). In a FEB condition events that should otherwise be recorded are lost. Typically the DØ data acquisition (DAQ) runs with a total FEB of a few percent, but at high luminosities the FEB can go above 10%, primarily because of the multiplicity of tracks.

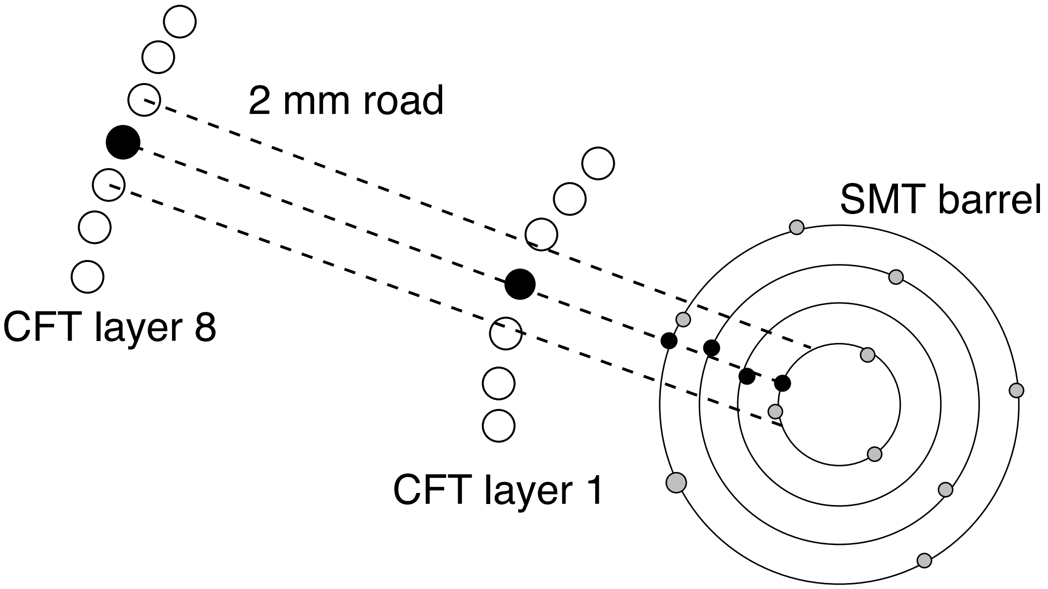

Figure 3.24: SMT and CFT road

3.3.3 Level 3 Trigger

The L3 decision involves an simplified version of the full reconstruction and processing occurs on a farm of commodity CPU nodes. At L3 the entirety of the analog calorimeter data is finally digitized and all data from an event is brought to one place for processing. The relationship of physics objects can be tested more fully for such things as isolation and combined kinematic quantities such as $\not\!\!E_T$. The primary vertex is used to refine the transverse energy measurement for EM and hadronic jets. In addition, hot cells can be masked, timing from the muon triggers is used to eliminate out-of-time cosmic tracks, and more advance tracking algorithms identify such things as displaced vertices from *b*-quark processes.

When an event is selected at L2 each readout crate shifts data to a queue on an single board computer (SBC). The TFW informs the routing master that an event has been selected and it selects a L3 node for the event. All the SBCs then receive a tag with this information, which is added to second queue. The SBCs match tags and event data in their queues and send the data off to the appropriate farm node. The farm nodes waits for data all SBCs and then must unpack it, build physics objects, and sent the results to data loggers if the event is accepted. On the current hardware the processing takes about 50 ms. Hundreds of nodes are used and processing at L3 is rarely, if ever, a bottleneck.

CHAPTER 4

Offline Particle Identification and Reconstruction

High energy collisions produce many different particles, some decay in very short distances and can only be reconstructed from decay products (such as Zs or taus), others penetrate material to various depths before stopping (such as electrons, photons, or hadrons) and others can penetrate far more material than can be practically instrumented (such as muons or neutrinos). For a general purpose detector such as DØ there are two tasks that must be accomplished during event processing: identifying the types of particles and measuring their kinematic properties (energy and direction). This process is called reconstruction and it happens at many levels from very coarse estimates involving simple patterns of tracks and calorimeter energies for the L1 trigger to the global track fit and energy loss compensation for the final muon reconstruction. Along the way identification and measurement are closely interwoven; for example, the calibration for a cluster of energy in the calorimeter may be different if it is from an electron or a hadronic jet.

4.1 Particle identification

To get general measurements of high energy particles from collisions the interaction point is surrounded by layers of tracking and calorimetery. The goal of tracking is to identifying particles with minimal interaction usually by amplifying the ionization that may happen as a charged particle passes. The calorimetry on the other hand aims to completely stop a particle and measure it's energy. The various layers are designed such that they form the most efficient and precise sieve of these particle types that is practical.

Look to Figure 4.1 for a skematic of how particles are identified. All charged particles leave signals in the inner layers of tracking. After the tracking come two major layers of calorimetry, called EM and hadronic. The EM calorimeter is designed to measure the energy and shower shape of a typical electron or photon hitting its material. The hadronic calorimeter is much thicker, denser, and more coarsely segmented; it stops hadronic particles and what energy remains of an electron or photon. Only muons and neutrions typically escape the calorimetry Muons, though, are charged and so can be tracked with an outer tracking system dedicatd to them. Neutrinos only interact via weak processes and so are essentially not observed. (There may be other long-lived particles that behave similarly and so have so far gone undiscovered).

Hadronic pariticles generally appear in a focused grouping called a jet. The jet is the product of the fragmentation from the strong interaction when a quark or gluon is involved in a hard interaction. The overall identification goes generally in this order:

1. Large (in ΔR) clusters of energy in the hadronic calorimeter identify jets.
2. Smaller clusters of energy that are mostly (>90%) in the EM calorimeter are from either electrons or photons.
3. Electrons are identified by a track, photons by the absence of a track.
4. Muons are identified by a track in both the inner and outer tracking that is isolated from other objects.
5. Neutrinos or other undetectable particles can be inferred from an imbalance in the total transverse energy after the other objects are measured.

Figure 4.1: Skematic illustration of the process of identifying different particle types using tracking and calorimeters. Charged particles such as electrons, muons, protons, and charged pions leave tracks in the central tracking systems. Electrons and photons deposit most of their energy in the EM calorimeter, distiquished mainly by a track for electrons and none for photons. Hadronic particles penetrate further and deposit most of their energy in the hadronic calorimeter. Quarks and gluons with enough energy fragment into a jet of mostly hadronic particles. Muons and neutrinos excape the detector but because the muon is charged it is detected by the tracking system.

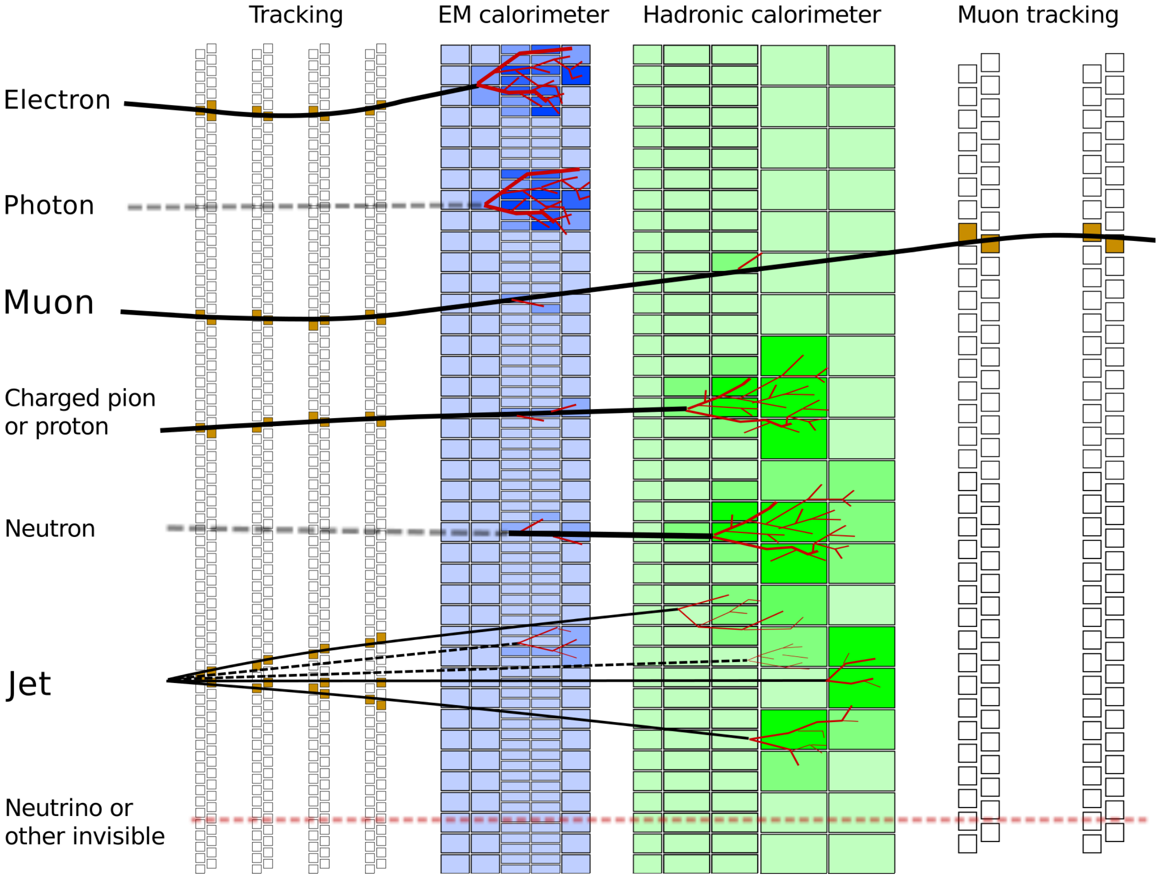

Other objects leave somewhat more ambiguous signals but are nevertheless very important such as the τ which has hadronic decays producing a unique narrow jet. Also, using information from tracking allows us to separate b-quark jets from lighter quark and gluon jets in a process called b-tagging. We will not have need for these later identification techniques in this work.

4.2 Tracks

DØ uses a combination of two algorithms to reconstruct tracks in the SMT and CFT. The first is the Histogram Track Finder (HTF) and the other is the Alternative Algorithm (AA). Both algorithms avoid the combinatorial explosion of having to compare every possible combination of hits, but they each have relative merits having to do with efficiency for low and high-p_T tracks and robustness in high luminosity environments.

In the solenoid magnetic field track follow circular paths in the plane perpendicular to the field, in this case x-y. Under the assumption that a track originates from the coordinate origin then there are two parameters that define such a track, the curvature ρ and the angle ϕ of the track at the origin. Just as these (ρ, ϕ) coordinates map into a curve in (x, y) space, one can similarly map an (x, y) coordinate into a curve in (ρ, ϕ) space which cooresponds to all the tracks that may pass through that point. This process is called a Hough transform and it is used to map a hit into what is actually a line in (ρ, ϕ). The HTF algorithm works by filling a 2D histogram of (ρ, ϕ) with values along the Hough transform line of each hit. A true track should correspond to clusters with high multiplicity in this histogram. The HTF algorithm selects groups of hits associated with histogram entries above a certain threshhold, $N_h^{\min}$, called *templates* and further filters them. The (r, z)-coordinates of hits in these templates are used form lines $(z_0, dz/dr)$ and a similar filtering is applied. The $\eta > 0$ / $\eta < 0$ ambiguity is resolved in a third step, and finally the full 3D hit information is used by a Kalman fitter to do a final filtering of the hits and determine the track parameters. The HTF algorithm is run in two ways, once starting with SMT hits and extrapolating to the CFT in the Kalman fitter stage, or the reverse, starting with CFT hits. [30, 31]

The HTF algorithm is efficient for high-p_T isolated tracks but to increase robustness in high luminosity environments and to improve efficiency for low-p_T tracks and those missing hits the AA is used. The AA begins by selecting seeds of three (r, ϕ) hits. These seeds must have their first and second hits in a $\Delta\phi$ as seen from the beamspot, and adding the third hit must produce a curvature more than that corresponding to $p_T = 180$ MeV and impact parameter less than 2.5 cm. The algorithm then propogates the track to outer layers by searching in a $\Delta\phi$ window and selecting hits that keep the increase in χ^2 below a threshold. As the tracks are propogated fitting in (r, z) is also used to filter the candidate hits. As the track crosses a new layer missing hits are allowed up to a certain threshhold. This algorithm can also be seeded with CFT hits, but because the CFT design doesn't inherently match axial and stereo angle hits further assumptions are needed to reduce the combinatoric and make the computation reasonable. This is done by first finding a primary vertex using the SMT algorithm and requiring that as the track is propagated out through the CFT the hits remain consistent with this vertex. Once a track in the CFT is found consistent hits in the SMT are added to the fitting. [32, 33]

4.3 EM objects

In the context of particle detection "EM objects" will refer to electrons and photons. Muons are identified separately because they deposit only a small fraction of their energy in the calorimeter, and taus (not used in this analysis) decay leptonically or hadronically close to the interaction region before reaching the detectors. The response in the calorimeter should be very similar for electrons and photons, developing via a cascade of Bremstralung ($e \to e\gamma$) and pair production ($\gamma \to e^+e^-$); but, only the electron should leave a track pointing toward the calorimeter cluster. The photon shower develops slightly later than an electron, but this effect is small, on average of shift of about a radiation length (actually $\frac{9}{7}X_0$).

EM objects deposit most of their energy in the early layers of the calorimeter (appropriately designated the EM calorimeter) which is designed to get a useful sampling of the developing EM shower shape before all remaining energy is collected in the hadronic calorimeter. The peak of the EM shower shifts deeper for higher energy EM objects, but for objects of a few tens of GeV (such as from $Z \to ee$) it should generally occur in the EM3 layer, the most finely segmented. This corresponds to $\approx 6X_0$ or 10 cm in DØ . Isolation requirements are also important to the identification: hadronic objects such as $\pi_0 \to \gamma\gamma$ can decay electromagnetically but these usually occur within jets and so are often surrounded by a broad cone of additional activity.

The process of identification starts by selecting clusters of energy that have high EM fraction ($E_{\text{EM}}/E_{\text{total}}$) and isolation. The clusters along with any matched tracking information is further filtered by the `ElectronSelector` and `PhotonSelector` based on shower shape, isolation, and tracking. Clusters are selected using a $\Delta R < 0.4$ cone algorithm applied to the energy in the four EM layers and the first fine hadronic (FH) layer in 0.1×0.1 segments of $\phi \times \eta$ space ($\phi \times \eta$ projective towers). The clustering starts with the highest E_T tower, combines it with additional energy in a $\Delta R < 0.4$ cone, recomputes the centroid of the cluster, and repeats in an iterative process. Remaing clusters above a $E_T > 0.5$ GeV threshhold are used to seed clusters in descending E_T order. Applying cuts on the fraction of EM calorimeter energy and isolation,

$$\text{Iso} = \frac{E_{\text{EM}}}{E_{\text{total}}} > 0.9$$

$$\text{EMfr} = \frac{E_{\text{total}}(\Delta R < 0.4) - E_{\text{EM}}(\Delta R < 0.2)}{E_{\text{EM}}(\Delta R < 0.2)} < 0.2$$

yields our *preselected* EM objects.

4.3.1 Electrons

For each preselected EM object a number of values are computed for use in the final identification. The identification of the object as an electron or a photon is accomplished with a combination of simple cuts on these variables. In the most recent iteration DØ is using four combinations of cuts for electrons called simply Point0, Point05, Point1, and Point2, from loosest to tightest. The loose cuts have high electron efficiency at the cost of lower background rejection, useful for signals with extra information but low rate such as $h \to Z \to \ell\ell\ell\ell$. The tighter cuts are useful if the rate is high but the electron identification must reject more background such as in $W \to e\nu$. In addition to the preselection variables, the cuts use

HMx7 The 7-variable H-matrix. The energy fraction in the four EM calorimeter layers along with the total EM energy, z-vertex, and ϕ width are used to compute a χ^2 measuring the consitency of the shower shape with reference electrons and the inverse of the covariance matrix for these electrons (the H-matrix). This is used in the CC.

HMx8 The 8-variable H-matrix which adds z-width for the EC.

Sigphi Cluster width^2 at EM layer 3 in ϕ.

IsoHC4 Track isolation in a "halo-cone", the sum of track p_T for tracks $0.05 < \Delta R < 0.4$ from the cluster.

NN7 Artificial neural network using 7 variables for CC: fraction of EM energy in layer 1, number EM1 cells in $\Delta R < 0.2$, IsoHC4, number of EM1 cells in

$0.2 < \Delta R < 0.4$, number of tracks in $\Delta R < 0.5$, number of CPS clusters in $\Delta R < 0.1$, and energy squared weighted RMS of CPS.

NN3 Artificial neural network using 3 variables for EC: number EM1 cells in $\Delta R < 0.2$, IsoHC4, and 8-variable H-matrix.

Lhood8 Likelihood computed as $\sum \mathrm{PDF}_e(i)/(\sum \mathrm{PDF}_e(i) + \sum \mathrm{PDF}_{\mathrm{qcd}}(i))$ for the 8 variables: spatial track match χ^2 probability, E_T/p_T, 8-variable H-matrix, EM fraction, distance of closest approach to primary vertex, number of tracks in $\Delta R < 0.05$, sum p_T of tracks in $\Delta R < 0.4$, and the number of CPS strips / E_{cal}.

E/p Calorimeter energy divided by tracker momentum

TrkMatch Track match χ^2 probability (negative if no track found).

HoR Hits on road is a measure of the number of tracking hits along the *road* pointing toward the EM cluster. This is used to identify electron candidates without a fully reconstructed track. Only useful in the central region.

The cuts applied to these variables are shown in Table 4.1. We have selected the Point05 cuts hilighted in the table for the analysis that follows.

4.3.2 Photons

Photons are selected in a similar manner to electrons. The sets of cuts are designated Core0, Core1, and Core2, from loosest to tightest. The cuts are also different in the central calorimeter and endcap calorimeter. The details of the identification cuts are given in Table 4.2. Though there are some shower shape differences the main feature that identifies a photon is the lack of a track match. Because tracking efficiency is significantly lower in the endcap region reliable photon identification in this region is difficult. As will be demonstrated, the GMSB signal of interest in this

Table 4.1: The cuts for electron identification are labeled Point0, 05, 1, and 2. Not all variables are used for all Points, and because of significant differences between central and endcap calorimeters they are treated separately. This analysis uses Point05. Some of the cuts are $|\eta|$ dependant via the functions $f_1(\eta) = 6.5(|\eta - 0.82)^{-1} - 2.8$ if $|eta| \leq 2.6$, $f_1(\eta) = 6.5(|\eta - 1.835)^{-1} - 2.8$ if $|eta| > 2.6$, $f_2(\eta) = \max(0.01, -2.5|\eta| + 7)$, and $f_3(\eta) = \max(0.01, -2|\eta| + 5)$.

Variable	Central calorimeter				Endcap calorimeter			
	Point0	Point05	Point1	Point2	Point0	Point05	Point1	Point2
Iso <	0.09	0.15	0.08	0.08	0.1	0.05	0.01	0.06
EMfr >	0.9	0.9	0.9	0.9	0.9	0.97	0.9	0.9
HMx7 <	–	–	35.0	35.0	–	–	–	–
HMx8 <	–	–	–	–	40.0	10.0	40.0	10.0
Sigphi >	–	–	–	–	$f_1(\eta)$	$f_1(\eta)$	$f_1(\eta)$	$f_1(\eta)$
IsoHC4 <	4.0	3.5	2.5	2.5	$f_2(\eta)$	$f_3(\eta)$	$f_2(\eta)$	$f_2(\eta)$
NN7 >	0.4	0.3	0.9	0.9	–	–	–	–
NN3 >	–	–	–	–	0.05	0.20	0.05	0.1
Lhood8 >	–	0.05	0.2	0.6	–	–	0.05	0.65
E/p <	–	8.0	8.0	3.0	–	–	–	6.0
TrkMatch >	0.0	0.0	0.0	0.0	–	–	0.0	0.0
HoR >	0.6	–	–	–	–	–	–	–

thesis produces high p_T photons that almost entirely end up in the CC region. For this reason we only consider photons identified in CC. Our final state has a fully reconstructed $Z \to \ell\ell$ in addition to the photon so background rejection is less of an issue and we choose the CC Core0 identification for the analysis that follows. (As you will see later, even with the looser photon identification the contribution from $Z + \text{jets} \rightsquigarrow Z + \gamma$ fakes is less than 1% in our $p_T(\gamma) > 20$ GeV signal region.)

4.4 Muons

The DØ detectors include a dedicated muons tracking system which offers an independent momentum measurement in addition to the measurement in the central tracking system. This means that a variety of muon reconstructions are possible, but some signature in the muon trackers is generally required to identify tracks as muons; One exception is the Muon Tracking in the Calorimeter (MTC) algorithm, which is

Table 4.2: The cuts for photon identification are labeled Core0, 1, and 2 for CC and EC. Not all variables are used for all Points, This analysis uses on CC photons with identified with CCcore0. Some of the cuts are $|\eta|$ dependant via the functions $f_1(\eta) = 7.4 \cdot \eta^2 - 35.9 \cdot |\eta| + 45.7$ and $f_2(\eta) = 7.5 \cdot \eta^2 - 36.0 \cdot |\eta| + 44.8$.

Variables	CCcore0	CCcore1	CCcore2	ECcore0	ECcore1	ECcore2
Iso $<$	0.15	0.10	0.07	0.15	0.10	0.07
EMfr $>$	0.90	0.95	0.97	0.90	0.95	0.97
IsoHC4 $<$	2.0	2.0	1.5	1.5	1.5	1.5
HMx8 $<$	–	–	–	–	30	30
Sigphi $<$	18	18	18	$f_1(\eta)$	$f_1(\eta)$	$f_1(\eta)$
Sigz $>$	–	–	–	$f_2(\eta)$	$f_2(\eta)$	$f_2(\eta)$
ANN5 $>$	0.1	0.1	0.3	–	–	–
ANN4 $>$	–	–	–	0.05	0.1	0.3

quite inefficient and not considered here.

Recall that the A-layer is positioned inside the torroid and the B and C-layers are outside. Hits in the A layer are formed into *segments* as are hits in the combined BC-layers. A segment is a combinations of hits forming direction information. With both an A-layer and a BC-layer segment a muon can be reconstructed with full kinematic information, direction and momentum (actually, charge and momentum are reconstructed together, the bending is proportional to q/p). Such a reconstruction is called a *local* muon.

More common is a *central track-match* muon which fits the muon tracking information to a central track. When there is a matching central track a full reconstruction in the muon system may not be necessary, and so a central track-match muon may be matched to just a A segment or just a BC segment. With a lone A segment or BC segment it is technically possible to reconstruct a direction, and in the case of a BC segment a momentum, assuming they originate at the beam spot or primary vertex, but this is error prone and rarely done.

The muons are identified using three quality criteria: the quality of the muon information, the quality of the central track fit, and isolation. In this analysis we use muon quality `loose`, track quality `tracknewmedium`, and isolation `TopScaledMedium`.

A `loose` muon must at minimum either be constructed from a single segment formed from two wire hits and a scintillator hit matched to a central track, or a local muon with at least one scintillator hit and a segment with at least two wire hits. The matched central track is `tracknewmedium` if $|\text{dca}| < .2$ cm (dca=distance of closests approach to primary vertex) or $|\text{dac}| < .04$ cm if there are SMT hits, the track fit has at at least $\chi^2/\text{d.o.f.} < 9.5$, and there are at least 2 CFT hits. The isolation is `TopScaledMedium` if the sum of other track p_T in a $\Delta R < 0.5$ cone is $< 15\%$ of the muon p_T and the sum of E_T from the calorimeter in $0.1 < \Delta R < 0.4$ is also $< 15\%$ of the muon p_T.

Many details can found in in [34] and the update for RunIIb [35]. The simulated momentum resolution is much better than in data, and this discrepancy has worsened somewhat with recent data taken with higher instaneous luminosities. Thus, all simulations with muons include smearing that has been updated to match measured RunIIb1-2 resolutions, in particular accounting for a substantial tail in the resolution [36].

4.5 Missing E_T

We know of at least one important particle which is never directly detectable in an experiment such as DØ , the neutrino. In addition, there well may be other very weakly interacting particles originating in new models such as the gravitino in the GMSB model we focus on in this work. To identify these particles we are forced to consider a measure of the total energy imbalance, the transverse missing energy $\not{E}_T$. The total transverse momentum in a $p\bar{p}$ collision should be very nearly 0.

The $\not{E}_T$ is computed by summing the x and y-components of all calorimeter cell energies relative the detector origin,

$$\not{E}_x = \sum_i E^i \sin\theta^i \cos\phi^i \qquad \not{E}_y = \sum_i E^i \sin\theta^i \sin\phi^i \tag{4.1}$$

where uncorrected $\not{E}_T = -(E_x, E_y)$. This quantity is corrected for muons which at the energies of interest are minimum ionizing and leave a small fraction of their energy in the calorimeter. The quantity is also corrected for identified EM and hadronic jets, which have specific calibrations These corrections are accomplished by removing the associated energy deposits from the energy sum and then adding back in the correct muon, electron, photon, or jet E_x, E_y [37, 38].

A standard processor also computes a quantity called the $\not{E}_T$ a significance. The $\not{E}_T$ significance is a measure of how consistent the $\not{E}_T$ is with the variation in unclustered energy as well as the resolution of reconstructed objects such as jets, em clusters, and muons. Because this computation requires complete reconstruction from all objects it is calculated at the analysis level just before event selection. For details see [39, 40].

CHAPTER 5

Data Analysis

5.1 Signal signature

The goal of this analysis is to identify events containing three features: a Z boson decaying to electrons or muons, a photon of high transverse energy, and substantial missing energy. Events of this type are the *signal* that we will call $Z\gamma + \not{E}_T$. For our purposes these events are generally assumed to come from the "Line E" GMSB model discussed in Section 2.4 and this motivates some of the cuts we choose. All events that can be attributed to combinations of known physics and detector miss-measurement are the *background*.

We must balance two competing quantities

1. the efficiency with which signal events would be identified, and
2. the power to reject backgrounds.

Certain inefficiencies are unavoidable because of detector acceptance (via geometric coverage, detector response, and limitations of triggering), but beyond this the event selection determines the balance of expected number of signal events to background events. This determines our power to accept or reject the signal hypothesis once statistical and systematic uncertainties are accounted for.

The $Z \to \ell^+\ell^-$ in our signal provides a very clear and unique signature. Within the geometric acceptance of the detector the leptons can be reconstructed with high efficiency (about 90%) and low background. The Z decay is fully reconstructed so the pair of leptons must have opposite charge and combine to an invariant mass

$$M_{\mathrm{inv}} = \sqrt{(E_1 + E_2)^2 - |\mathbf{p}_1 + \mathbf{p}_2|^2} \tag{5.1}$$

that peaks strongly at the Z resonance (91.2 GeV). In addition, when the Z and γ originate from heavy particle decays, such as from the NLSPs of GMSB, they are more boosted than in a SM $Z\gamma$ process; this gives them uniquely high transverse momentum and keeps the signal photons largely in the CC.

5.2 Backgrounds

The SM includes a wide variety of processes that can produce the $Z\gamma + \not\!\!E_T$ signature. At one end of the spectrum are pure quantum chromodynamics (QCD) processes producing hadronic jets which have very high cross section, but they require multiple fakes combining to substantial invariant mass to produce our signal. On the other end of the spectrum are rare events that frequently produce $Z\gamma + \not\!\!E_T$, such as ZW events where the electron in $W \to e\nu$ is mistaken for a photon or $Z\gamma$ where instrumental limitations sometimes lead to high $\not\!\!E_T$. Because $\not\!\!E_T$ resolution is relatively poor and production of $Z\gamma$ is substantial this $Z\gamma + X$ process dominates the background.

SM production of $Z\gamma$ can itself be divided into two somewhat different processes, initial state radiation (ISR) and final state radiation (FSR). In ISR the photon is radiated from an initial quark, while in FSR the photon is radiated from one of the lepton decay products of the Z. Each is illustrated as a Feynman diagram in Figure 5.1.

In general FSR photons have lower p_T, are close to one of the final state leptons in direction, are associated with low di-lepton invariant mass ($M(\ell\bar{\ell})$), and have three-body invariant mass ($M(\ell\bar{\ell}\gamma)$) close to the Z mass. These events can be partially

Figure 5.1: Feynman diagram for the production of $Z\gamma$ via photon ISR (left) and FSR (right).

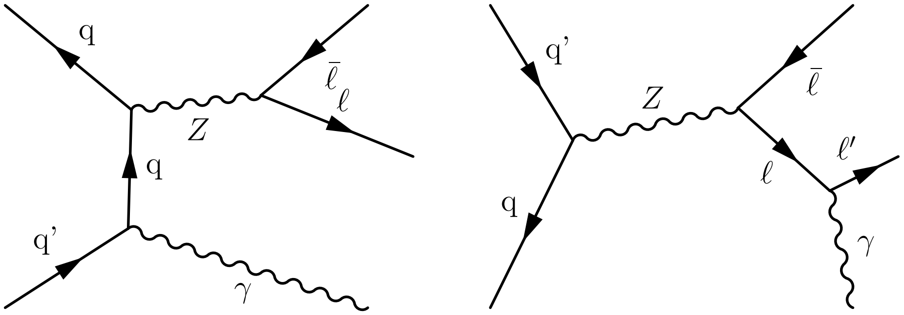

rejected by a ΔR cut requiring the photon be sufficiently separated from each of the two leptons. The minimum photon p_T requirement and invariant mass cuts also contribute to rejection. On the other hand, ISR photons have kinematics much closer to the signal. The power to distinguish these events from signal comes mainly from $\not{E}_T$ and $p_T(\gamma)$. The distinction between ISR and FSR is very clear in the three-body versus two-body distribution from data in Figure 5.2.

Besides $Z\gamma$, other backgrounds must be considered, though their contributions may be small.

QCD multi-jet

As already mentioned, two or more jets can conspire to produce lepton and photon signatures. These events may contain real leptons and photons from pion decays, but these are usually of low p_T and very unlikely to appear in invariant mass combinations at the Z mass or higher. Real missing energy, such as from neutrinos from charged pion decays is also expected to be small, but limitations in the calorimeter can occasionally lead to large $\not{E}_T$. This background will be estimated using a data-driving method.

Z+jets

The Z is frequently produced along with jets from quark or gluon ISR (for

Figure 5.2: The three-body mass $M(\ell\ell\gamma)$ versus the two-body mass $M(\ell\ell)$ for $ee\gamma$ and $\mu\mu\gamma$ events in data. A diagonal dashed green line indicates the $M(\ell\ell\gamma) > M(\ell\ell)$ limit (there is gap of about 10 GeV to the data because of the $p_T(\gamma) > 10$ GeV cut). The peak along the horizontal $M(\ell\ell\gamma) = M_Z$ is from FSR events, and the peak along the vertical $M(\ell\ell) = M_Z$ is from ISR events.

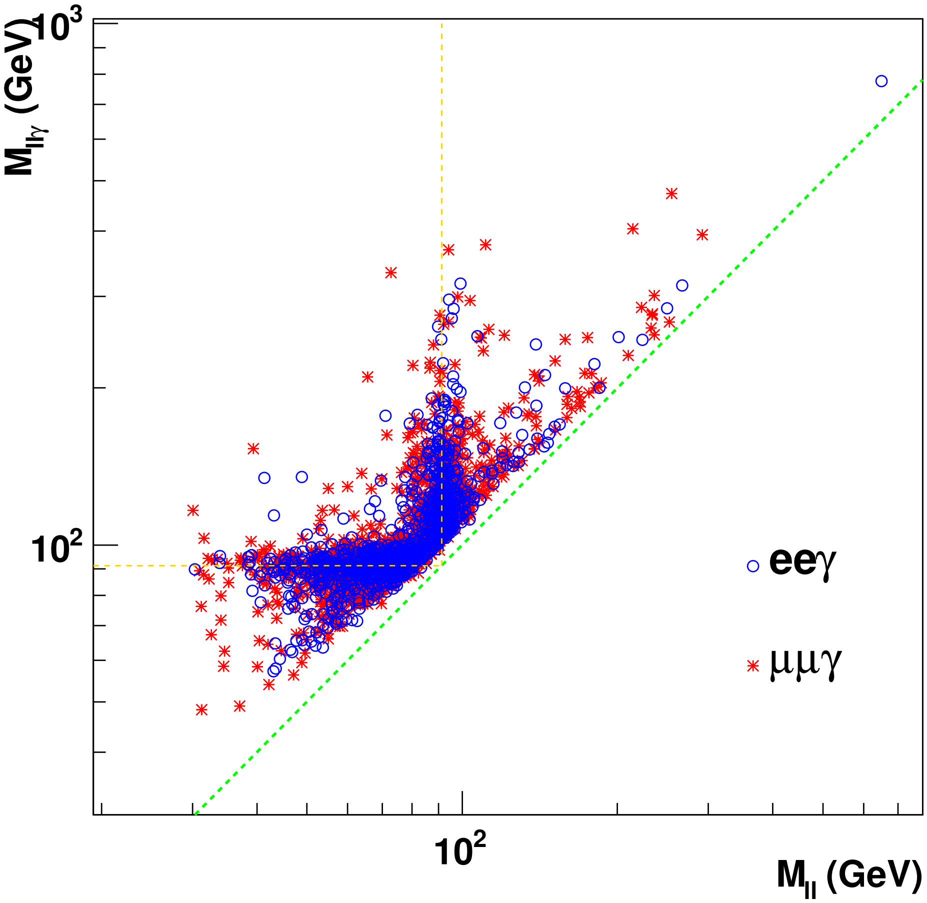

example, the leading order contribution would be identical to the left diagram of Figure 5.1 but replacing the photon with a gluon). These events have much lower cross section than QCD but require only a single jet $\sim \gamma$ fake. These events are similar to QCD with regard to $\not{E}_T$. This background will be estimated using a data-driving method.

$W + X \to \ell\nu + X$

The cross section for W+jet production is about 10× that of Z+jets with leptonic decays, but a fake lepton with invariant mass near the Z peak is required in addition to a photon. The $W\gamma$ cross section is only about 3× that of $Z\gamma$ [41, 42]. These events have a substantial $\not{E}_T$ ($\sim$ 40 GeV) from the neutrino in the leptonic decay of W. A limit on this background is made using data and cross-checked with Monte Carlo (MC) simulation.

$t\bar{t}/WW$

The production of $t\bar{t}$ and WW are similar except that $t\bar{t}$ also includes two b-jets. The cross section is much smaller than Z+jets and does not include a real Z, but the decays may produce a pair of high p_T leptons along with substantial real missing energy. This background is estimated with MC simulation.

ZW/ZZ

These events are very rare, but do contain a real Z and either jets from the hadronic decay of the other boson or real missing energy from $W \to \ell\nu$ or $Z \to \nu\bar{\nu}$. This background is estimated with MC simulation.

5.3 Datasets and triggers

Run II can be broken down into four periods separated by shutdowns during which repairs and small changes to the detector were made. These are known as RunIIa, RunIIb1, RunIIb2, and RunIIb3. The datasets used for this analysis comes from the

Table 5.1: The data used for the $ee\gamma+\not\!\!E_T$ event selection. These events were skimmed from the full RunII data by the CSG, selecting for two high-p_T EM objects.

Dataset name	Run	Data size	Number of events
`CSG_CAF_2EMhighpt_PASS3_p18.14.00`	RunIIa	1.59TB	36,294,680
`CSG_CAF_2EMhighpt_PASS2_p21.10.00`	RunIIb1	1.64TB	29,190,479
`CSG_CAF_2EMhighpt_PASS4_p21.10.00_p20.12.00`	RunIIb2	557.14GB	9,418,773
`CSG_CAF_2EMhighpt_PASS4_p21.10.00_p20.12.01`	RunIIb2	58.26GB	894,319
`CSG_CAF_2EMhighpt_PASS4_p21.10.00_p20.12.02`	RunIIb2	1.27TB	19,586,614
`CSG_CAF_2EMhighpt_PASS4_p21.10.00_p20.12.04`	RunIIb2	23.67GB	335,636
`CSG_CAF_2EMhighpt_PASS4_p21.12.00_p20.12.05_allfix`	RunIIb2	2.28TB	33,678,841
`CSG_CAF_2EMhighpt_PASS5_p21.18.00_p20.16.07_fix`	RunIIb3	0.64TB	10,027,490
`CSG_CAF_2EMhighpt_PASS5_p21.18.00_p20.16.07_reduced2`	RunIIb3	0.95TB	13,681,078
`CSG_CAF_2EMhighpt_PASS5_p21.18.00_p20.16.08`	RunIIb3	1.25TB	17,768,892
Total		10.3TB	170,877,011

entirety of DØ 's Run IIb up to the summer 2010 shutdown on 18 July 2010 (RunIIb1-3). The run ranges are 222028-234913 for RunIIb1, 237342-252918 for RunIIb2, and 255328-262856 for RunIIb3. The total integrated luminosity is 6.2 fb^{-1} with a 6.1% uncertainty.

This analysis uses data skimmed for events with two high-p_T EM objects (Table 5.1) or two high-p_T muons objects (Table 5.2). The objects are only required to pass very loose requirements. The `2EMhighpt` skim selects events with two EM clusters which have $E_T > 12$ GeV, EM fraction > 0.9 and loose isolation. The `2MUhighpt` skim selects events with either two loose muons matched to central tracks of $p_T > 10$ GeV, two loose muons with one matched to a central track of $p_T > 15$ GeV, or one medium muon with track $p_T > 15$ GeV and two additional tracks with $p_T > 15$ GeV.

Events are required to satisfy standard D0 data quality criteria which means events must be recorded with all detectors in a good state. This analysis uses version v2010-07-18 of the data quality package, dq_defs [43]. Data quality is flagged at the level of *luminosity blocks*, which are small subsets of runs. Data quality issues may include such things as a tripped power supply leaving a large portion of the detector off or certain known anomalous calorimeter noise patterns.

Analyzed events must have been triggered by at least one of a standard set of

Table 5.2: The data used for the $\mu\mu\gamma+\not\!\!E_T$ event selection. These events were skimmed from the full RunII data by the CSG, selecting for two high-p_T muon objects.

Dataset name	Run	Data size	Number of events
`CSG_CAF_2MUhighpt_PASS3_p18.14.00`	RunIIa	545.61GB	9,776,282
`CSG_CAF_2MUhighpt_PASS2_p21.10.00`	RunIIb1	1.20TB	15,141,203
`CSG_CAF_2MUhighpt_PASS4_p21.10.00_p20.12.00`	RunIIb2	444.70GB	5,439,158
`CSG_CAF_2MUhighpt_PASS4_p21.10.00_p20.12.01`	RunIIb2	51.28GB	594,548
`CSG_CAF_2MUhighpt_PASS4_p21.10.00_p20.12.02`	RunIIb2	1.15TB	13,191,811
`CSG_CAF_2MUhighpt_PASS4_p21.10.00_p20.12.04`	RunIIb2	11.17GB	127,786
`CSG_CAF_2MUhighpt_PASS4_p21.12.00_p20.12.05_allfix`	RunIIb2	2.34TB	25,093,718
`CSG_CAF_2MUhighpt_PASS5_p21.18.00_p20.16.07_fix`	RunIIb3	0.52TB	6,154,623
`CSG_CAF_2MUhighpt_PASS5_p21.18.00_p20.16.07_reduced2`	RunIIb3	1.15TB	11,473,094
`CSG_CAF_2MUhighpt_PASS5_p21.18.00_p20.16.08`	RunIIb3	1.64TB	15,564,931
Total		9.0TB	102,557,154

triggers that require a single EM or μ object. The efficiency of this trigger combination is approximately 99% for the pair of high p_T objects required in this analysis.

5.4 Monte Carlo modeling

The GMSB signal and many of the standard model backgrounds are modeled with MC events in a full simulation of the DØ detector. These events are created in stages called *generation*, *simulation*, *digitization*, and *reconstruction*. In event generation hard scattering events are created of a specific type; say GMSB, Z+jets, or $t\bar{t}$. All the physics that would occur at short distances before reaching the detector are also created at this stage; this includes such things as the Z decay and quark hadronization to jets. The simulation stage recreates the particles interactions with the material of the detector, and the digitization stage recreates the measurement made by detector. The output of digitization is much like real data from the detector and so goes through the same reconstruction software. The output format produced by reconstruction is called TMB; as a final technical step results are written to an additional analysis format called CAF.

After a shutdown changes to the detectors need to be accounted for in the simulation. For now there are two releases relevant to this study, p20.03.09 and p20.15.04, the first models RunIIb1 conditions and and the second models RunIIb2 condi-

Table 5.3: GMSB model line E cross sections as computed with ISAJET.

Λ	σ (fb)	br($\tilde{\chi}_1^0 \to \gamma\tilde{G}$)	br($\tilde{\chi}_1^0 \to Z\tilde{G}$)	$M(\chi_1^0)$	$M(\chi_1^\pm)$	$M(\chi_2^0)$
65.	189.8	0.976	0.00450	99.0	117.3	141.3
70.	145.7	0.892	0.0864	111.1	129.1	151.7
75.	111.9	0.715	0.253	123.0	140.8	162.1
80.	85.68	0.545	0.408	135.0	152.4	172.5
85.	65.60	0.420	0.519	146.8	163.9	183.0
90.	50.32	0.335	0.592	158.6	175.4	193.6
100.	29.60	0.234	0.674	182.1	198.1	214.7
110.	17.46	0.179	0.714	205.4	220.7	235.9
120.	10.31	0.146	0.737	228.5	243.2	257.2
140.	3.565	0.106	0.760	274.4	287.8	300.0

tions. An official simulation for RunIIb3 was not available, but this analysis uses MC reweightings of the RunIIb2 simulation applicable to combined RunIIb2 and 3 data. For the less important background processes we use only RunIIb1 simulation with weights for all RunIIb1,2,3.

The signal MC is generated with ISAJET [44, 45] interfacing with PYTHIA. The dataset names and number of events are listed in Table 5.4. A mass spectrum was first produced using `isasugra` for the minimal model in which the μ parameter is determined. Then, $\mu = \frac{3}{4}M_1$ is set and a new mass spectrum and branching ratios are computed by `isasusy`. This is interfaced to Pythia via the Supersymmetry Les Houches Accord (SLHA) standard for generation [46]. Cross sections for normalization were computed with `isajet` (`Isasugra`, `isasusy`, and `isajet` are all part of the ISAJET package). Cross sections, the branching ratio of the NLSP decay to Z, some particle masses are given in Figure 5.3.

The SM background processes were generated with either ALPGEN+PYTHIA or PYTHIA [47, 48] and fully simulated. The processes Z+jets and W+jets used ALPGEN+PYTHIA where ALPGEN produces the hard scattering process and PYTHIA completes the process with, for example, the hadronic showering. This is preferred to plain PYTHIA for simulating jet multiplicities in these vector boson events, but isn't impor-

Table 5.4: MC samples used to model the GMSB model line E signal.

Process	Generator	SAM definition name	Number of events
GMSB $\Lambda = 65$ TeV	Isajet+Pythia	wilsona_gmsb_linee_lambda65_run2b1_v1	179719
GMSB $\Lambda = 70$ TeV	Isajet+Pythia	wilsona_gmsb_linee_lambda70_run2b1_v1	206159
GMSB $\Lambda = 75$ TeV	Isajet+Pythia	wilsona_gmsb_linee_lambda75_run2b1_v1	205380
GMSB $\Lambda = 80$ TeV	Isajet+Pythia	wilsona_gmsb_linee_lambda80_run2b1_v1	212401
GMSB $\Lambda = 85$ TeV	Isajet+Pythia	wilsona_gmsb_linee_lambda85_run2b1_v1	213169
GMSB $\Lambda = 90$ TeV	Isajet+Pythia	wilsona_gmsb_linee_lambda90_run2b1_v1	209033
GMSB $\Lambda = 95$ TeV	Isajet+Pythia	wilsona_gmsb_linee_lambda95_run2b1_v1	217039
GMSB $\Lambda = 100$ TeV	Isajet+Pythia	wilsona_gmsb_linee_lambda100_run2b1_v1	213413
GMSB $\Lambda = 110$ TeV	Isajet+Pythia	wilsona_gmsb_linee_lambda110_run2b1_v1	208254
GMSB $\Lambda = 120$ TeV	Isajet+Pythia	wilsona_gmsb_linee_lambda120_run2b1_v1	207177
GMSB $\Lambda = 65$ TeV	Isajet+Pythia	wilsona_gmsb_linee_lambda65_run2b2_v1	188265
GMSB $\Lambda = 70$ TeV	Isajet+Pythia	wilsona_gmsb_linee_lambda70_run2b2_v1	24103
GMSB $\Lambda = 75$ TeV	Isajet+Pythia	wilsona_gmsb_linee_lambda75_run2b2_v1	207642
GMSB $\Lambda = 80$ TeV	Isajet+Pythia	wilsona_gmsb_linee_lambda80_run2b2_v1	217927
GMSB $\Lambda = 85$ TeV	Isajet+Pythia	wilsona_gmsb_linee_lambda85_run2b2_v1	211658
GMSB $\Lambda = 90$ TeV	Isajet+Pythia	wilsona_gmsb_linee_lambda90_run2b2_v1	24210
GMSB $\Lambda = 95$ TeV	Isajet+Pythia	wilsona_gmsb_linee_lambda95_run2b2_v1	206789
GMSB $\Lambda = 100$ TeV	Isajet+Pythia	wilsona_gmsb_linee_lambda100_run2b2_v1	215142
GMSB $\Lambda = 110$ TeV	Isajet+Pythia	wilsona_gmsb_linee_lambda110_run2b2_v1	210221
GMSB $\Lambda = 120$ TeV	Isajet+Pythia	wilsona_gmsb_linee_lambda120_run2b2_v1	210130

tant for this analysis, comparisons to a Pythia sample yielded similar results. Other Pythia samples considered include diboson (WW, WZ, ZZ) and $t\bar{t}$, matrix element $Z+\gamma$, and EM-like jets for jet faking photon studies. They are all listed in Table 5.5.

When MC is used the events are reweighted using a few standard processors. All MC events are overlayed at the digitization stage with *minimum bias* data to model backgrounds and interactions not coming from the hard scattering. Minimum bias data comes from a random selection of interactions passing the loosest of triggers, it is dominated by elastic, diffractive, and very low p_T QCD interactions. This minimum bias overlay may come from a luminosity spectrum that does not match data, so a reweighting to match the luminosity is data is applied. There is also a beam position weight and in the case of Z+jets a reweighting to match the $p_T(Z)$ to data since this not well modelled when events are generated [49].

Additional weights are also applied that correspond to the discrepancy between data and MC for object reconstruction and identification efficiency. There is a weight for electrons [50, 51], photons [52], and muons [35]. The weights average 0.88 for electron identification, 0.998 for the electron trigger probability, 0.98 for muon iden-

Table 5.5: MC samples used to model SM backgrounds.

Process	Generator	SAM definition name	Number of events
Z+jets→ ee+jets	Alpgen+Pythia	CSG_alpgenpythia_gamz_ee_15_75_p211100_v9	17533290
Z+jets→ ee+jets	Alpgen+Pythia	CSG_alpgenpythia_gamz_ee_75_130_p211100_v9	30713059
Z+jets→ ee+jets	Alpgen+Pythia	CSG_alpgenpythia_gamz_ee_130_250_p211100_v9	1500601
Z+jets→ ee+jets	Alpgen+Pythia	CSG_alpgenpythia_gamz_ee_250_1960_p211100_v9	2549541
Z+jets→ ee+jets	Alpgen+Pythia	CSG_alpgenpythia_gamz_ee_15_75_p211800_Run2b2_v3	10586441
Z+jets→ ee+jets	Alpgen+Pythia	CSG_alpgenpythia_gamz_ee_75_130_p211800_Run2b2_v3	10397501
Z+jets→ ee+jets	Alpgen+Pythia	CSG_alpgenpythia_gamz_ee_130_250_p211800_Run2b2_v3	1356697
Z+jets→ ee+jets	Alpgen+Pythia	CSG_alpgenpythia_gamz_ee_250_1960_p211800_Run2b2_v3	849821
Z+jets→ $\mu\mu$+jets	Alpgen+Pythia	CSG_alpgenpythia_gamz_mumu_15_75_p211100_v9	16118936
Z+jets→ $\mu\mu$+jets	Alpgen+Pythia	CSG_alpgenpythia_gamz_mumu_75_130_p211100_v9	31630328
Z+jets→ $\mu\mu$+jets	Alpgen+Pythia	CSG_alpgenpythia_gamz_mumu_130_250_p211100_v9	1397000
Z+jets→ $\mu\mu$+jets	Alpgen+Pythia	CSG_alpgenpythia_gamz_mumu_250_1960_p211100_v9	1931252
Z+jets→ $\mu\mu$+jets	Alpgen+Pythia	CSG_alpgenpythia_gamz_mumu_15_75_p211800_Run2b2_v3	9848040
Z+jets→ $\mu\mu$+jets	Alpgen+Pythia	CSG_alpgenpythia_gamz_mumu_75_130_p211800_Run2b2_v3	10341024
Z+jets→ $\mu\mu$+jets	Alpgen+Pythia	CSG_alpgenpythia_gamz_mumu_130_250_p211800_Run2b2_v3	1352792
Z+jets→ $\mu\mu$+jets	Alpgen+Pythia	CSG_alpgenpythia_gamz_mumu_250_1960_p211800_Run2b2_v3	848230
Z+jets→ $\tau\tau$+jets	Alpgen+Pythia	CSG_alpgenpythia_gamz_tautau_15_75_p211100_v3	2932722
Z+jets→ $\tau\tau$+jets	Alpgen+Pythia	CSG_alpgenpythia_gamz_tautau_75_130_p211100_v3	2670851
Z+jets→ $\tau\tau$+jets	Alpgen+Pythia	CSG_alpgenpythia_gamz_tautau_130_250_p211100_v3	921039
Z+jets→ $\tau\tau$+jets	Alpgen+Pythia	CSG_alpgenpythia_gamz_tautau_250_1960_p211100_v3	1590915
$t\bar{t}$	Alpgen	CSG_alpgenpythia_t+t_2l+2nu+2b_m172_p211100_v3	1489496
$t\bar{t}$	Alpgen	CSG_alpgenpythia_t+t_lnu+2b+2lpc_m172_p211100_v3	1563304
$t\bar{t}$	Alpgen	CSG_alpgenpythia_t+t_2b+4lpc_m172_p211100_v3	1534905
WW, WZ, ZZ	Pythia	CSG_pythia_diboson_incl_p211100_v3	1889856
W+jets→ $\ell\nu$+jets	Alpgen+Pythia	CSG_alpgenpythia_w+0lp_lnu+0lp_excl_p211100_v9	113352357
W+jets→ $\ell\nu$+jets	Alpgen+Pythia	CSG_alpgenpythia_w+1lp_lnu+1lp_excl_p211100_v9	59068229
W+jets→ $\ell\nu$+jets	Alpgen+Pythia	CSG_alpgenpythia_w+2lp_lnu+2lp_excl_p211100_v9	35559542
W+jets→ $\ell\nu$+jets	Alpgen+Pythia	CSG_alpgenpythia_w+3lp_lnu+3lp_excl_p211100_v9	16130867
W+jets→ $\ell\nu$+jets	Alpgen+Pythia	CSG_alpgenpythia_w+4lp_lnu+4lp_excl_p211100_v9	6816110
W+jets→ $\ell\nu$+jets	Alpgen+Pythia	CSG_alpgenpythia_w+5lp_lnu+5lp_incl_p211100_v9	3172852
W+jets→ $\ell\nu$+jets	Alpgen+Pythia	CSG_alpgenpythia_w+0lp_lnu+0lp_excl_p211800_Run2b2_v3	176679537
W+jets→ $\ell\nu$+jets	Alpgen+Pythia	CSG_alpgenpythia_w+1lp_lnu+1lp_excl_p211800_Run2b2_v3	88675764
W+jets→ $\ell\nu$+jets	Alpgen+Pythia	CSG_alpgenpythia_w+2lp_lnu+2lp_excl_p211800_Run2b2_v3	33906880
W+jets→ $\ell\nu$+jets	Alpgen+Pythia	CSG_alpgenpythia_w+3lp_lnu+3lp_excl_p211800_Run2b2_v3	9004108
W+jets→ $\ell\nu$+jets	Alpgen+Pythia	CSG_alpgenpythia_w+4lp_lnu+4lp_excl_p211800_Run2b2_v3	2291070
W+jets→ $\ell\nu$+jets	Alpgen+Pythia	CSG_alpgenpythia_w+5lp_lnu+5lp_incl_p211800_Run2b2_v3	963247
$Z + \gamma \to ee + \gamma$	Pythia	wilsona_pythia_gam+z_gam+ee_pt8_p211100_v2	1098822
$Z + \gamma \to \mu\mu + \gamma$	Pythia	wilsona_pythia_gam+z_gam+mumu_pt8_p211100_v2	1278814
$Z + \gamma \to \mu\mu + \gamma$	Pythia	wilsona_pythia_gam+z_gam+mumu_pt8_p211800_v2	925818
EM-like QCD jets	Pythia	wilsona_qcd_emjet_pt10_20_run2b1	1186880
EM-like QCD jets	Pythia	wilsona_qcd_emjet_pt20_30_run2b1	66750
EM-like QCD jets	Pythia	wilsona_qcd_emjet_pt30_40_run2b1	898590
EM-like QCD jets	Pythia	wilsona_qcd_emjet_pt40_60_run2b1	887170
EM-like QCD jets	Pythia	wilsona_qcd_emjet_pt60_80_run2b1	890579
EM-like QCD jets	Pythia	wilsona_qcd_emjet_pt80_120_run2b1	871243
EM-like QCD jets	Pythia	wilsona_qcd_emjet_pt20_30_run2b1_v2	1282733
EM-like QCD jets	Pythia	wilsona_qcd_emjet_pt30_40_run2b1_v2	2041247
EM-like QCD jets	Pythia	wilsona_qcd_emjet_pt40_60_run2b1_v2	1849282
EM-like QCD jets	Pythia	wilsona_qcd_emjet_pt60_80_run2b1_v2	2219254
EM-like QCD jets	Pythia	wilsona_qcd_emjet_pt80_120_run2b1_v2	2223464

tification, 0.81 for the muon trigger probability, and 0.92 for photon identification.

5.5 Selection of Z

To make the initial selection of the Z signal we require two opposite sign leptons of the same type, with high p_T and substantial invariant mass,

1. $p_T(\ell_{1,2}) > 15$ GeV, opposite sign
2. $p_T(e_{\text{leading}}) > 25$ GeV, $p_T(\mu_{\text{leading}}) > 20$ GeV
3. $M(\ell\ell) > 30$ GeV

Additionally, in the electron case one is required to be in the CC.

Plots of data versus MC in invariant mass are shown in Figures 5.3 and 5.4, scaled versions of the GSMB signal model are also shown. The MC matches the data quite well here. The mass peak was fitted in both cases to a Gaussian convolved with the Breit-Wigner distribution and the half-width at half-maximum (HWHM) was found to be 4.34 GeV for the $e\bar{e}$ case and 8.28 GeV for the $\mu\bar{\mu}$ case. The broader peak for the muon case is because the momentum resolution of high-p_T muons is substantially worse than electrons. This is because muons are not measured in the calorimeter and instead rely solely on tracking, and at high momenta the bending in the magnetic fields is small enough to approach the tracking resolution. The fits yield a peak value at 91.0 and 90.03 GeV for the electron and muon cases, respectively.

To more strongly select events with a Z boson we cut at $M_{Z,\text{fit}} \pm 3$ HWHM. Rounding these off this yields the requirements $78 < M(ee) < 104$ GeV and $65 < M(\mu\mu) < 115$ GeV. These cuts are also indicated in the figures.

5.5.1 Angle between muons and missing energy

The muon sample includes a substantial number of muons with very poorly reconstructed momentum. If the muon is reconstructed incorrectly in general is most likely

Figure 5.3: Comparison of data versus background model in the invariant mass of inclusive opposite-sign di-electron events. The last bin includes overflow.

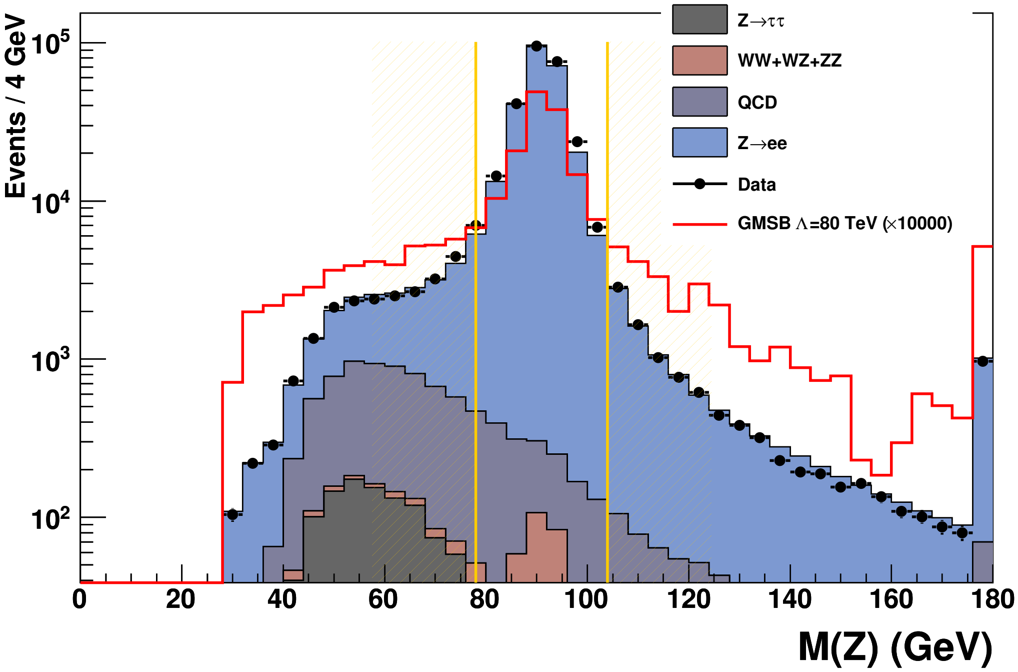

Figure 5.4: Comparison of data versus background model in the invariant mass of inclusive opposite-sign di-muon events. The last bin includes overflow.

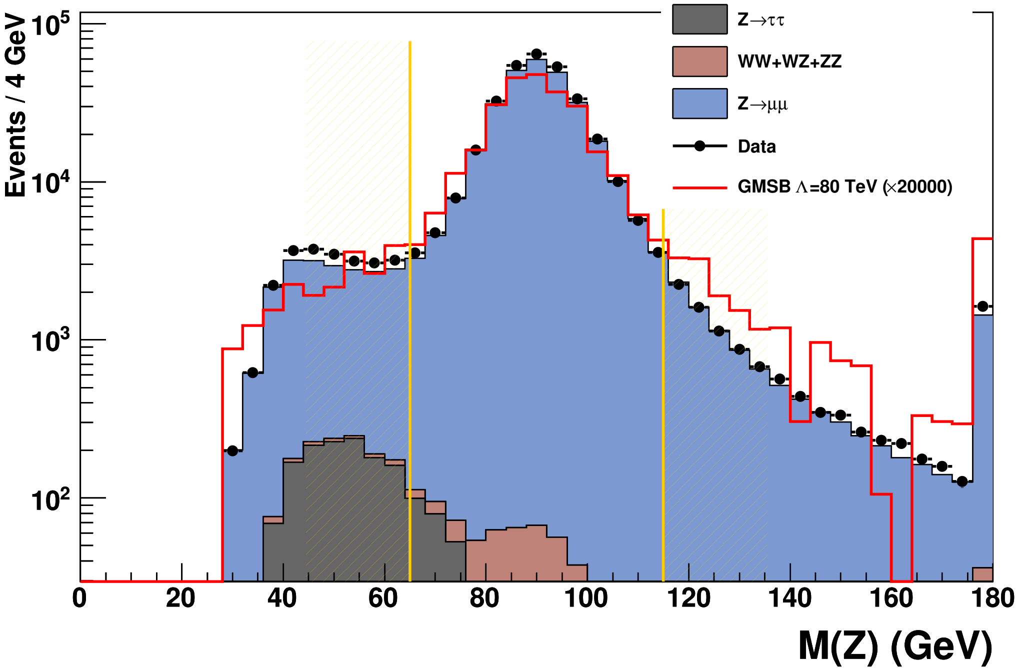

Figure 5.5: The distribution of $\Delta\phi$ between the higher (a) or lower (b) p_T muon and the missing energy ϕ direction as a function of $\not{E}_T$. A clear clustering at $\Delta\phi = \pi$ for the leading muon and $\Delta\phi = 0$ for the trailing muon is seen, indicating that many of the high $\not{E}_T$ events in this sample are just due to muon reconstruction error. Cuts are shown with red lines at $\pi - \pi/32$ in (a) and $\pi/32$ in (b). This uses data events with basic di-muon requirements: $15, 20$ GeV $< p_T(\mu_2, \mu_1)$ and 70 GeV $< M(\mu^+\mu^-)$.

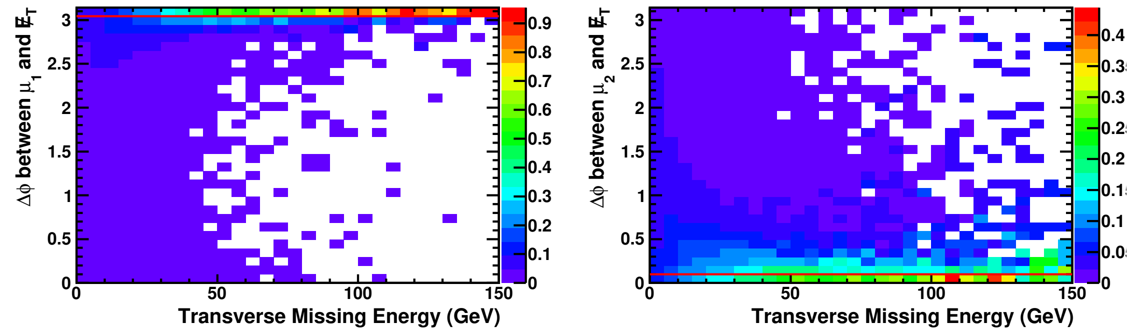

(a) (b)

that the higher p_T muon was the that shifted up in p_T and/or the lower p_T muon to have shifted down. An object with an excess of reconstructed p_T adds an artificial contribution to the calculated $\not{E}_T$ in the opposite direction; the $\not{E}_T$ increases in the same direction for an p_T reconstructed too low. If the missing energy is small relative to the reconstruction error then the $\not{E}_T$ direction is expected to be strongly correlated or anti-correlated with the muon direction. This is quite easy to see in Figure 5.5 using inclusive $\mu^+\mu^-$ data with a loose cut of 70 GeV $< M_{\mu^+\mu^-}$. Vertical slices in $\not{E}_T$ have been normalized to emphasize the shape along the vertical $\Delta\phi(\mu, \not{E}_T)$ axis. The clustering toward $\Delta\phi = \pi$ for the leading muons and toward $\Delta\phi = 0$ for the trailing muons indicate muon reconstruction errors substantial enough to dominate the $\not{E}_T$. The red lines show cuts $\pi/32$ away from the edges. For electron events the distribution is substantially better, nearly flat in $\Delta\phi$.

Figure 5.6: Comparison of data versus background model in the three body invariant mass $M(ee\gamma)$ in events with $p_T(\gamma) > 10$ GeV. The last bin includes overflow.

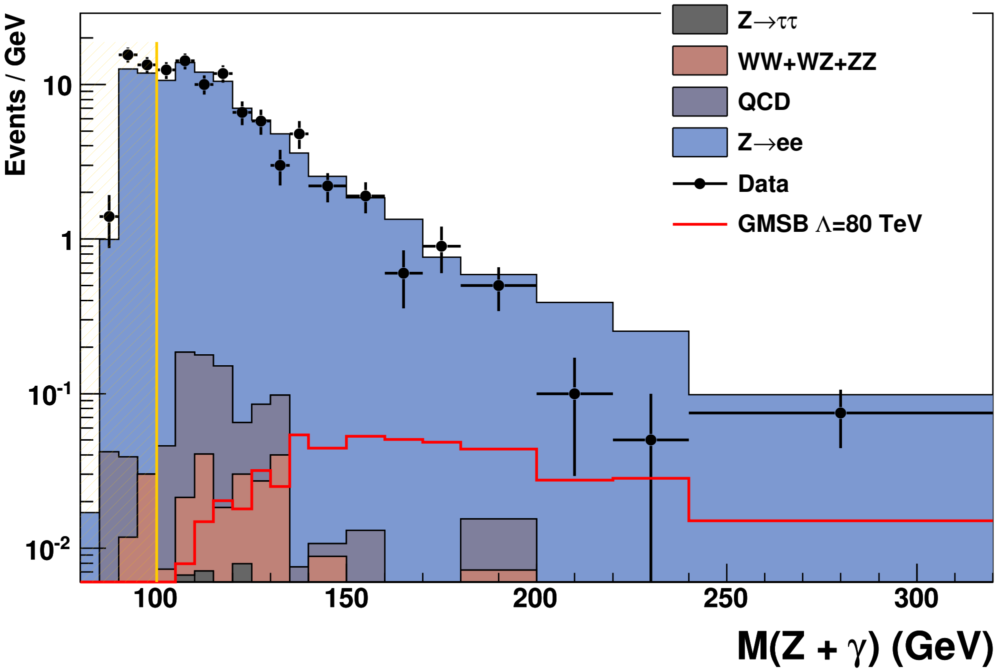

5.6 Selection of $Z + \gamma$

Initially the photon is required to have $p_T > 10$ GeV. It must be separated from the two leptons and any jets by $\Delta R > 0.7$; since our signal has prompt photons that should be relatively isolated this tends to reject radiatively produced photons from SM backgrounds.

When an FSR photon is radiated it takes away energy from the Z decay leptons, the result of which is that we see the strong horizontal grouping of events Figure 5.2 corresponding to a three-body mass $M(\ell\ell\gamma)$ near the Z mass. When the on-shell Z in our signal is combined in three-body invariant mass with the prompt photon we tend to get values much larger than M_Z. Thus we introduce the cut 100 GeV $< M(\ell\ell\gamma)$ for both channels. This is illustrated in Figures 5.6 and 5.7.

On top of the three-body mass cut we also tighten the photon p_T requirement. The prompt photons from the GMSB signal are produced via the decay of heavy

Figure 5.7: Comparison of data versus background model in the three body invariant mass $M(\mu\mu\gamma)$ in events with $p_T(\gamma) > 10$ GeV. The last bin includes overflow.

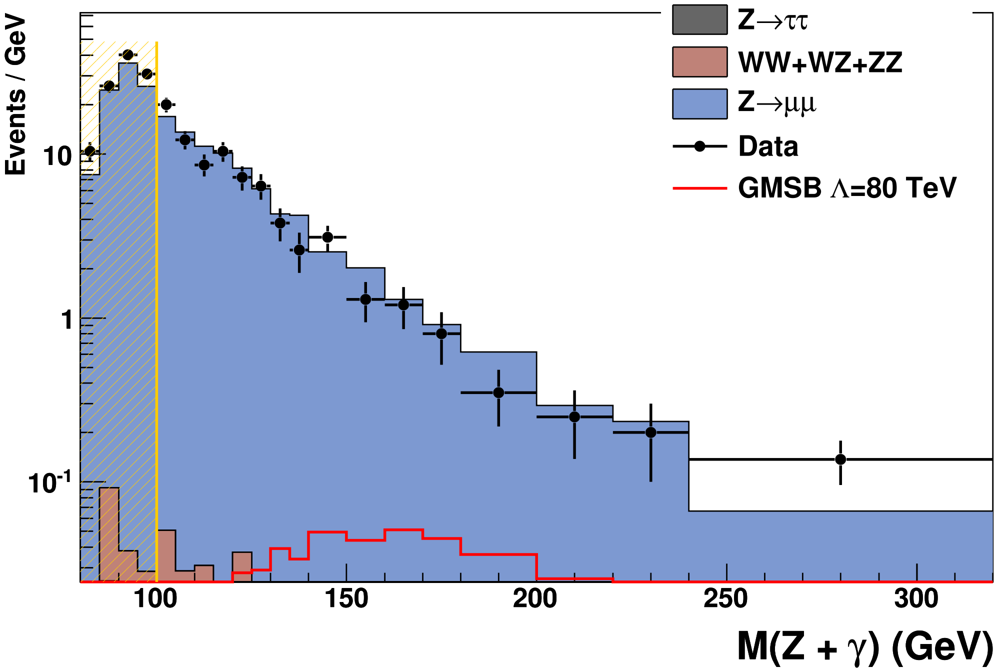

particles which give them a large transverse boost. This distinguishes them from the SM photons which show an exponentially decaying p_T spectrum. We select the cut 30 GeV $< p_T(\gamma)$ as shown in Figures 5.8 and 5.9. (Similarly, the Z is also boosted and its reconstructed p_T shows a similarly distinguishing feature in the signal.)

Finally, the signal is expected to have large $\not{E}_T$so we cut events with $\not{E}_T$lower than 30 GeV for both channels. There are substantial differences between the electron and muon channels here again because of the muon momentum resolution. The leptons are an important part of the $\not{E}_T$combination and so mis-measurements of their kinematics broadens the $\not{E}_T$resolution. Thus we see a longer tail in the $\not{E}_T$for both data and MC. The MC benefits from a recent update to the muon smearing processor that, though it doesn't improve the reconstruction resolution, at least ensures that MC better models data [36]. The $\not{E}_T$spectrum of background, signal, and data is shown in Figures 5.10 and 5.11.

We summarize the results of this sequence of cuts in Table 5.6 for the electrons

Figure 5.8: Comparison of data versus background model in the $p_T(\gamma)$ distribution in $ee\gamma$ events with $M(ee\gamma) > 100$ GeV. The last bin includes overflow.

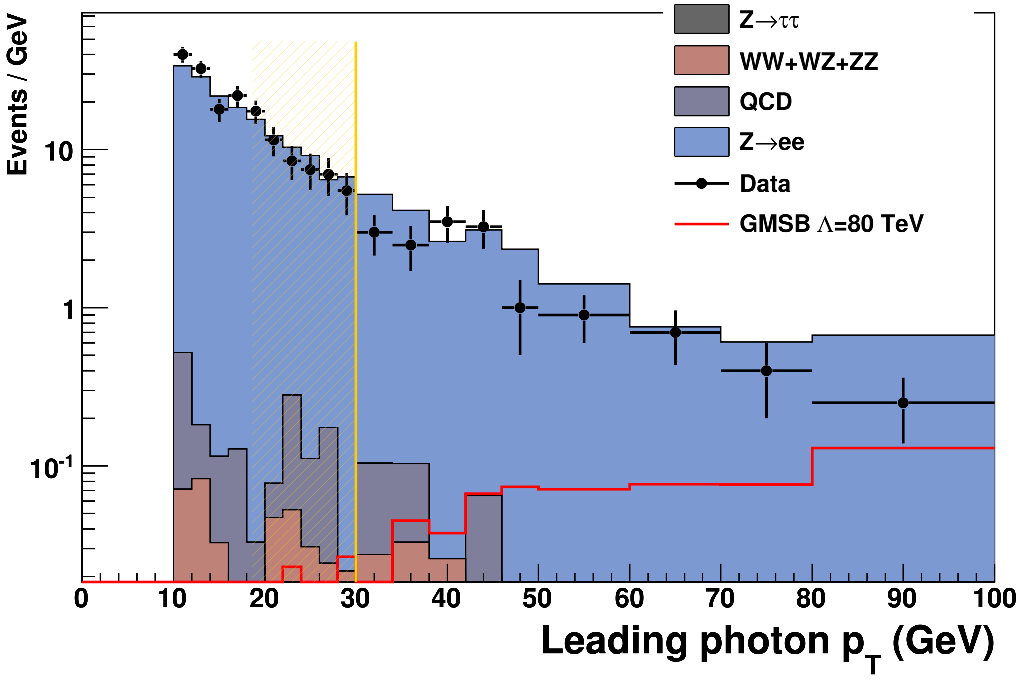

Figure 5.9: Comparison of data versus background model in the $p_T(\gamma)$ distribution in $\mu\mu\gamma$ events with $M(\mu\mu\gamma) > 100$ GeV. The last bin includes overflow. The last bin includes overflow.

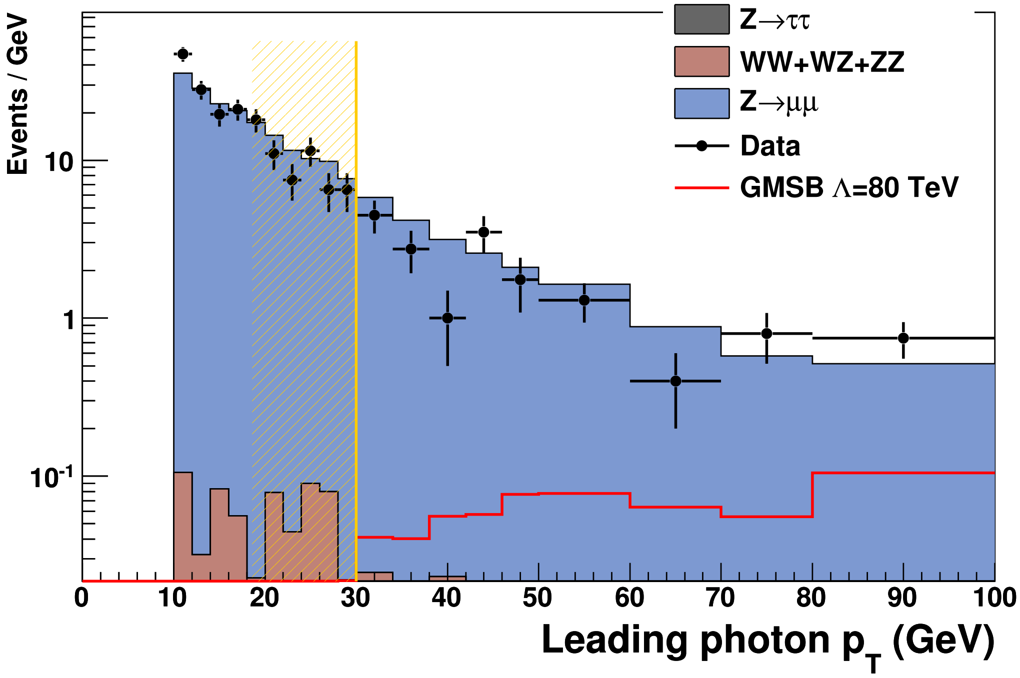

Figure 5.10: Comparison of data versus background model in the $\not\!\!E_T$for $ee\gamma$ events with $M(ee\gamma) > 100$ GeV and $p_T(\gamma) > 30$ GeV. The last bin includes overflow.

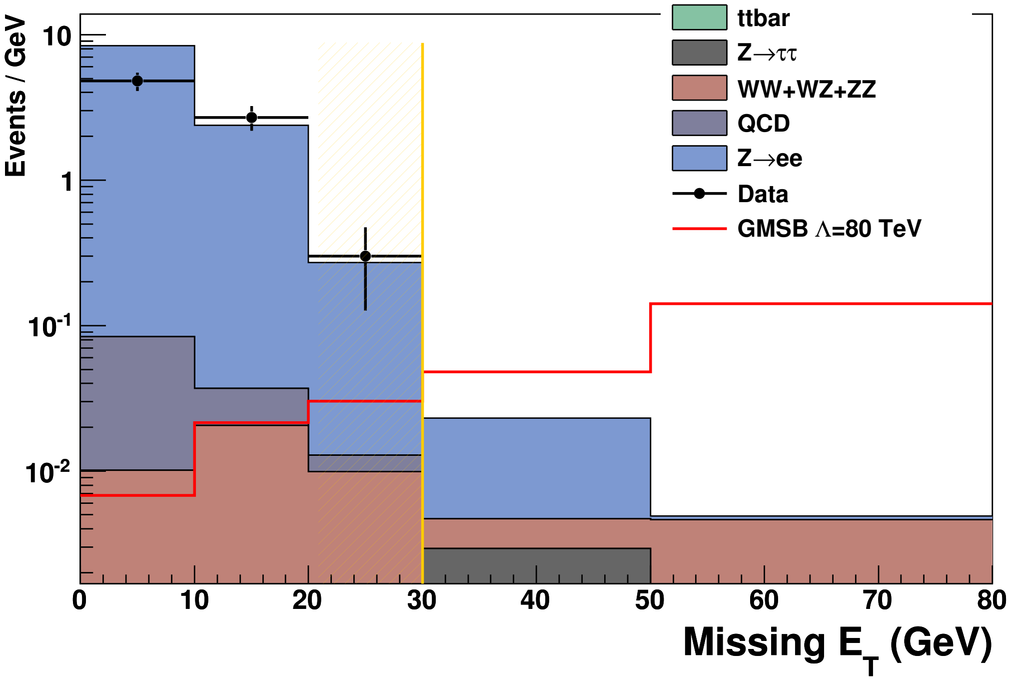

Figure 5.11: Comparison of data versus background model in the $\not\!\!E_T$for $\mu\mu\gamma$ events with $M(\mu\mu\gamma) > 100$ GeV and $p_T(\gamma) > 30$ GeV. The last bin includes overflow.

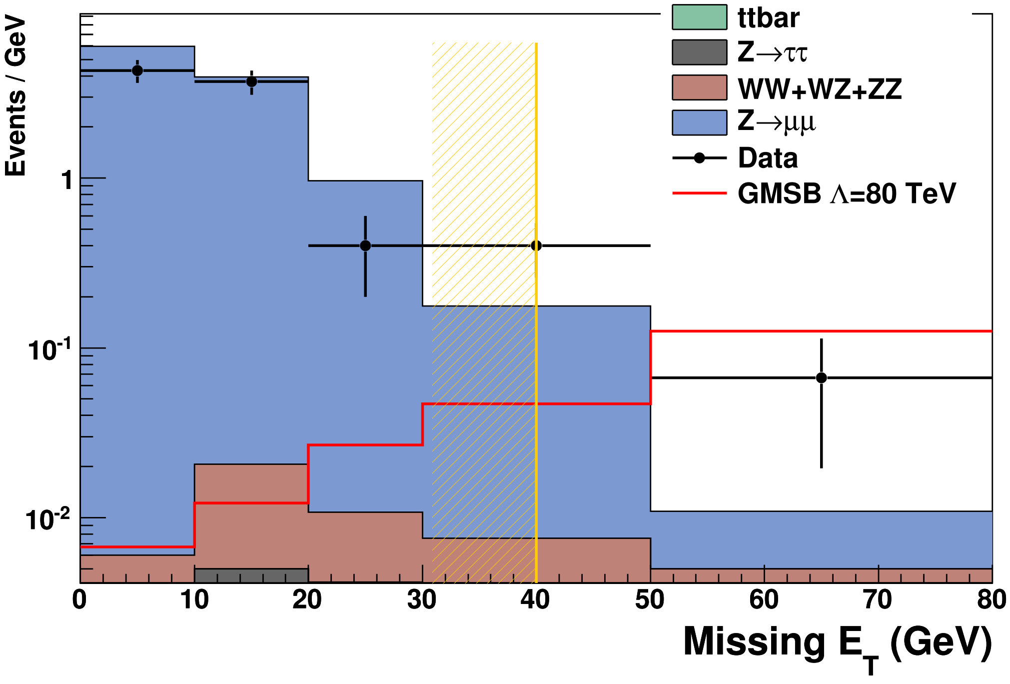

and Table 5.7 for the muons. This table is meant to illustrate the contributions from the various backgrounds as modeled by MC. There seems to be little evidence for a signal, at least in the electron channel. In Chapter 6 we will calculate constraints on the signal using more detailed information. In particular, the full $\not{E}_T$spectrum will be used in a likelihood comparison of background and background+signal to data. Some background events estimated from data will also be included; one is already shown in the *ee* Table 5.6, the contribution from QCD jet events.

Table 5.6: Cut flow for the *ee* channel. Values are the expected number of events predicted by each MC and the number of observed events in the "Data" column. Only statistical errors are shown. Percentages indicate the fraction of events accepted by each cut.

Cut	ttbar	Ztautau	Dibosons	QCD	Zee	MC Total	Data	GMSB080
	146.77 ± 0.81	1037.88 ± 24.98	484.19 ± 5.93	7607.13 ± 40.04	278781.44 ± 171.28	288057.42 ± 177.76	297623.00 ± 545.55	22.19 ± 0.36
$78 < M(ee) < 104$ GeV	22 %	4.9 %	59 %	19 %	90 %	88 %	88 %	65 %
	32.80 ± 0.39	51.09 ± 5.82	284.02 ± 3.66	1426.62 ± 15.63	250498.54 ± 160.77	252293.08 ± 161.68	261770.00 ± 511.63	14.37 ± 0.30
$p_T(\gamma) > 10$ GeV	0.58 %	0.23 %	0.48 %	0.26 %	0.22 %	0.22 %	0.22 %	42 %
	0.19 ± 0.03	0.12 ± 0.04	1.36 ± 0.17	3.78 ± 0.79	560.34 ± 7.66	565.79 ± 7.70	570.00 ± 23.87	6.04 ± 0.20
$100 < M(ee\gamma)$ GeV	97 %	75 %	85 %	91 %	77 %	78 %	73 %	1e+02 %
	0.18 ± 0.03	0.09 ± 0.03	1.16 ± 0.16	3.44 ± 0.75	433.84 ± 6.86	438.70 ± 6.90	418.00 ± 20.45	6.03 ± 0.20
$p_T(\gamma) > 30$ GeV	44 %	53 %	44 %	27 %	25 %	25 %	19 %	96 %
	0.08 ± 0.02	0.05 ± 0.03	0.51 ± 0.11	0.93 ± 0.37	109.45 ± 3.66	111.03 ± 3.68	78.00 ± 8.83	5.79 ± 0.19
$\not{E}_T > 30$ GeV	79 %	91 %	25 %	0 %	0.34 %	0.55 %	0 %	90 %
	0.06 ± 0.02	0.04 ± 0.03	0.13 ± 0.05	0.00 ± 0.00	0.38 ± 0.11	0.61 ± 0.13	0.00 ± 0.00	5.21 ± 0.18

Table 5.7: Cut flow for the $\mu\mu$ channel. Values are the expected number of events predicted by each MC and the number of observed events in the "Data" column. Only statistical errors are shown. Percentages indicate the fraction of events accepted by each cut.

Cut	ttbar	Ztautau	Dibosons	Zmm	MC Total	Data	GMSB080
	142.31 ± 0.74	1531.21 ± 31.00	506.07 ± 5.70	320782.57 ± 182.87	322962.16 ± 185.57	342601.00 ± 585.32	15.32 ± 0.30
$65 < M(\mu\mu) < 115$ GeV	41 %	17 %	69 %	90 %	90 %	89 %	86 %
	57.90 ± 0.47	260.71 ± 12.26	346.69 ± 4.17	289498.69 ± 168.86	290163.99 ± 169.36	306541.00 ± 553.66	13.22 ± 0.28
$\Delta\phi$ cuts, see Sec. 5.5.1	93 %	78 %	91 %	88 %	88 %	87 %	91 %
	54.07 ± 0.46	203.69 ± 10.96	314.64 ± 4.00	253563.21 ± 157.90	254135.60 ± 158.33	267667.00 ± 517.37	12.06 ± 0.26
$p_T(\gamma) > 10$ GeV	0.57 %	0.14 %	0.71 %	0.37 %	0.37 %	0.37 %	44 %
	0.31 ± 0.03	0.28 ± 0.13	2.23 ± 0.31	936.61 ± 9.36	939.43 ± 9.36	984.00 ± 31.37	5.32 ± 0.18
$100 < M(\mu\mu\gamma)$ GeV	85 %	57 %	67 %	50 %	50 %	45 %	99 %
	0.26 ± 0.03	0.16 ± 0.06	1.48 ± 0.21	467.83 ± 6.92	469.73 ± 6.92	447.00 ± 21.14	5.29 ± 0.18
$p_T(\gamma) > 30$ GeV	42 %	66 %	31 %	24 %	24 %	21 %	97 %
	0.11 ± 0.02	0.11 ± 0.05	0.46 ± 0.12	111.95 ± 3.56	112.63 ± 3.57	94.00 ± 9.70	5.15 ± 0.17
$\not{E}_T > 30$ GeV	79 %	8.1 %	20 %	1.2 %	1.4 %	4.3 %	82 %
	0.09 ± 0.02	0.01 ± 0.00	0.09 ± 0.04	1.36 ± 0.37	1.55 ± 0.38	4.00 ± 2.00	4.23 ± 0.16

In the $\mu\mu$ channel there is an excess of events in data. These are likely the result of the substantial tail on the muon momentum resolution. Consider the event displays for two highest $\not\!\!E_T$events displayed in Appendix 7. Figure 7.3 shows the event where $\not\!\!E_T = 60.1$, $p_T(\mu_1) = 136.1$, $p_T(\mu_2) = 17.9$, $p_T(\gamma) = 73.0$ GeV, $M(\mu^+\mu^-) = 108.4$, and $M(\mu^+\mu^-\gamma) = 250.2$ GeV. And Figure 7.4 shows the event where $\not\!\!E_T = 68.3$, $p_T(\mu_1) = 137.6$, $p_T(\mu_2) = 27.9$, $p_T(\gamma) = 81.7$ GeV, $M(\mu^+\mu^-) = 109.0$, and $M(\mu^+\mu^-\gamma) = 249.2$ GeV. This highest $\not\!\!E_T$event has the suspicious feature that the leading muon is oriented directly opposite the $\not\!\!E_T$and the di-muon mass is near the top of our mass cut window. This suggests the muon momentum was reconstructed too large inducing $\not\!\!E_T$to balance the error.

5.7 Background estimation with data

5.7.1 QCD faking $Z \to ee$

QCD multi-jet events do not resemble our signal in many ways but jets can have a significant probability of faking the signal of other objects, especially electrons or photons. Because the cross section of multi-jet events is orders of magnitude higher than inclusive $Z \to ee$ we must consider the possibility of multi-jet fakes where the kinematics are fortuitous enough to also satisfy the Z-mass constraint.

This background can be clearly seen in Figure 5.12 where there is an excess of data events in the low mass region. This is where you expect to observe background from fakes which lack a real invariant mass near the Z. Notice that a QCD background may contribute to a similar discrepancy in the $\mu\mu$ sample as seen in Figure 5.4, but the contribution is much less than for electrons. Estimating a signal such as this from MC is difficult because the action of a jet faking an electron is rare and anomalous and would at the very least require extremely large MC statistics.

We will use a data-driven process to estimate these jet events in our sample. The

Figure 5.12: The $Z \to ee$ MC compared to data without the QCD contribution included. The discrepancy at low mass will be used to estimate the QCD contribution to the background.

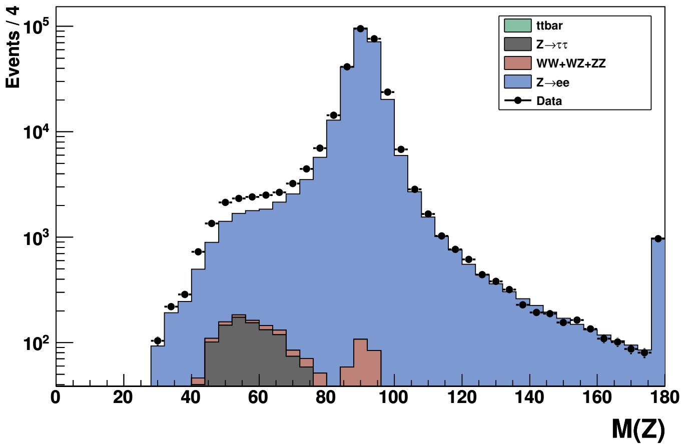

idea is form a QCD-rich sample of di-EM data by using a reversed cut on one of the EM object identification variables. The invariant mass spectrum for these events is then used as a template along with well understood MC such as $Z \to ee$ to fit the mass spectrum in data. The process is thus

1. Select events from data with at least two "preselected" EM objects ($0.9 <$ emfrac, isolation < 0.2)

2. Use events with a reversed quality cut on both

    - Here `isoHC4` > 4 GeV (track isolation) is used, but

    - a cut such as H-matrix > 40 (shower-shape) has been used in other analyses, this has the advantage of having less p_T dependence but requires a harder cut to reject real electrons.

3. In $p_T(e_1)$ and $p_T(e_2)$ bins use the resulting QCD rich spectrum along with Z+jet MC to fit the mass spectrum in data.

4. Uses `TFractionFitter`, part of ROOT, which is a likelihood fitter that accounts for data and MC statistics.

The results of these fits using bin edges at 15, 25, 35, and 45 GeV for $p_T(e_1)$ and $p_T(e_2)$ are shown in Figure 5.13. Beyond $p_T = 45$ GeV the MC fits well enough without background that the fitting errors dominate the results. These errors are about 34% and so we assign a conservative systematic of 40% for this channel's contribution.

5.7.2 Z+jets faking $Z\gamma$

There are two methods in common use at DØ to estimate Z+jet backgrounds where jet $\sim \gamma$.

1. *Matrix method* - count photon events after a preselection (N_1) and again after identification cuts (N_2). Then

$$\begin{pmatrix} N_1 \\ N_2 \end{pmatrix} = \begin{pmatrix} 1 & 1 \\ \epsilon_\gamma & \epsilon_{\text{jet}} \end{pmatrix} \begin{pmatrix} N_\gamma \\ N_{\text{jet}} \end{pmatrix}$$

   Use $Z\gamma$ or diphoton MC and EM-like jets in MC or data to estimate efficiencies ϵ_γ and ϵ_{jet}. The quantity we want to know is $N'_{\text{jet}} = \epsilon_{\text{jet}} N_{\text{jet}}$ which should sum with $N'_\gamma = \epsilon_\gamma N_\gamma$ to the total number of selected events, N_2.

2. *Template method* - Using preselected photon events in MC, and possibly data, compare the shape of a continuous discriminating variable such as the electron identification. Then use these shapes as templates to fit the distribution of that variable in data.

Both methods allow us to use data, at least at the preselection level, to estimate backgrounds. Both methods can be used and compared against each other. Here we use the matrix method, but the template method yields consistent values.

At the preselection level (N_1) we require EM clusters in CC which have EM fraction $> .9$, isolation < 0.15, and separated from any identified leptons. The core0 photon identification requirements are then added to find N_2.

Figure 5.13: Fitting a QCD rich background sample from a reversed `isoHC4` selection to the invariant mass spectrum of data in combination with Monte Carlo $Z(ee)$+jets. Since this isolation cut has a significant p_T dependence the fitting is done in bins of $p_T(e_1)$ and $p_T(e_2)$ with edges at 15, 25, 35, and 45 GeV.

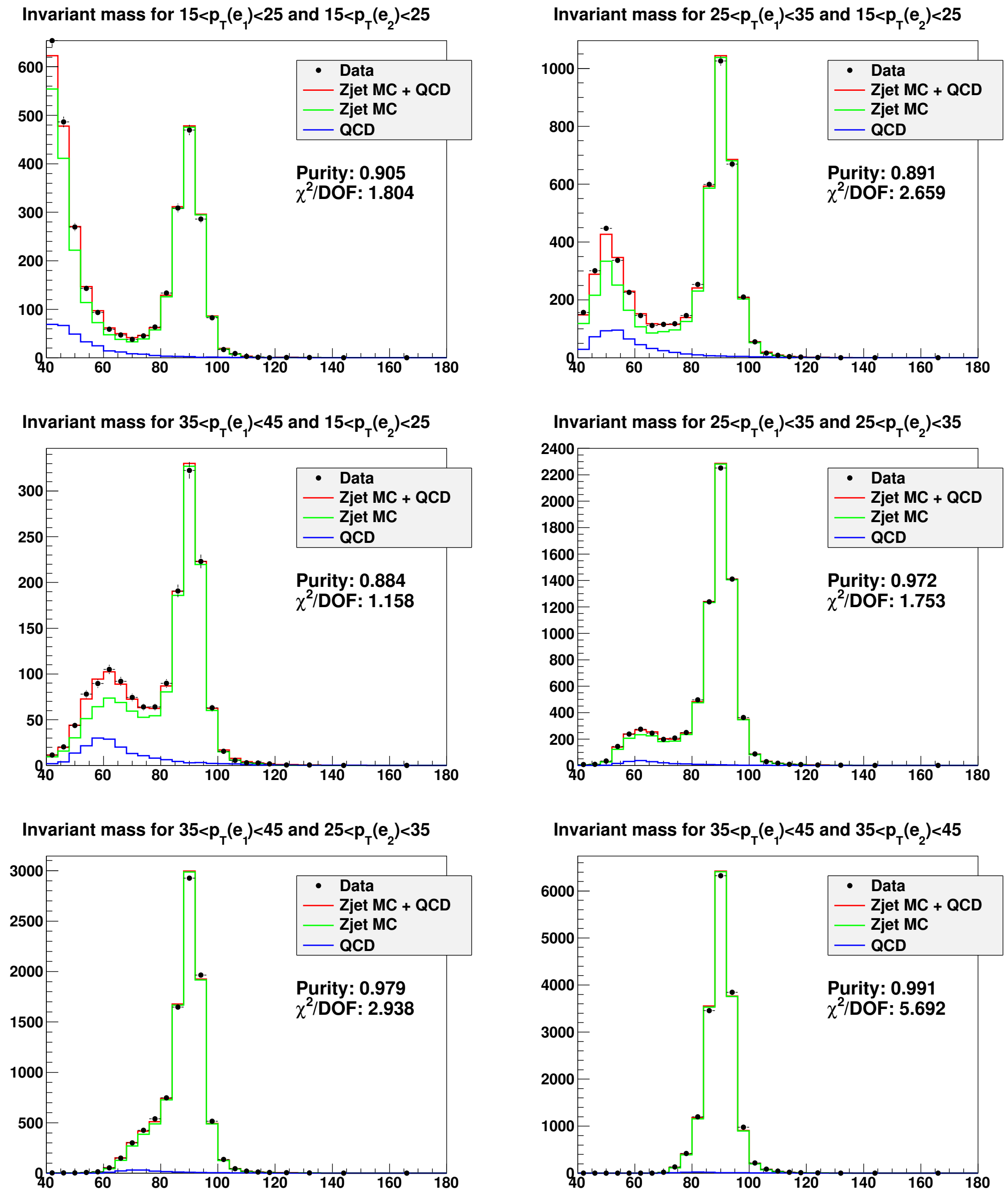

Figure 5.14: (a) Efficiency as a function of p_T and $|\eta|$ to identify a photon with the core0 selection in CC once it has passed preselection. (b) Efficiency as a function of instantaneous luminosity.

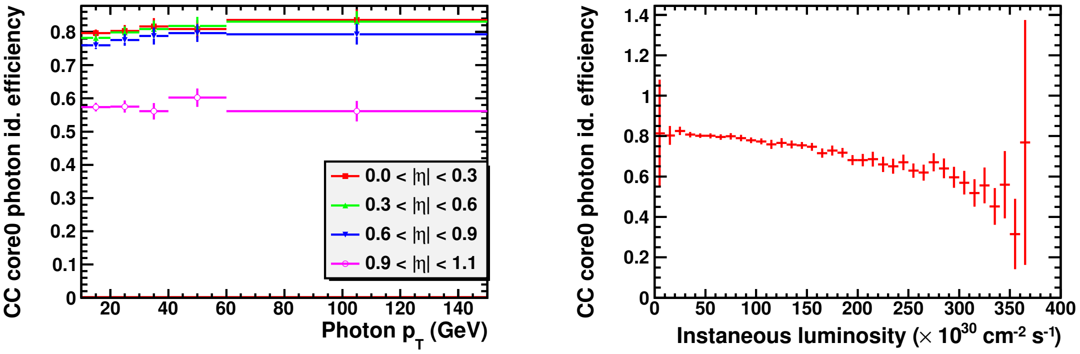

(a) (b)

We begin by estimating ϵ_γ from $Z(\mu\mu) + \gamma$ MC. The estimate of ϵ_γ is done in regions of p_T and $|\eta|$. Efficiencies rise slightly with p_T and drop with $|\eta|$, as seen in Figure 5.14(a). There is also some luminosity dependence as see in Figure 5.14(b), but the MC has been reweighted for instantaneous luminosity and matches data quite well so this will be left out of the estimate. This dependence is understandable because with increasing luminosity there are more uncorrelated tracks and energy deposits so the photon is less likely to pass isolation requirements.

Other analysis sometimes use data to make this estimate, but because $Z + \gamma$ is already quite background-free it is usually what is used as a source of high quality photons. In our case we are estimating a background to $Z + \gamma$, so MC is the best alternative.

To estimate ϵ_{jet} a QCD MC that has been filtered for EM-like jets is used. Because these events won't have the p_T or η spectrum of our signal it is especially important to bin in these variables; the results are shown in Figure 5.15. This fake EM signal does not have a strong instantaneous luminosity dependence.

Figure 5.15: Using a QCD MC sample filtered for EM-like jets, this is the efficiency as a function of p_T and $|\eta|$ to identify a photon with the core0 selection in CC once it has passed preselection.

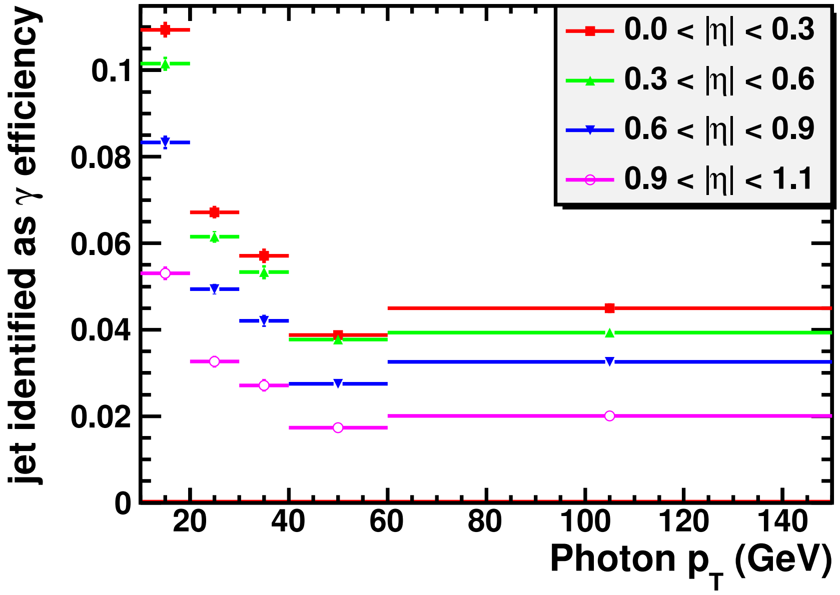

The breakdown of the selected events into photon-like jet fakes and true photon events is

$$N'_\gamma = \epsilon_\gamma \frac{N_2 - \epsilon_{\text{jet}} N_1}{\epsilon_\gamma - \epsilon_{\text{jet}}} \qquad N'_{\text{jet}} = \epsilon_{\text{jet}} \frac{\epsilon_\gamma N_1 - N_2}{\epsilon_\gamma - \epsilon_{\text{jet}}} \tag{5.2}$$

The algebra yielding this is simple, but for further discussion and references see [53] and the updated uncertainties in [54]. There are three uncertainties, the statistical uncertainty is completely anti-correlated and approximated by

$$\delta N'_\gamma = -\delta N'_{\text{jet}} = \sqrt{\frac{N'_\gamma N_{\text{jet}}}{N_2}}, \tag{5.3}$$

and propagating the uncertainty on the efficiencies yields

$$\delta N'_\gamma = -\delta N'_{\text{jet}} = -\epsilon_{\text{jet}} \frac{N_2 - \epsilon_{\text{jet}} N_1}{(\epsilon_\gamma - \epsilon_{\text{jet}})^2} \delta\epsilon_\gamma \tag{5.4}$$

Table 5.8: Estimate of jet to γ fake background in the $ee\gamma$ channel using the matrix method.

$p_T(\gamma)$ range	N signal	N background	Uncertainty
$30 < p_T < 40$	20.6	9.4	± 2.6
$40 < p_T < 60$	27.8	4.2	± 1.9
$60 < p_T < 150$	13.3	2.7	± 1.5
Total	61.7	16.3	± 3.5

Table 5.9: Estimate of jet to γ fake background in the $\mu\mu\gamma$ channel using the matrix method.

$p_T(\gamma)$ range	N signal	N background	Uncertainty
$30 < p_T < 40$	27.8	10.2	± 2.7
$40 < p_T < 60$	30.9	5.1	± 2.1
$60 < p_T < 150$	22.8	3.2	± 1.7
Total	81.5	18.5	± 3.8

$$\delta N'_{\gamma} = -\delta N'_{\text{jet}} = -\epsilon_{\gamma}\frac{\epsilon_{\gamma}N_1 - N_2}{(\epsilon_{\gamma} - \epsilon_{\text{jet}})^2}\delta\epsilon_{\text{jet}} \tag{5.5}$$

Using these values we find the total contribution from jet backgrounds is 16.3 ± 3.5 events in $ee\gamma$ and 18.5 ± 3.8 events from $\mu\mu\gamma$ with $p_T(\gamma) > 30$ GeV and before the $\not\!\!E_T$ cut. Details are displayed in Tables 5.8 and 5.9.

5.7.3 Using same-sign di-leptons

An additional method for estimating the background from processes such as QCD multijets or from W+jets is to look at events that pass all the same selection cuts but using same-sign leptons instead of the opposite signs always expected from a Z decay. There should be equal proportions of same and opposite sign lepton fakes so we expect the contribution of these background to contribute equally to the same-sign and opposite sign signals. But, the full same-sign sample could potentially be a large over-estimate of these backgrounds because the same-sign sample may be contaminated by true Z events where there was a charge misidentification.

The charge misidentification is small for muons. After the invariant mass and $\Delta\phi$ cuts but before requiring a photon there are 98 events in data with same-sign muons; comparing this to 268318 events with opposite sign, this is a 0.04 % contribution. There are no same-sign events passing the $p_T(\gamma) > 10$ requirement.

For electrons the raw numbers are higher: 12046 same-sign events and 262085 opposite sign events after the invariant mass cut for a ratio of 4.6%. After $p_T(\gamma) > 10$ GeV and $M(ee\gamma) > 100$ GeV there are 16 same-sign and 420 opposite sign, a similar fraction of 3.81%. The result of electron charge misidentification studies is that it is about 0.44% in CC and 6.4% in the EC [55]. Given that our $Z \rightarrow e^+e^-$ events are split 66%/34% between the CC-CC and the CC-EC combinations we expect same-sign from Z at the rate of

$$2 \cdot 0.0044(1-0.0044) \cdot 0.066 + 0.044(1-0.064) \cdot 0.34 + 0.064(1-0.0044) \cdot 0.34 = 4.1\% \tag{5.6}$$

With the same-sign fraction between 4.6 and 3.8% this result is consistent with the $\approx 1\%$ estimate for the QCD background in Table 5.6 from fitting the excess data at low invariant mass.

5.8 Systematic uncertainties

We assign the standard systematic uncertainty on DØ luminosity of 6.1%. The PDF uncertainty is estimated as 4%. The muon identification systematics include three contributions 1.0% for the reconstruction, 1.1% for tracking efficiency, and 0.5% for isolation. The electron uncertainty is $\approx 1\%$ in the CC region but is as high as 3-4% in the extreme forward region, here we use 2%. The cross section uncertainties for Z+jets, dibosons, and $t\bar{t}$ are 6, 6, and 10%, respectively. Fit errors for the high p_T portion of the QCD estimation are as high as 38%, so we assign a conservative estimate of 50% to QCD. A summary of the values and references are enumerated in

Table 5.10: Contributions to the uncertainty in the number of background events expected for the $ee\gamma$ and $\mu\mu\gamma$ channels.

Quantity	Uncertainty RunIIb
Trigger	2 %
Muon identification	1.6 % / muon [35]
Electron identification	2 % / electron [51]
Photon identification	2.7 % [52]
Luminosity	6.1 % [56]
W/Z+jets cross-section	6 % [48]
$t\bar{t}$ cross-section	10 % [57]
Diboson cross-section	6 % [58]
QCD	40 %
PDF	4 %

Table 5.10.

5.9 Boosted Decision Tree selection

Though our signal is generally characterized by high p_T photons and large missing energy, as in any event selection process, there are many additional features that may remain unexploited. Multivariate techniques such as likelihood, H-matrix, artificial neural networks (ANNs), and boosted decision treess (BDTs) aim to exploit these features in a somewhat automated way. Common to all is an initial stage where the event selector is *trained* to separate signal from background. Training uses MC signal and background along with additional background estimates that may come from data to prepare the selection process. The selection process is then tested on an independent set of signal and background events to estimate it's signal efficiency and background rejection rate. Typically the output of one of these algorithms is a single variable which takes high values for signal and low values for background.

Of course there are relative merits to each algorithm. Features that may be important include the speed of training, speed of testing, robustness to the specific set

Figure 5.16: Illustration of decision trees and boosting. Each cell shows the number of signal and background events, and branching corresponds to a cut on a single variable. Cuts are chosen to maximize a weighted purity. From one tree to the next the misclassified events (signal events in a background leaf and background events in a single leaf) are given higher weight with the boosting algorithm.

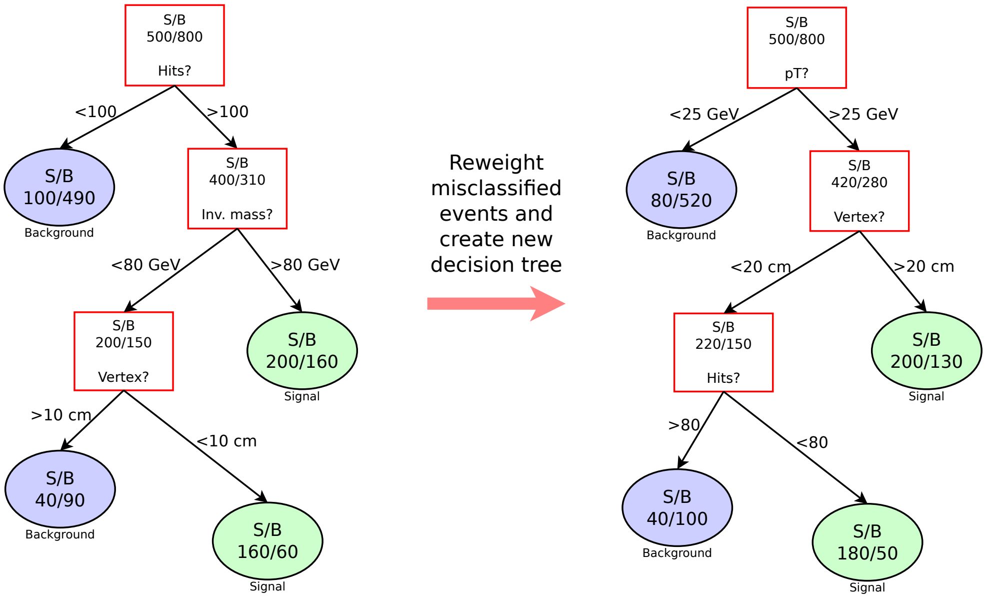

of variables choosen, robustness to overtraining, behaviour when the variables are strongly correlated, auxillary information you can derive from training, and technical knowledge necessary to use sucessfully. The BDT technique has become a very popular technique in recent years [59, 60, 61]. It behaves well with respect to speed and over-training even when many variables are used. As a byproduct of the training process it can provide a ranking of which variables are most important.

The fundamental unit of a BDTs is a decision tree. A decision tree is a branching sequence of simple cuts, each on a single variable, that leads to a final decision at a leaf of the tree. In our case the decision is whether a particular event is signal or background. A decision tree is illustrated in Figure 5.16.

A decision tree is trained by looking over a pool of events labeled either signal or background and selecting the cut on a single variable that separates the signal and background into the most pure samples. The tree branches and the selection is repeated for each of the the two sub-samples. A stopping criterion such as high purity or few events is used to end the splitting process; at this point every event has been filtered into a signal or background leaf.

The decision tree becomes more robust and efficient by using it in combination with many other trees, called a forest. Trees are trained in succession and misclassified events (signal events that end up in background leaves, or vise-versa) are given larger weight when the next tree is trained; This weighting makes the even more likely to be correctly classified in later trees. This process is called boosting. Typically a forest may have several hundred to a few thousand decision trees.

When using the BDT forest to identify an event the event is tested on each one of the trees. Trees that identify it as signal contribute +1 and those that identify it as background contribute -1 to a sum that is the BDT output. Additionally there may be a weight of applied to the ±1 score for each tree.

A preselection was applied before training and selection. We use the same object identification as already described with the photon separated from the leptons and jets by $\Delta R > .7$. Additionally we require

$$M(\ell\ell) > 70 \text{ GeV} \qquad p_T(\gamma) > 15 \text{ GeV} \qquad \not{E}_T > 15 \text{ GeV} \tag{5.7}$$

There are significantly different issues for the two lepton types: muons have a wide momentum resolution with a substantial tail whereas electrons suffer more from confusion with photons and jets. Therefore, we trained BDTs separately for the $ee\gamma$ and $\mu\mu\gamma$ channels. One advantage to BDT selection is that it is efficient and stable even when applied to many selection variables; thus we began our training with more than 100 variables including identification variables for the leptons and photon, invariant masses, momentum sums and differences, angle differences, etc.

The training process yields a ranking for the variables that is used to select the 30 most important. Comparisons between data and MC were inspected for all of these 30 variables; any that showed poor MC modeling in the inclusive $\ell\ell\gamma$ ($p_T(\gamma) > 10$ GeV) distributions were removed. From this we ended up with a list of 21 variables for the $ee\gamma$ channel and 25 variables for the $\mu\mu\gamma$ channel which have distributions displayed in Figures 5.17-5.19 and Figures 5.20-5.23, respectively.

The variables for the $ee\gamma$ channel are

1. $M_T(\gamma_1, \not{E})$
2. Missing E_T
3. Leading photon core energy for isolation (GeV)
4. Leading photon p_T
5. $\Delta R(l_1, l_2)$
6. Missing energy signficance
7. $M(Z)$
8. Missing energy parallel to Z
9. $M_T(l_2, \not{E})$
10. $p_T(l_2) - \not{E}_T$
11. Angle between l_1 and l_2
12. Leading jet p_T
13. $p_T(Z + \gamma_1)$
14. $M(l_2 + \gamma_1)$
15. Missing energy transverse to Z
16. $p_T(l_2 + \gamma_1)$
17. Leading photon calo. isolation, $(E_{total}(.4) - E_{EM}(.2))/E_{EM}(.2)$
18. $M(l_{\text{nearest}} + \gamma_1)$
19. $M_T(l_{\text{nearest}}, \not{E})$
20. $M_T(l_1, \not{E})$
21. $M_T(j_2, \not{E})$

and the variables for the $\mu\mu\gamma$ channel are

1. $M_T(\gamma_1, \not{E})$
2. $p_T(l_2) - p_T(\gamma_1)$
3. Leading photon core energy for isolation

4. $p_T(l_2) - \not{E}_T$
5. Leading photon p_T
6. $M_T(l_2, \not{E})$
7. ϕ angle between Z and γ_1
8. $\eta(Z)$
9. $\eta(Z + \gamma_1)$
10. $M_T(l_1, \not{E})$
11. Angle between Z and γ_1
12. $\Delta R(l_1, l_2)$
13. $p_T(l_{\text{nearest}}) - \not{E}_T$
14. Leading muon η
15. Leading muon ΔR distance to nearest jet reconstructed with 0.5 cone algorithm
16. $p_T(Z + \gamma_1)$
17. $M(l_2 + \gamma_1)$
18. Leading jet p_T
19. Leading photon calo. isolation, $(E_{total}(.4) - E_{EM}(.2))/E_{EM}(.2)$
20. $M(l_1 + \gamma_1)$
21. $M_T(j_{\text{nearest}}, \not{E})$
22. $M(l_{\text{nearest}} + \gamma_1)$
23. Second muon ΔR distance to nearest jet reconstructed with 0.5 cone algorithm
24. Angle between l_1 and l_2
25. $\Delta R(Z, \gamma_1)$

It might be surprising that the p_T difference variables but at least variables such as $p_T(l_2) - \not{E}_T$ make very good sense. If the the lower muon is undermeasured then the $\not{E}_T$ will increase; these two things balance in the difference. Events with true $\not{E}_T$ not not from the μ_2 undermeasurement will have a large negative value of this difference.

Finally, the distribution of background events and signal at two Λ scales are shown in Figure 5.24.

Figure 5.17: Variables 1-8 used for BDT selection in the $ee\gamma$ channel in order of importance as ranked by the BDT training. The standard e^+e^- selection, $M(ee) > 70$ GeV, and $p_T(\gamma) > 10$ GeV have been applied.

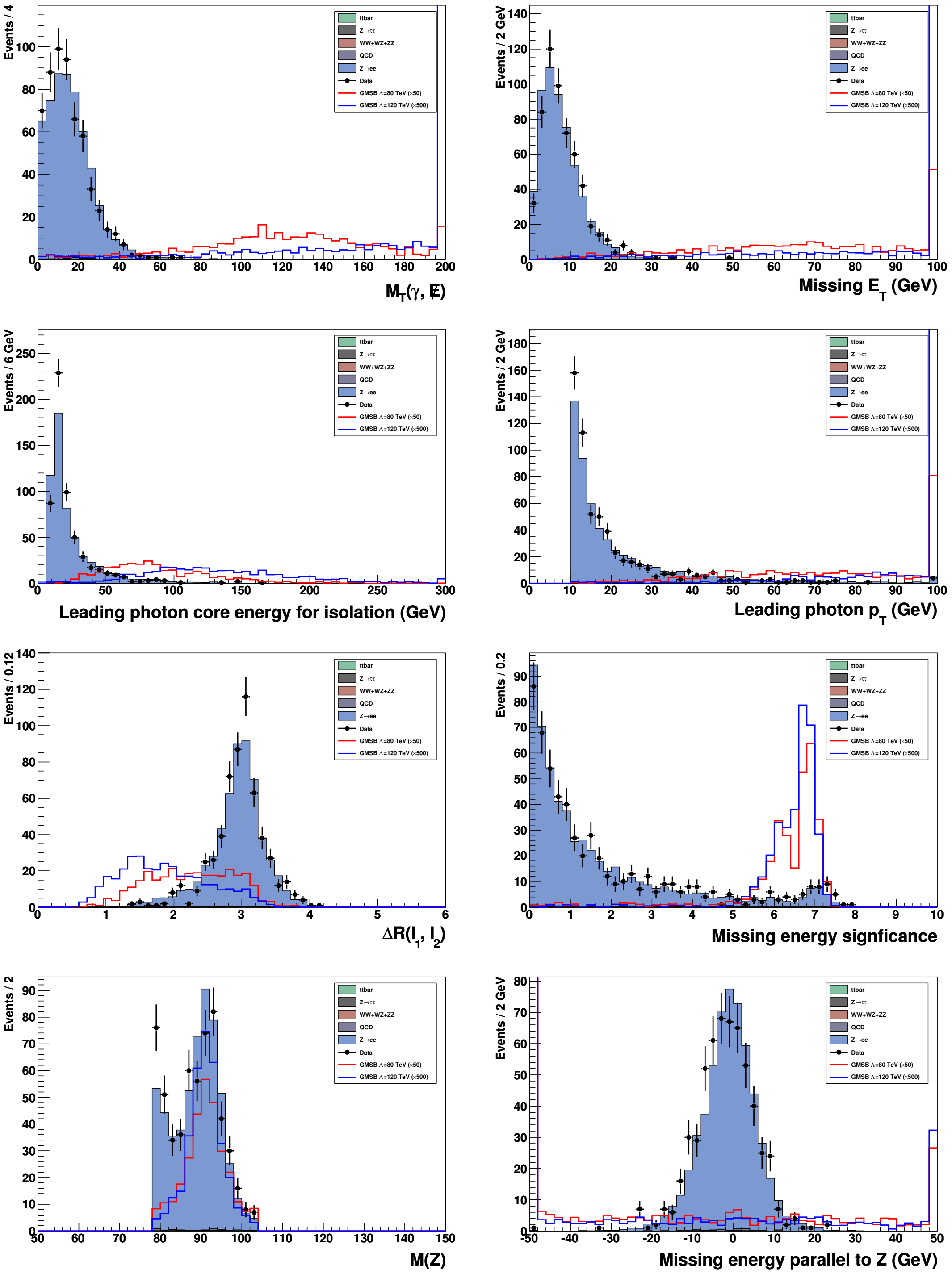

Figure 5.18: Variables 9-16 used for BDT selection in the $ee\gamma$ channel in order of importance as ranked by the BDT training. The standard e^+e^- selection, $M(ee) > 70$ GeV, and $p_T(\gamma) > 10$ GeV have been applied.

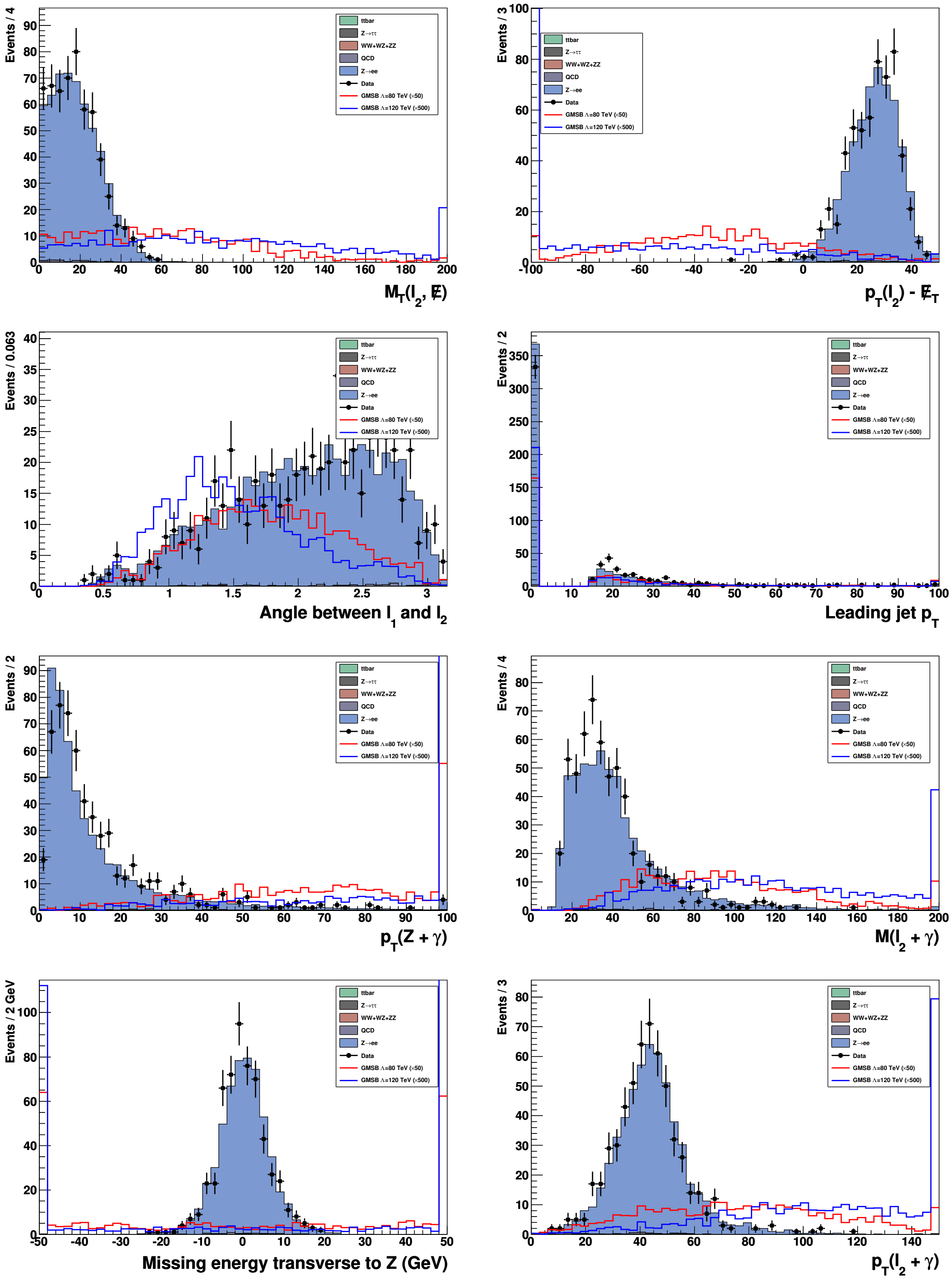

Figure 5.19: Variables 17-21 used for BDT selection in the $ee\gamma$ channel in order of importance as ranked by the BDT training. The standard e^+e^- selection, $M(ee) > 70$ GeV, and $p_T(\gamma) > 10$ GeV have been applied.

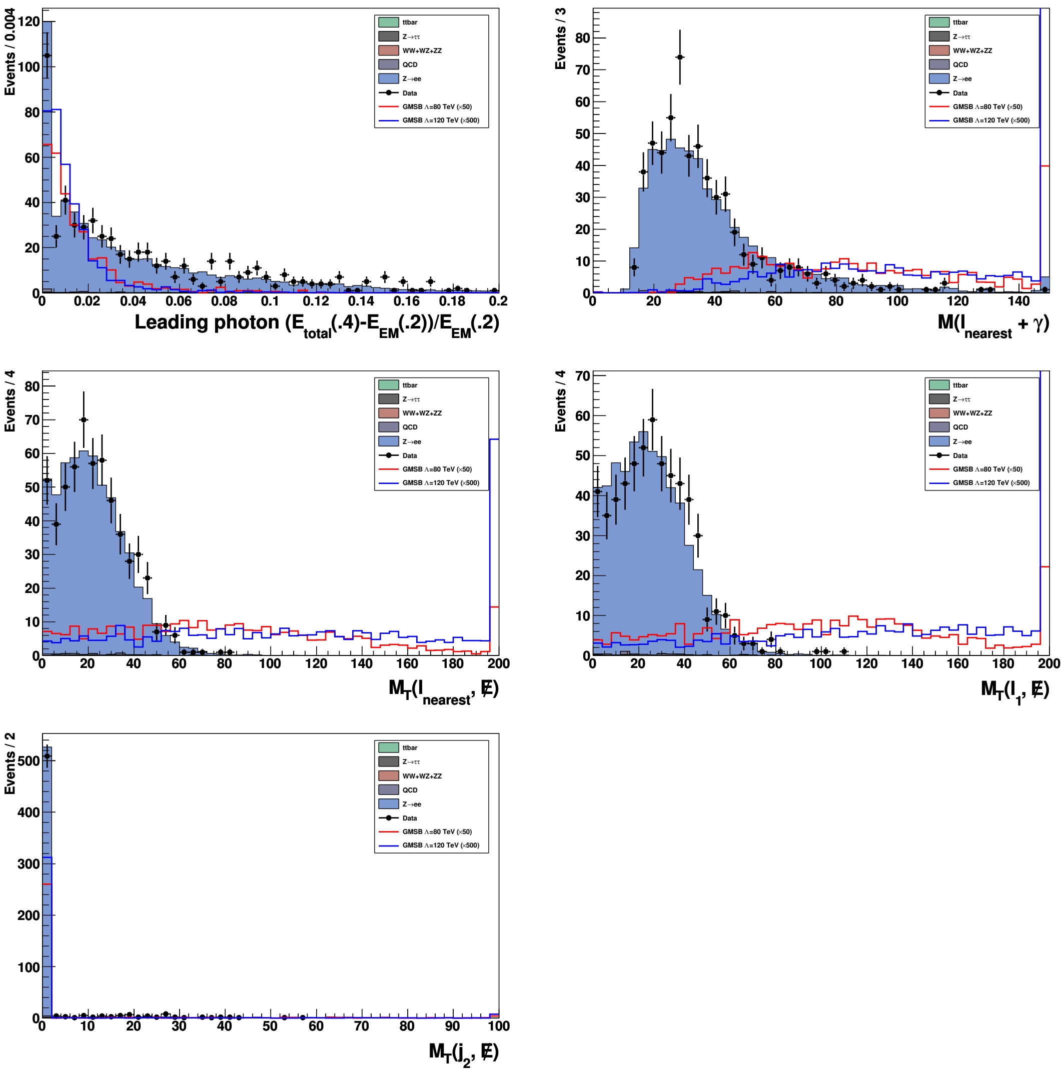

Figure 5.20: Variables 1-8 used for BDT selection in the $\mu\mu\gamma$ channel in order of importance as ranked by the BDT training. The standard $\mu^+\mu^-$ selection, $M(\mu\mu) > 70$ GeV, and $p_T(\gamma) > 10$ GeV have been applied.

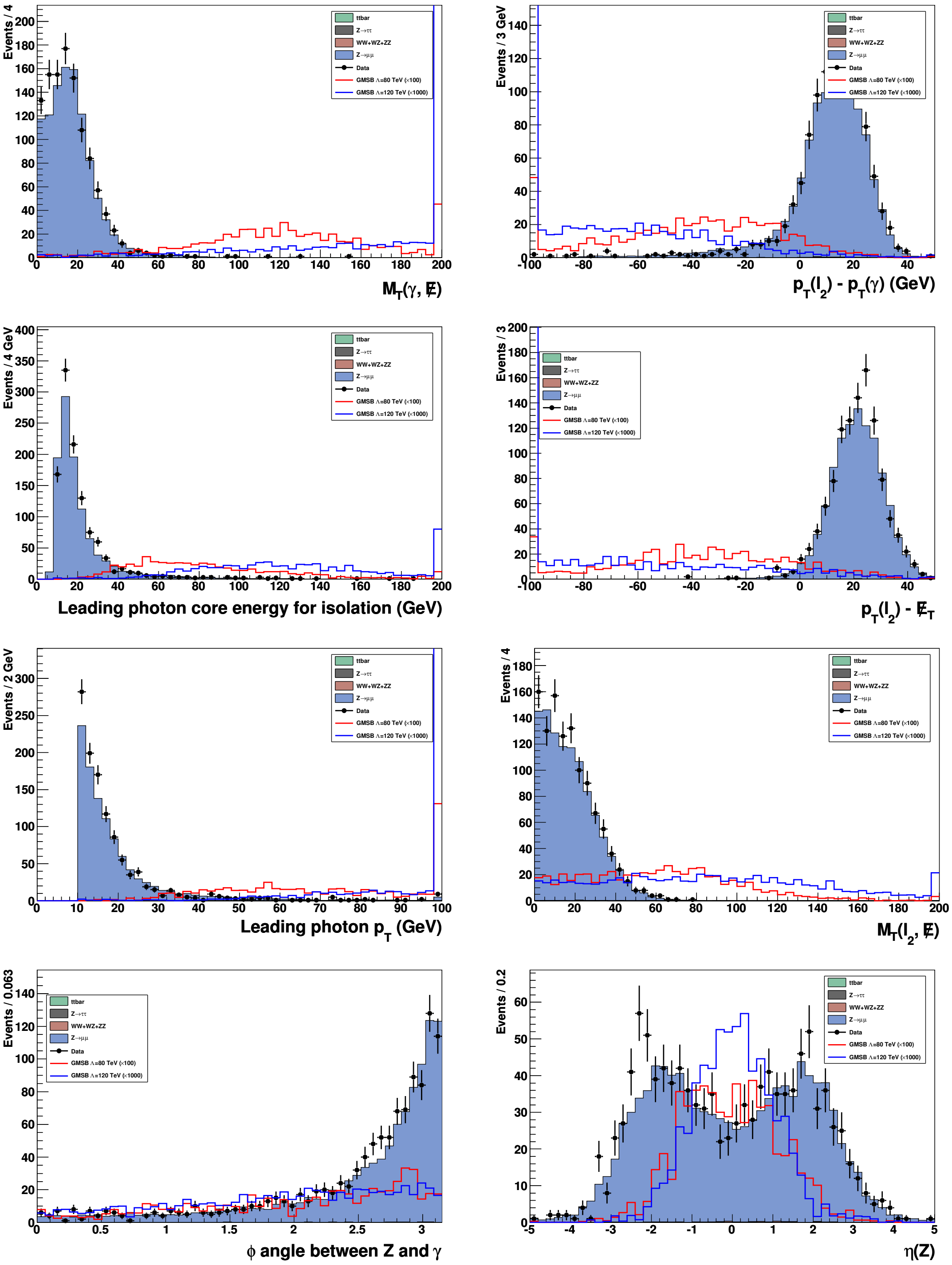

Figure 5.21: Variables 9-16 used for BDT selection in the $\mu\mu\gamma$ channel in order of importance as ranked by the BDT training. The standard $\mu^+\mu^-$ selection, $M(\mu\mu) >$ 70 GeV, and $p_T(\gamma) > 10$ GeV have been applied.

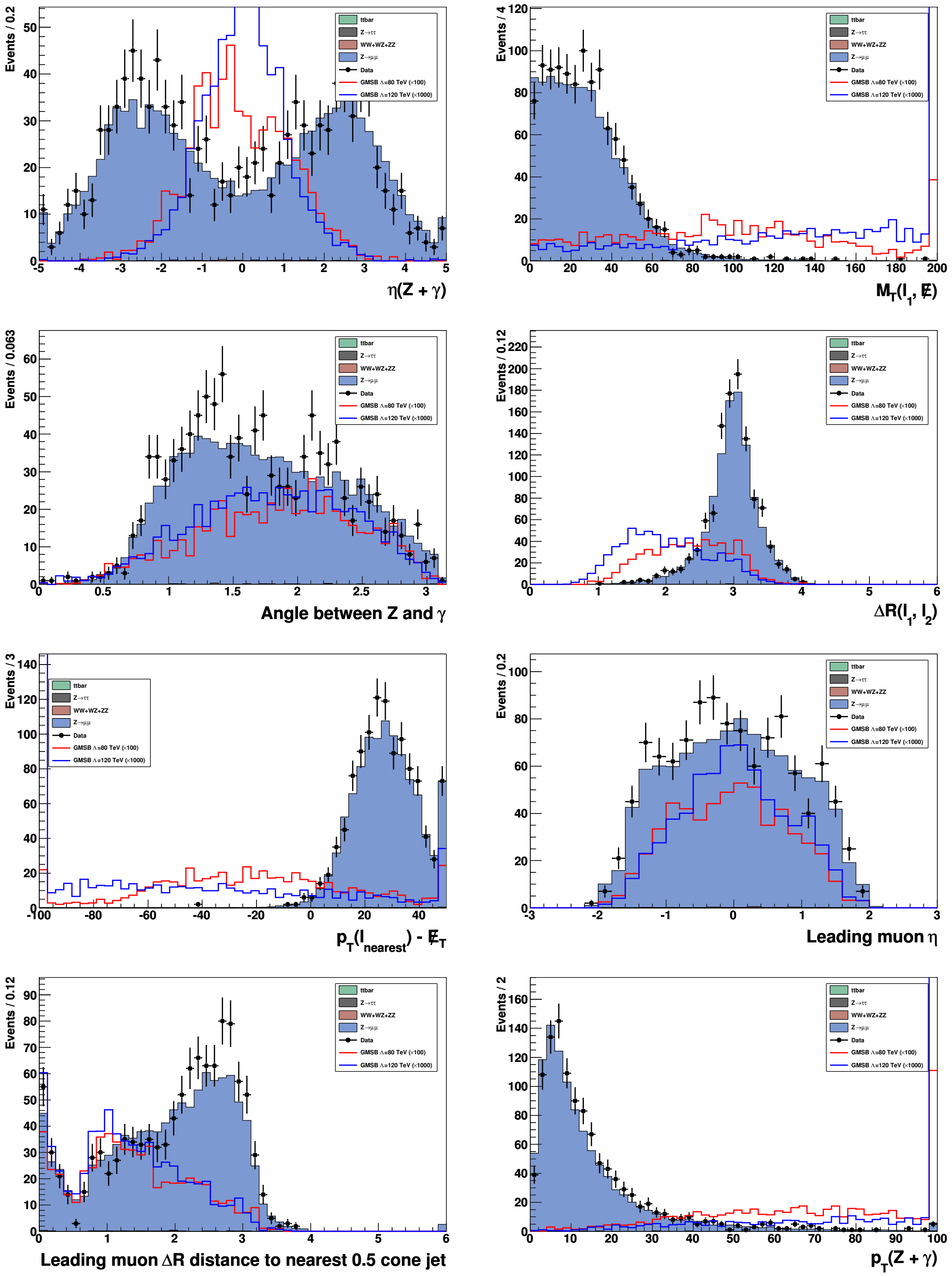

Figure 5.22: Variables 17-24 used for BDT selection in the $\mu\mu\gamma$ channel in order of importance as ranked by the BDT training. The standard $\mu^+\mu^-$ selection, $M(\mu\mu) >$ 70 GeV, and $p_T(\gamma) > 10$ GeV have been applied.

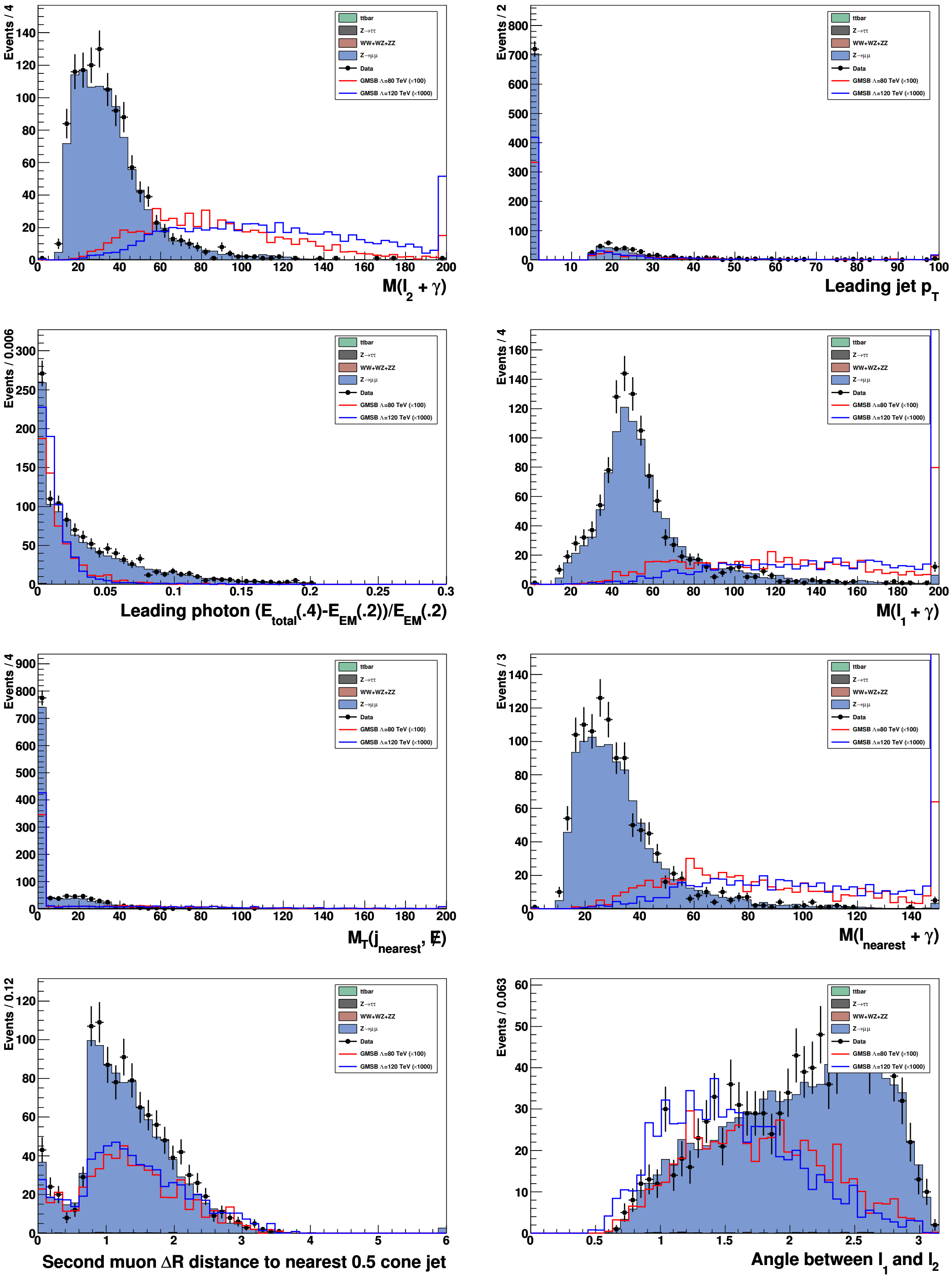

Figure 5.23: Variable 25 used for BDT selection in the $\mu\mu\gamma$ channel in order of importance as ranked by the BDT training. The standard $\mu^+\mu^-$ selection, $M(\mu\mu) >$ 70 GeV, and $p_T(\gamma) > 10$ GeV have been applied.

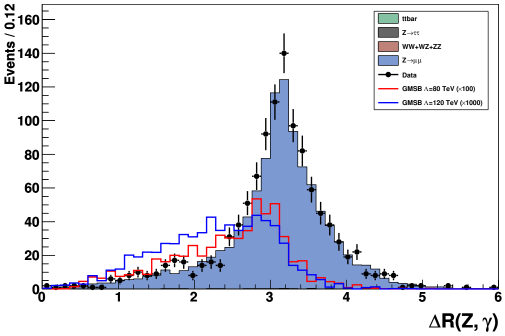

Figure 5.24: Distributions of the BDT selection variable for the ee channel on the left and the $\mu\mu$ channel on the right. The top plots show the signal with scale $\Lambda = 85$ TeV, and the bottom plots show the same backgrounds but with $\Lambda = 120$ TeV signal.

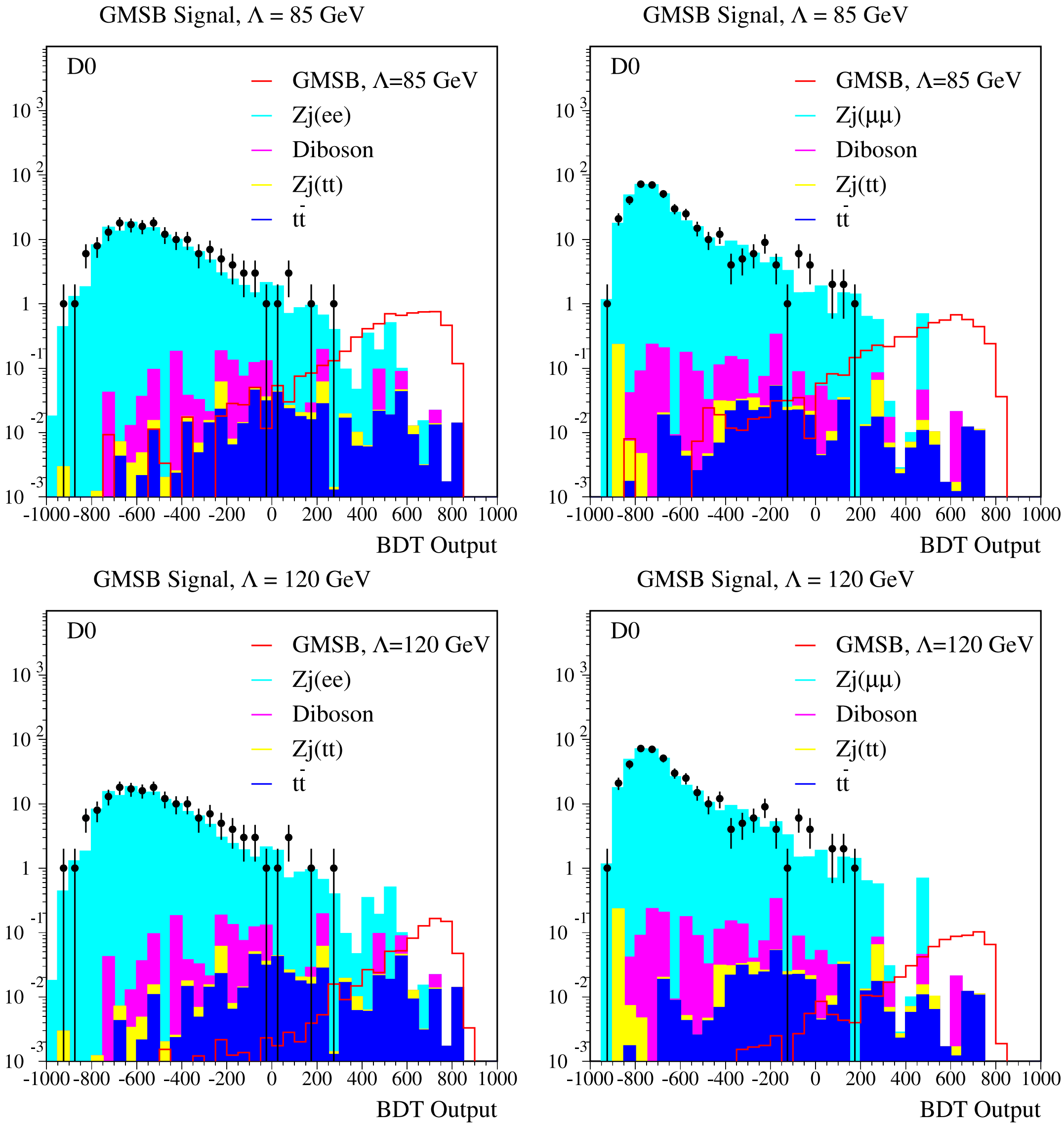

CHAPTER 6

Constraints on GMSB

6.1 Limit setting

Given the lack of significant signal we proceed to determining a region of parameter space where we can exclude the signal. In high energy physics (HEP) the standard of confidence for an exclusion interval is 95%, which corresponds to

The limit setting computation is accomplished using the COLLIE software. COLLIE takes as input histograms for the expected signal, all backgrounds, and the data. Each bin of each sample can have a statistical uncertainty and a number of systematic uncertainties. Systematic uncertainties may be specified per bin or as an overal percentage, they also may be uncorrelated (the cross section uncertainties of each MC process, for example) or correlated across samples (the luminosity uncertainty, for example).

The test statistic is formed by considering the Poisson likelihood ratio

$$Q = \frac{e^{-(s+b)}(s+b)^d/d!}{e^{-b}b^d/d!} = e^{-s}\left(1+\frac{s}{b}\right)^d \tag{6.1}$$

where s, b, and d are the numbers of signal, background, and data events, respectively. A joint likelihood for all channels and bins is created by taking a simple product and to recast into a somewhat more useful form we consider the negative log-likelihood

Figure 6.1: The distribution of $\not\!\!E_T$ after selecting for $p_T(\gamma) > 20$ GeV used in the limit setting. The red line is the background estimate, and the blue line is a scaled $\Lambda = 80$ TeV signal. At left is the $ee\gamma$ channel and at right is the $\mu\mu\gamma$ channel.

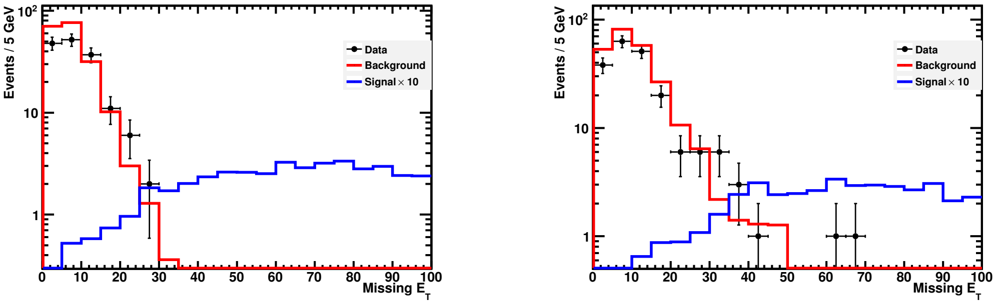
$ee\gamma$

$\mu\mu\gamma$

ratio (NLLR),

$$\begin{aligned}\text{NLLR} &= -2\log \prod^{\text{channels}} \prod^{\text{bins}} Q \\ &= 2 \sum^{\text{channels}} \sum^{\text{bins}} \left(s - d\log\left(1 + s/b\right)\right)\end{aligned}$$

The maximum likelihood occurs at the minimum NLLR and for large statistics this quantity approaches the Gaussian χ^2 value.

6.2 Simple cut results

For limit setting the same cuts as in Chapter 5 were used except that the photon selection was loosened to $p_T(\gamma) > 20$ GeV and signal, background, and data was binned in $\not\!\!E_T$ from 0 to 100 GeV. Distributions of $\not\!\!E_T$ for data, background, and $\Lambda = 80$ TeV signal are shown in Figure 6.1.

The resulting 95% confidence limits on a GMSB model line E signal cross section are shown in Figures 6.2 and 6.3. The solid line is the observed limit from data and the dashed line is the expected limit. The green and yellow contours are the 1 and 2-sigma deviations from the expected limit. That the solid line lies within the

Figure 6.2: 95% confidence limit on the cross section of GMSB production in model line E as a fraction of the theoretical value from Isajet. The result is a function of the Λ scale and is shown on the left for the $ee\gamma$ channel and on the right for the $\mu\mu\gamma$ channel.

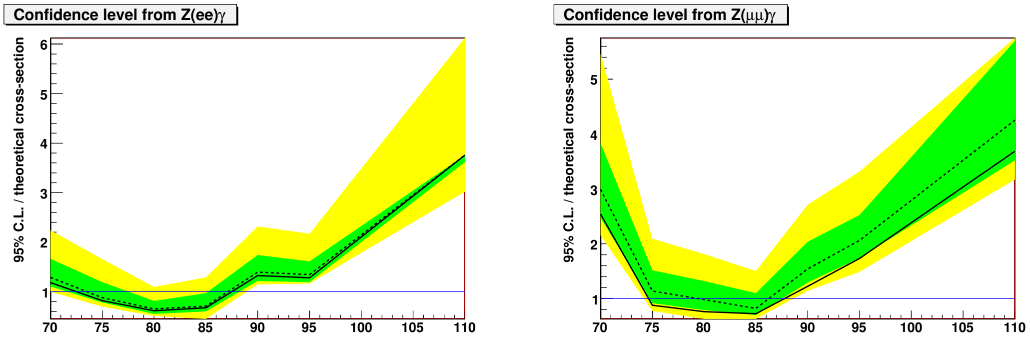

green band suggests that the data is well modeled by the background alone. The cross section limit is given as a fraction of the cross section estimated by Isajet, so Λ values where the solid line drops below 1 are excluded with 95% confidence.

The result of this simple cut analysis is that the region $70 < \Lambda < 97$ TeV is excluded with 95% confidence. This corresponds to $111 < M(\tilde{\chi}_1^0) < 176$ GeV.

6.3 Boosted decision tree results

Now we apply the more powerful BDT selection process to set limits on this GMSB model. In this case we use the same preselected events as described in the BDT Section 5.9, and binning is done in BDT scores from -400 to 800 as seen in Figure 6.4. The resulting limits from the $ee\gamma$, $\mu\mu\gamma$, and the two channels combined are shown in Figures 6.5 and 6.6.

Using BDT selection the 95% confidence region where the model is excluded expands to $70 < \Lambda < 117.5$ TeV. This corresponds to $111 < M(\tilde{\chi}_1^0) < 222$ GeV.

Figure 6.3: 95% confidence limit on the cross section of GMSB production in model line E as a fraction of the theoretical value from ISAJET. This is the result of combining the results from the $ee\gamma$ and $\mu\mu\gamma$ channels.

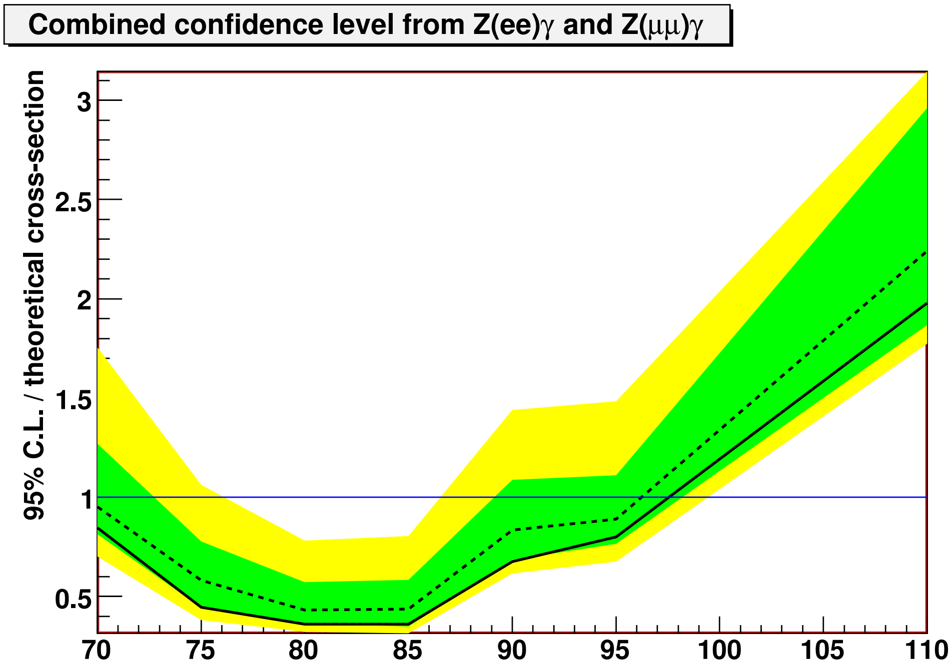

Figure 6.4: Distributions of signal and background BDT output used for the log likelihood limit setting. This signal is using $\Lambda = 85$ TeV. At left is the $ee\gamma$ channel, and at right the $\mu\mu\gamma$ channel.

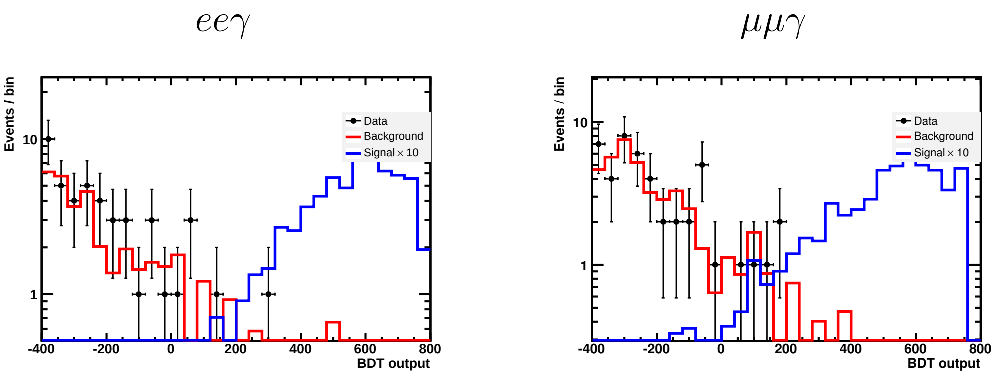
$ee\gamma$

$\mu\mu\gamma$

Figure 6.5: 95% confidence limit on the cross section of GMSB production in model line E as a fraction of the theoretical value from Isajet. Here BDT selection is employed on the $ee\gamma$ channel at left and the $\mu\mu\gamma$ channel at right.

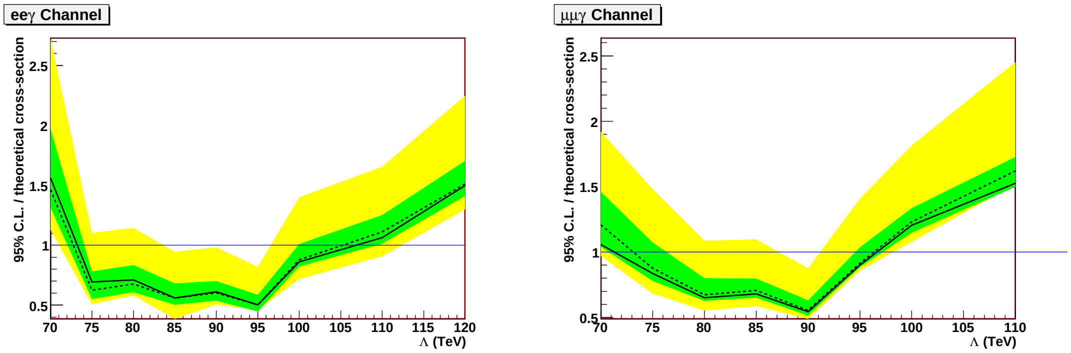

Figure 6.6: 95% confidence limit on the cross section of GMSB production in model line E as a fraction of the theoretical value from Isajet. This is the result of combining the results from the $ee\gamma$ and $\mu\mu\gamma$ channels using BDT selection.

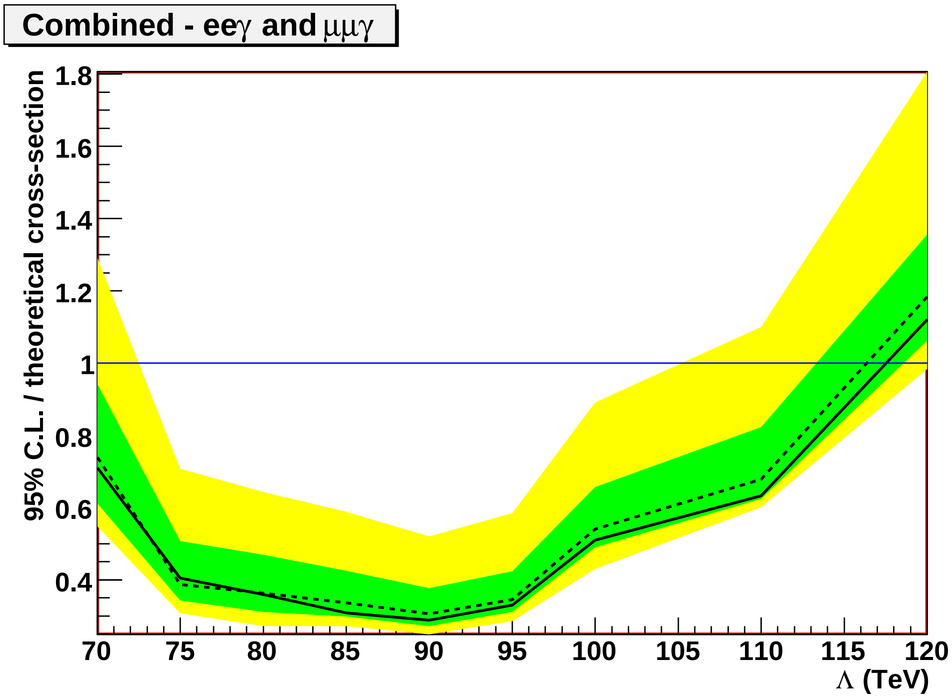

CHAPTER 7

Summary and Conclusions

This thesis details a search for a supersymmetry (SUSY) signature conducted with events containing $Z\gamma$ and large missing transverse energy in the DØ experiment at Fermilab's Tevatron accelerator with $p\bar{p}$ collisions at center of mass energy 1.96 GeV. The data used in the analysis was collected by the DØ experiment from June 2006 to July 2010 with a total integrated luminosity of 6.2 fb^{-1}. During this period the Tevatron accelerator has run extremely well producing peak luminosity of 4×10^{32} cm^{-2} s^{-1}, exceding the designed value. The DØ experiment has been fully functional with data taking efficiency larger than 90%. More than a million $Z \to \ell^+\ell^-$ events are detected and used in this analysis. The inclusive Z events are triggered by the high p_T lepton triggers with efficiency close to 100%.

This thesis is a pioneering work at the DØ experiment to search for a SUSY experimental signature in events containing $Z\gamma$ plus large missing E_T. Two Z decay channels are considered in the analysis, $Z \to e^+e^-$ and $Z \to \mu^+\mu^-$. This experimental signature is predicted by the gauge-mediated supersymmetry breaking (GMSB) model in the process

$$p\bar{p} \to \tilde{\chi}_1^0\tilde{\chi}_1^0 \to Z\tilde{G}\gamma\tilde{G} \quad (Z \to \ell^+\ell^-).$$

As can be seen in this process the experimental supersymmetry signature would be two isolated leptons from the Z decay, an isolated photon, and large missing transverse energy due to the two gravitinos ($\tilde{G}$) escaping detection.

The event selection criteria includes two isolated leptons with $p_T > 15$ GeV and requiring one with $p_T > 25(20)$ GeV for electrons (muons). The invariant mass of the dilepton must be within the Z mass window consistent with the detected mass resolution ($\pm 3\sigma$). An isolated photon with $E_T > 30$ GeV and well separated from the two leptons is required. The three-body invariant mass $M(\ell\ell\gamma)$ must be larger than 100 GeV to reject final state radiation events. The standard model production of $Z\gamma$ is used as a control sample for detector efficiency determination and normalization. The standard model events are modeled by fully simulated Monte Carlo (MC) events. It is found that data is consistent with MC predictions to 1% for inclusive Z events, which demonstrates a good understanding of lepton and photon detection with the DØ experiment.

Supersymmetry is searched for in the signal regions where missing E_T is larger than 30 GeV for the electron channel and 40 GeV for the muon channel. The missing E_T resolution and modeling is also checked with inclusive Z events. Data and MC are found to be consistent. The background in the signal region is expected to be very small. It is checked by MC simulations and estimated using data driven methods.

The predicted number of events from the supersymmetric model for $\Lambda = 80$ TeV is 5.2 ± 0.18 in the electron channel and 4.23 ± 0.16 in the muon channel, where Λ is the supersymmetry breaking scale in the model.

In data no event is observed in the electron channel with an expected standard model background of 0.61 ± 0.13. In the muon channel 3 events are observed with an expected standard model background of 1.55 ± 0.38.

We conclude that the observed data is consistent with the standard model prediction, no evidence for a supersymmetric signal is found. By combining the analysis results from both electron and muon channels we exclude the GMSB model at 95% confidence level for $70 < \Lambda < 117.5$ TeV, which corresponds to neutralino masses of

$111 < \tilde{\chi}_1^0 < 222$ GeV.

Similar searches will be continued at the Large Hadron Collider (LHC) where the center of mass energy will be 3.5 to 7 times larger than the current Tevatron energy. With *pp* collisions at 14 TeV the production cross section of our model is enhanced by a factor greater than 32 in the for $\Lambda \geq 120$ TeV region beyond the limit derived here. There remains great potential—with sufficient energies and intergrated luminosity—to discover supersymmetry at scales just out of reach of this work.

APPENDIX

Event Displays

This appendix provides figures describing specific events with high photon p_T and $\not{E}_T$ coming from data and the GMSB signal MC. All the figures are made up of four panels. The *top left* plot is a "LEGO" plot showing the η and ϕ directions unrolled onto a plne. Bars indicate calorimeter energy deposits ($>$ .5 GeV) overlayed with identified muons (green), EM clusters (brown, either an electron or a photon), and the $\not{E}_T$ (yellow, always at $\eta = 0$). The *top right* plot shows the tracks and energy deposits the r-z plane. The *bottom left* plot shows similar information but in the r-ϕ plane, a view looking down the beamline. Finally, the *bottom right* plot is a broader 3D view also looking down the beamline where muon hits are visible.

The following figures show two di-electron events from data with $p_T(\gamma) > 20$ GeV and $\not{E}_T > 25$ GeV, looser cuts than in the analysis. They also show two of the three di-muon events from data with $p_T(\gamma) > 30$ GeV and $\not{E}_T > 40$ GeV. A summary is given in Table 7.1

Figure 7.1: Event 27215903 from run 240307 selected from data as $ee\gamma$. The reconstructed momenta are $p_T(e_1) = 44.1$, $p_T(e_2) = 40.5$, and $p_T(\gamma) = 21.3$ GeV. Also, $\not\!\!E_T = 25.1$, $M(e^+e^-) = 89.7$, and $M(e^+e^-\gamma) = 158.1$ GeV.

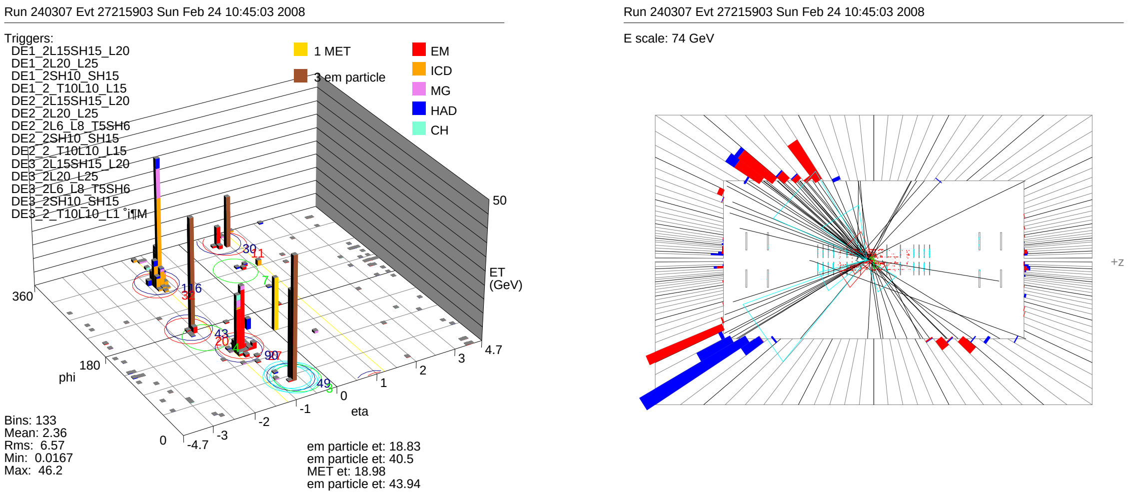

η-ϕ LEGO plot

r-z tracks and calorimeter

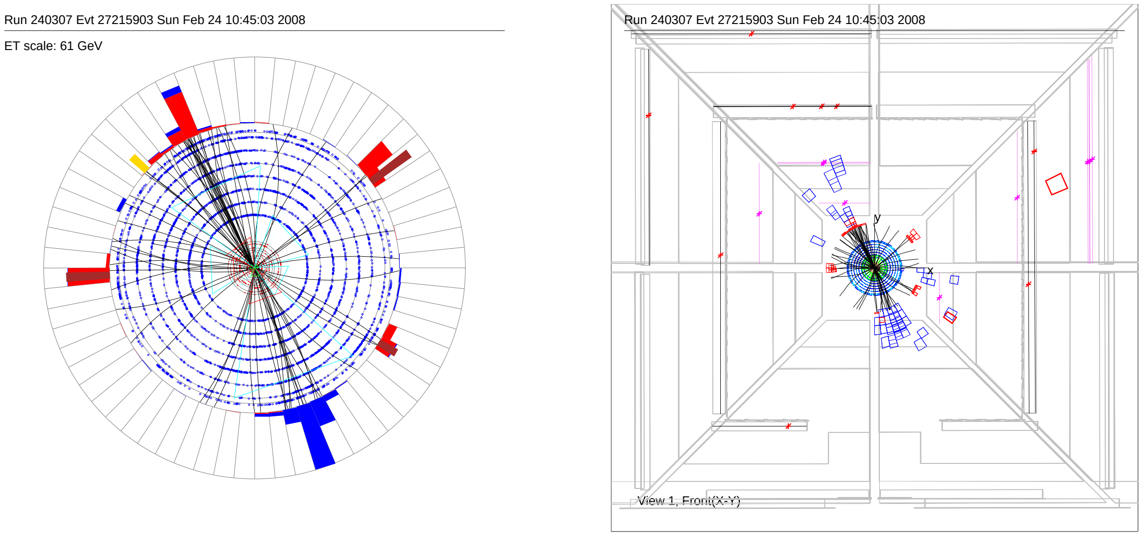

r-ϕ tracks and calorimeter

3D view down z showing muon system

Figure 7.2: Event 29464575 from run 258334 selected from data as $ee\gamma$. The reconstructed momenta are $p_T(e_1) = 120.0$, $p_T(e_2) = 34.5$, and $p_T(\gamma) = 132.7$ GeV. Also, $\not\!\!E_T = 25.8$, $M(e^+e^-) = 99.2$, and $M(e^+e^-\gamma) = 317.3$ GeV.

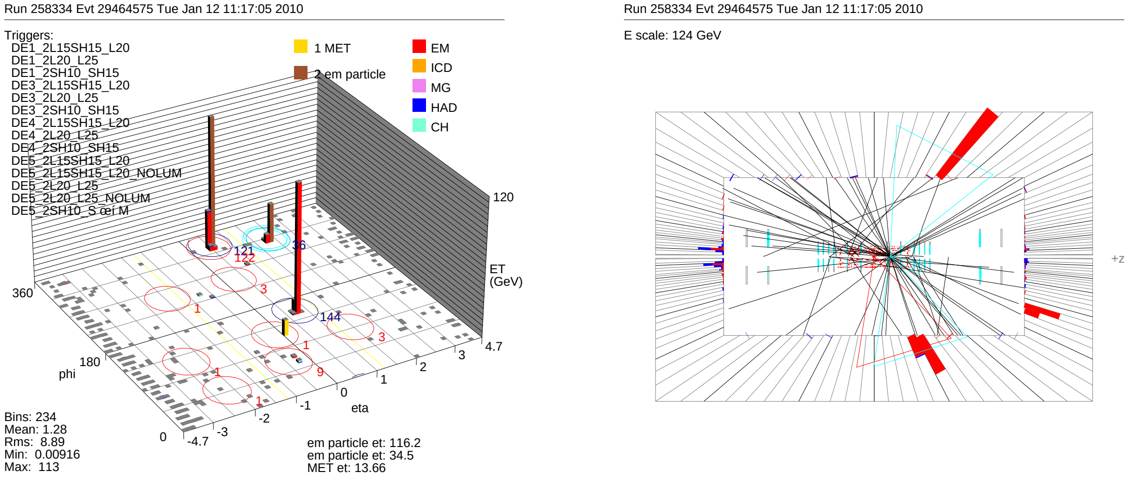

η-ϕ LEGO plot

r-z tracks and calorimeter

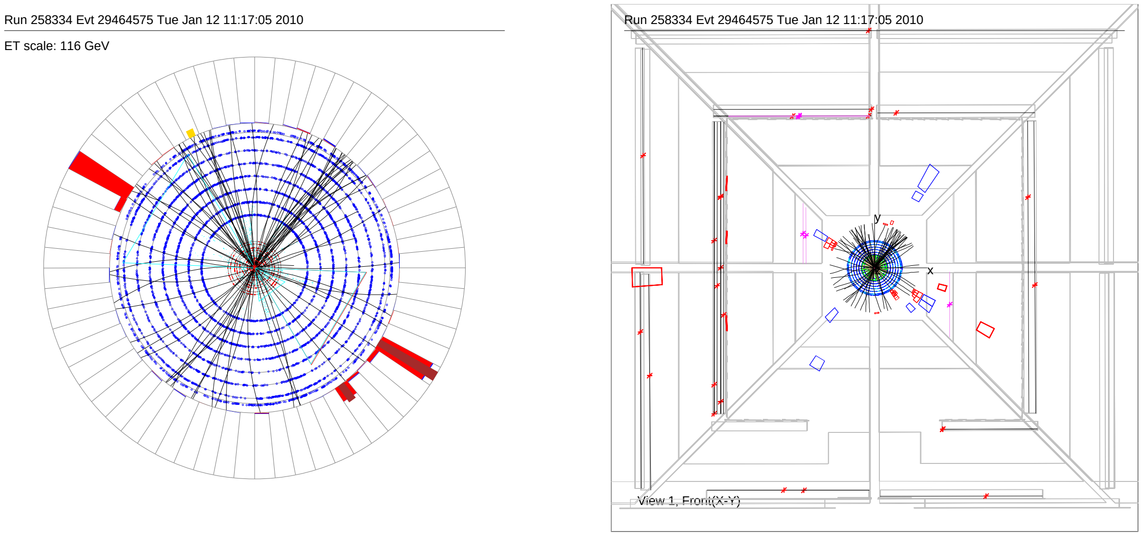

r-ϕ tracks and calorimeter

3D view down z showing muon system

Figure 7.3: Event 12548212 from run 229274 selected from data as $\mu\mu\gamma$. The reconstructed momenta are $p_T(\mu_1) = 136.1$, $p_T(\mu_2) = 17.9$, and $p_T(\gamma) = 73.0$ GeV. Also, $\not\!\!E_T = 60.1$, $M(\mu^+\mu^-) = 108.4$, and $M(\mu^+\mu^-\gamma) = 250.2$ GeV.

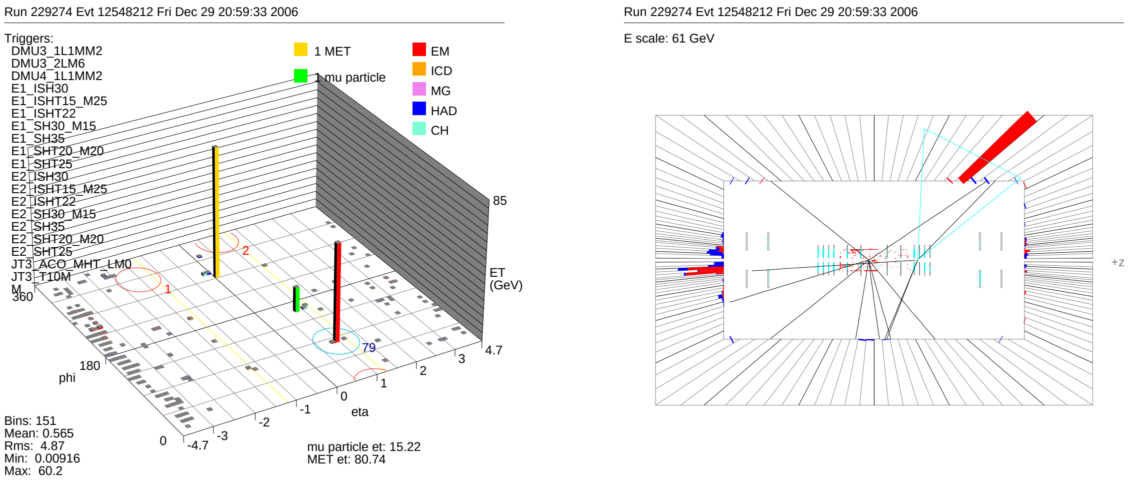

η-ϕ LEGO plot

r-z tracks and calorimeter

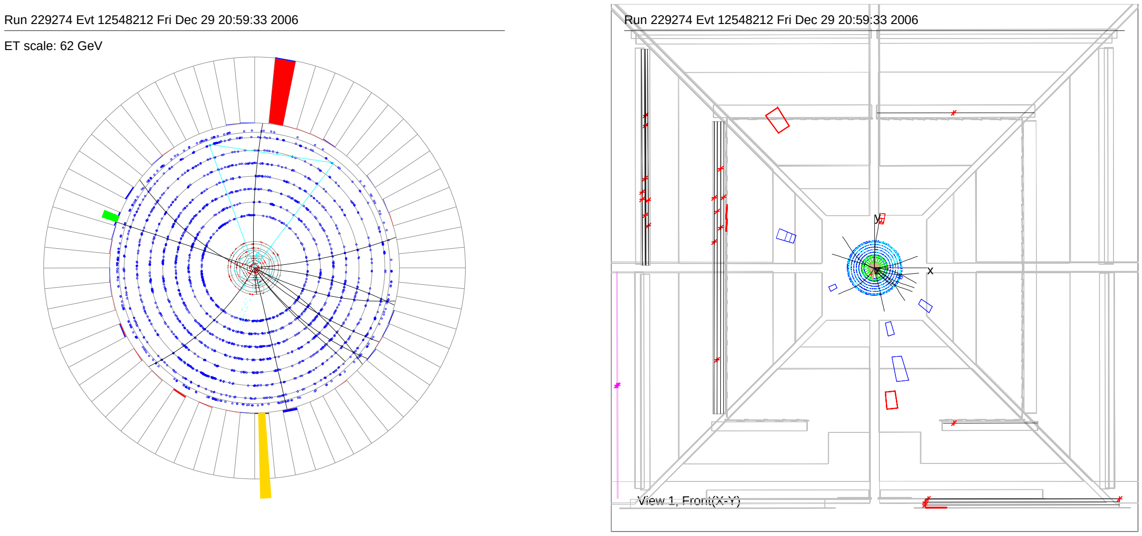

r-ϕ tracks and calorimeter

3D view down z showing muon system

Figure 7.4: Event 12959364 from run 243771 selected from data as $\mu\mu\gamma$. The reconstructed momenta are $p_T(\mu_1) = 137.6$, $p_T(\mu_2) = 27.9$, and $p_T(\gamma) = 81.7$ GeV. Also, $\not{E}_T = 68.3$, $M(\mu^+\mu^-) = 109.0$, and $M(\mu^+\mu^-\gamma) = 249.2$ GeV.

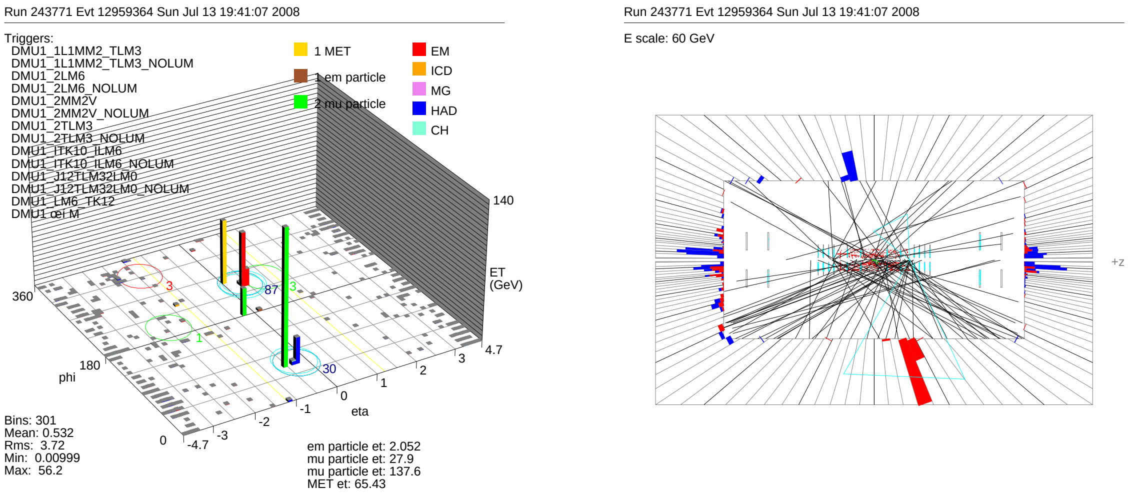

η-ϕ LEGO plot

r-z tracks and calorimeter

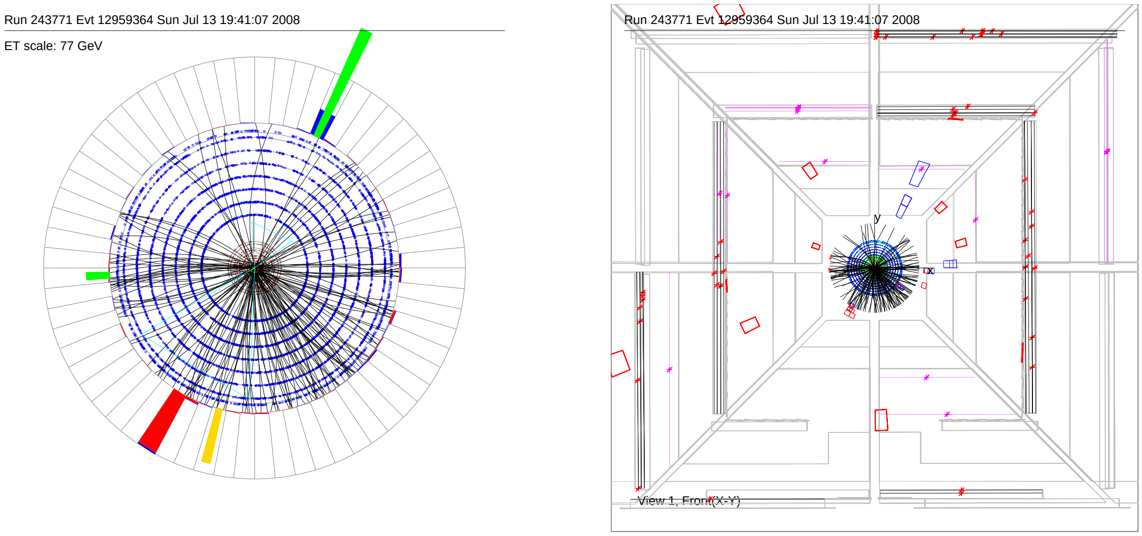

r-ϕ tracks and calorimeter

3D view down z showing muon system

Table 7.1: Summary of events displayed in this Appendix.

	Run	Event	$M(ee)$	$M(ee\gamma)$	$p_T(\gamma)$	$\not{E}_T$	$p_T(e_1)$	$p_T(e_2)$
Figure 7.1	240307	27215903	89.7	158.1	21.3	25.1	44.1	40.4
Figure 7.2	258334	29464575	99.2	317.3	132.7	25.8	120.0	34.5

	Run	Event	$M(\mu\mu)$	$M(\mu\mu\gamma)$	$p_T(\gamma)$	$\not{E}_T$	$p_T(\mu_1)$	$p_T(\mu_2)$
Figure 7.3	229274	12548212	108.4	250.2	73.0	60.1	136.1	17.8
Figure 7.4	243771	12959364	108.9	249.2	81.7	68.3	137.6	27.9

BIBLIOGRAPHY

[1] Fermilab. “Tevatron Luminosity”. http://www.fnal.gov/pub/now/tevlum.html, 2010.

[2] K. Nakamura and P. D. Group. “Review of Particle Physics”. *Journal of Physics G: Nuclear and Particle Physics*, 37(7A):075021, 2010.

[3] A. Pich. “The Standard Model of Electroweak Interactions”. *0705.4264*, May 2007.

[4] V. Buescher, et al. “Combination of CDF and D0 Limits on a Gauge Mediated SUSY Model Using Diphoton and Missing Transverse Energy Channel”. *hep-ex/0504004*, Apr. 2005.

[5] T. C. Collaboration, T. D. Collaboration, T. T. N. Physics, and H. W. Group. “Combined CDF and D0 Upper Limits on Standard Model Higgs-Boson Production with up to 6.7 fb-1 of Data”. *1007.4587*, July 2010.

[6] M. E. Peskin and D. V. Schroeder. *Introduction to Quantum Field Theory.* Addison-Wesley Pub. Co., Reading, Mass., 1995.

[7] H. Georgi, H. R. Quinn, and S. Weinberg. “Hierarchy of Interactions in Unified Gauge Theories”. *Physical Review Letters*, 33(7):451, 1974.

[8] P. G. Mercadante. “Search for supersymmetry at the LHC”. *Brazilian Journal of Physics*, 34(4a):1424–1433, Dec. 2004.

[9] S. P. Martin. “A Supersymmetry Primer”. *hep-ph/9709356*, Sept. 1997.

[10] J. L. Feng, J. Grivaz, and J. Nachtman. “Searches for supersymmetry at high-energy colliders”. *Reviews of Modern Physics*, 82(1):699, Mar. 2010. arXiv:0903.0046v2.

[11] V. M. Abazov, et al. (D0 Collaboration). “Search for Long-Lived Charged Massive Particles with the D0 Detector”. *Physical Review Letters*, 102(16):161802, Apr. 2009.

[12] H. Baer, P. G. Mercadante, X. Tata, and Y. Wang. “Reach of the CERN Large Hadron Collider for gauge-mediated supersymmetry breaking models”. *Physical Review D*, 62(9):095007, Oct. 2000.

[13] N. Panakashvili. "GMSB Parameters (higgsino-like neutralino)", Feb. 2010.

[14] T. Aaltonen, et al. (CDF Collaboration). "Search for Supersymmetry in $p\bar{p}$ Collisions at $\sqrt{s} = 1.96$ TeV Using the Trilepton Signature for Chargino-Neutralino Production". *Physical Review Letters*, 101(25):251801, Dec. 2008. arXiv:0808.2446v3.

[15] V. Abazov, et al. "Search for associated production of charginos and neutralinos in the trilepton final state using 2.3 fb-1 of data". *Physics Letters B*, 680(1):34–43, Sept. 2009. arXiv:0901.0646v1.

[16] B. Mukhopadhyaya and S. Mukhopadhyay. "Same-sign trileptons and four leptons as signatures of new physics at the Large Hadron Collider". *Physical Review D*, 82(3):031501, 2010. arXiv:1005.3051v2.

[17] V. Abazov, et al. "Search for supersymmetry in di-photon final states at". *Physics Letters B*, 659(5):856–863, Feb. 2008.

[18] V. M. Abazov, et al. (D0 Collaboration). "Search for Diphoton Events with Large Missing Transverse Energy in $6.3 fb^{-1}$ of $p\bar{p}$ Collisions at $\sqrt{s} = 1.96$ TeV". *Physical Review Letters*, 105(22):221802, Nov. 2010.

[19] P. C. Bhat and W. J. Spalding. "Fermilab Collider Run II: Accelerator Status and Upgrades". *AIP Conference Proceedings*, 753(1):30–41, Mar. 2005. arXiv:hep-ex/0410046v1.

[20] L. U. Group. "Tevatron Run II Handbook", 1998.

[21] V. Shiltsev. "Status of the tevatron collider run II and novel technologies for luminosity upgrades". In *Proceedings of the 2004 European Particle Accelerator Conference*, volume 1, page 239, Lucern, Switzerland, 2004.

[22] Fermilab. "Operations Rookie Books". http://www-bdnew.fnal.gov/operations/rookie_books/rbooks.html, 2010.

[23] fredatvisualmedia. "Lithium Lens Focusing", Mar. 2008 [Video file]. Video posted to `http://www.youtube.com/watch?v=Y8nWPtWy7U4`

[24] V. Abazov, et al. "The upgraded D0 detector". *Nuclear Instruments and Methods in Physics Research Section A: Accelerators, Spectrometers, Detectors and Associated Equipment*, 565(2):463–537, Sept. 2006.

[25] S. Desai. "Making Tracks at D0", May 2010.

[26] R. Angstadt, et al. "The Layer 0 Inner Silicon Detector of the D0 Experiment". *0911.2522*, Nov. 2009.

[27] S. Abachi, et al. "The D0 detector". *Nuclear Instruments and Methods in Physics Research Section A: Accelerators, Spectrometers, Detectors and Associated Equipment*, 338(2-3):185–253, Jan. 1994.

[28] J. Stark. “Counting Calories at D0”, June 2010.

[29] B. S. Acharya, et al. “Scintillation counters for the D0 muon upgrade”. *Nuclear Instruments and Methods in Physics Research Section A: Accelerators, Spectrometers, Detectors and Associated Equipment*, 401(1):45–62, Dec. 1997.

[30] A. Khanov. “HTF: histogramming method for finding tracks. The algorithm description.”. Internal note 3778, D0, Sept. 2000.

[31] A. Khanov. “HTF”, Dec. 2005.

[32] H. Greenlee. “The D0 Kalman Track Fit”. Internal Note 4303, D0, Dec. 2003.

[33] G. Borissov. “Technical details of AA tracking”, Dec. 2005.

[34] P. Calfayan, et al. “Muon Identification Certification for p17 data”. Internal note 5157, D0, June 2006.

[35] O. Brandt, et al. “Muon identification certification for the summer 2009 extended dataset (Run II-1 and -2)”. Internal Note 6025, D0, Mar. 2010.

[36] M. Cooke, et al. “Muon Momentum Oversmearing Update for p20 Data”. Internal Note 6031, D0, Feb. 2010.

[37] S. Trincaz-Duvoid and P. Verdier. “Missing ET Reconstruction in p17”. Internal note 4474, D0, June 2004.

[38] S. Calvet, P. Verdier, and E. Kajfasz. “Towards MissingET Certification and Unclustered Energy Studies”. Internal note 4927, D0, Sept. 2005.

[39] A. Duperrin. “Missing ET Significance Algorithm with p13 Run II data Application to e + multijets events”. Internal note 4261, D0, Sept. 2003.

[40] A. Schwartzman. “Missing Et Significance Algorithm in RunII data”. Internal note 4254, D0, Sept. 2003.

[41] V. M. Abazov, et al. (D0 Collaboration). “Measurement of the $p\bar{p} \to W\gamma + X$ cross section at sqrt[s]=1.96 TeV and WW gamma anomalous coupling limits”. *Physical Review D*, 71(9):091108, May 2005.

[42] V. Abazov, et al. “$Z\gamma$ production and limits on anomalous $ZZ\gamma$ and $Z\gamma\gamma$ couplings in $p\bar{p}$ collisions at $\sqrt{s} = 1.96$ TeV”. *Physics Letters B*, 653(5-6):378–386, Sept. 2007.

[43] A. Jonckheere and N. Khalatyan. “DZero Data Quality Coordination”. http://www-d0.fnal.gov/computing/data_quality/d0_private/forusers.html, 2010.

[44] H. Baer, F. Paige, S. Protopopescu, and X. Tata. “ISAJET”.

[45] H. Baer, F. E. Paige, S. D. Protopescu, and X. Tata. “ISAJET 7.69: A Monte Carlo Event Generator for pp, $\bar{p}p$, and $e^{=}e^{-}$ Reactions”. *hep-ph/0312045*, Dec. 2003.

[46] P. Skands. “SUSY Les Houches Accord”. http://home.fnal.gov/ skands/slha/, 2010.

[47] T. Sjstrand, S. P. Martin, and P. Skands. “PYTHIA 6.4 physics and manual”. *Journal of High Energy Physics*, 2006(05):026, May 2006. arXiv:hep-ph/0603175v2.

[48] M. L. Mangano, F. Piccinini, A. D. Polosa, M. Moretti, and R. Pittau. “ALPGEN, a generator for hard multiparton processes in hadronic collisions”. *Journal of High Energy Physics*, 2003(07):001–001, 2003.

[49] M. Shamim and T. Bolton. “Generator level reweighting of Z boson pT”. Internal note 5565, D0, Jan. 2008.

[50] X. Bu, G. Chen, and M. Takahashi. “Electron preselection efficiency study for Run II data”. Internal note 6006, D0, Nov. 2009.

[51] X. Bu, T. Head, K. Petridis, M. Takahashi, and Y. Xie. “Electron identification for summer 2010”. Internal note 6116, D0, Sept. 2010.

[52] D. Bandurin, et al. “Photon Identification for Run II data”. Internal Note 6004, D0, Oct. 2009.

[53] E. Barberis, et al. “The Matrix Method and its Error Calculation”. Internal note 4564, D0, Aug. 2004.

[54] U. Heintz. “Matrix Method Uncertainties”. Internal note 5534, D0, Nov. 2007.

[55] D. Bandurin and M. Takahashi. “Electron charge misidentification for p17 and p20 data and Monte Carlo”. Internal note 5927, D0, May 2009.

[56] T. Andeen, et al. “The D0 experiment’s integrated luminosity for Tevatron Run IIa”. Technical Report FERMILAB-TM-2365, Fermilab, Apr. 2007.

[57] S. Moch and P. Uwer. “Theoretical status and prospects for top-quark pair production at hadron colliders”. *Physical Review D*, 78(3):034003, 2008.

[58] J. M. Campbell and R. K. Ellis. “Update on vector boson pair production at hadron colliders”. *Physical Review D*, 60(11):113006, Nov. 1999.

[59] B. P. Roe, et al. “Boosted decision trees as an alternative to artificial neural networks for particle identification”. *Nuclear Instruments and Methods in Physics Research Section A: Accelerators, Spectrometers, Detectors and Associated Equipment*, 543(2-3):577–584, May 2005.

[60] H. Yang, B. P. Roe, and J. Zhu. "Studies of boosted decision trees for MiniBooNE particle identification". *Nuclear Instruments and Methods in Physics Research Section A: Accelerators, Spectrometers, Detectors and Associated Equipment*, 555(1-2):370–385, Dec. 2005.

[61] H. Yang, B. P. Roe, and J. Zhu. "Studies of stability and robustness for artificial neural networks and boosted decision trees". *Nuclear Instruments and Methods in Physics Research Section A: Accelerators, Spectrometers, Detectors and Associated Equipment*, 574(2):342–349, May 2007.